University of Padova

Faculty of Engineering

Department of Information Engineering

Tesi di Laurea Magistrale in Ingegneria Dell'Automazione

Battery Management System for Li-ion Batteries in Hybrid Electric Vehicles

Graduate candidate: Giacomo Marangoni

Thesis Advisor: Ch.mo Prof. Alessandro Beghi

Padova, December 7th, 2010

"No problem can be solved
from the same level of consciousness
that created it."

Albert Einstein

Acknowledgments

Grazie al professor Beghi,
per la sua preziosa disponibilità,
fiducia nei miei confronti
e tolleranza ai miei ritardi.

Grazie ai miei genitori e alla mia famiglia,
fonte di affetto e supporto indispensabili
per il raggiungimento di questo traguardo.

Grazie a Luisa e a tutti i miei amici,
che più o meno consapevolmente
mi hanno continuamente ispirato
a dare il meglio di me.

Abstract

One of the most attractive technologies for improving fuel economy in a vehicle is the use of hybrid powertrain technology. This has led to the development of charge-sustaining hybrid electric vehicles (HEVs), which currently combine an internal combustion engine (ICE) and an electrical motor (EM).

Central to the hybrid concept implementation is the performance of the energy storage device feeding the electrical motor. Due to cost, weight and packaging constraints, current production mostly uses rechargeable batteries with nickel-metal hydride (NiMH) cells. However, the automotive industry is fast evolving to lithium ion or lithium ion polymer chemistries, which have more favorable power, energy density, efficiency and environmental impact. In this context, the so-called dual-intercalation Li-ion battery is the most practical, reliable and popular choice among present lithium-based batteries. It uses a lithiated carbon intercalation material for the negative electrode, a lithiated transition metal intercalation oxide for the positive electrode and a liquid organic solution or a solid polymer for the electrolyte. Compared to the first lithium metal batteries, the intercalation structure has proved to significantly enhance reversibility and safety, at the cost of sacrificing energy density.

Although the diffusion of these lithium-ion batteries (LIBs) is already widespread in the portable electronics field, energy and power requirements for vehicle propulsion are much more rigorous, and operating these batteries safely, efficiently and reliably, as it is strictly required in the automotive field, is a challenging task.

The HEV component responsible for the efficient and safe usage of the vehicle battery pack is referred to as the battery management system (BMS). Its main activity is to track the state of charge (SoC) and state of health (SoH) of the battery pack, as well as perform maintenance actions such as cell balancing and cooling to provide maximum lifetime for the pack.

Unfortunately, SOC and SOH are not directly measurable quantities, and an estimation process is required. The most accurate estimates are obtained by matching the available measurements with an electrochemical model of the LIB under monitoring, exploiting stochastic methods like Kalman filtering.

This work reviews the development of a rigorous electrochemical model for a LIB, and explores one of the most recent techniques proposed by the literature that enables an accurate SOC estimation by means of an Unscented Kalman Filter. The theoretical framework is accompanied by simulations supporting the validity of the chosen approach.

Keywords: Battery Management System, Lithium-ion Battery Modeling, Automotive Battery Technology, SOC estimation, Unscented Kalman Filter

---

Contents

Chapter 1

Introduction

Contents

1.1 Hybrid Electric Vehicles (HEVs)

Modern transportation strategies are experiencing a slow but necessary revolution. The awareness of the need for this change has been mainly arisen by two critical problems of internal combustion engine (ICE) vehicles: air pollution of gas emissions and oncoming petroleum shortage. This technology, in spite of its current popularity, is not a viable option for the future, and sustainable alternatives have been and must be considered. For the near future, hybrid electric vehicles are a concrete answer to the aforementioned problems, among with electric vehicles and fuel cell vehicles.

The idea behind hybrid vehicles consists of combining two or more different power sources, which complement each other in such a way that consumptions and gas emissions are reduced. Several architectures have been designed for implementing this idea in HEVs [11]. The only common feature is the presence of two kinds of energy flow in the drive train: one is mechanical and and the other is electrical.

Up to date, the primary power source has been still considered to be an ICE. In future scenarios the ICE will be very likely replaced by more environmentally friendly systems like fuel cells converters. A second power source is provided to the vehicle by an energy storage device, like a rechargeable battery. The energy unit feeds an electric motor, which assists or replace the ICE in powering the vehicle. This configuration leads to three main benefits:

- the possibility to use smaller and more economical ICEs, because of the presence of an auxiliary power source;

- the possibility to avoid using the ICE when it is more inefficient (at low powers, or when the vehicle is stationary or braking);
- the ability to recover part of the braking energy, accumulating it in the energy storage device (regenerative braking).

The usual approach with regards to energy storage management is defined as *charge sustaining*: the energy unit is maintained in a specified range of *State-Of-Charge* (SOC) through the power provided by the heat engine and the regenerative braking system [5]. This is very different from EV designs, where the energy unit is meant to be deeply discharged, and then recharged only through the electric grid.

Most of charge sustaining HEVs are referred to as full HEVs (FHEVs), meaning that they can store enough energy to run, even if for limited distances, exclusively on the electric motor. So called *mild hybrid electric vehicles* (MHEVs) are very similar to FHEVs, but they are not capable of an exclusive electric-only mode of propulsion, as they have smaller electric motors and smaller batteries. The resulting fuel efficiency improvement is not as significant as the one of full HEVs: according to the benchmarks of Manzie [17], fuel savings in MHEVs are of the order of 10 % to 15 % with respect to a non-hybrid vehicle, while in full-hybrid vehicles they belong to a practical range of 15 % to 25 %, with a theoretical relative improvement of the 30 % to 40 %. Nonetheless, the costs for mild-hybrids are lower, thus providing an interesting cost-attractive alternative.

A different strategy is implemented in *plug-in hybrid electric vehicles* (PHEVs), having larger batteries than those used in FHEVs, which allow for longer driving ranges in all-electric mode (e.g. 30-100 km). These vehicles are more similar to EVs rather than charge sustaining HEVs, since their energy storage devices are meant to be recharged through the electrical grid. This approach has the advantage of using energy generated with higher efficiency than the energy produced by an ICE. In this way, the fuel consumption, as well as the dependency on petroleum, can be considerably reduced, and the operating costs are potentially lower than the other hybrid alternatives. However, demanding requirements on PHEVs batteries pose non-trivial technologic and economic problems.

1.2 Energy storage devices

A fundamental component for any hybrid electric or pure electric vehicle is a portable device which is capable of storing electrical energy. In a charge sustaining HEV, this energy device is almost permanently either on discharge or charge, and must be capable of delivering peak power to the drivetrain during discharge, and of accepting power from the engine or from regenerative braking during charge. Thus, the main requirement of the energy unit is its ability to sustain a very large number of high drain and shallow cycles, and store this energy efficiently.

In 2002, a set of quantitative requirements and performance goals for power-assist HEV energy storage devices was issued under the FreedomCAR project, a

Characteristic	Range of values
Pulse discharge power (constant for 10 s)	25 kW to 40 kW
Peak regenerative pulse power (10 s, for specified pulse energy)	20 kW (for 55 W h pulse) to 35 kW (for 7 W h pulse)
Total available energy (over DOD[a] range where power goals are met)	0.3 kW h to 0.5 kW h (at C1/1 rate[b])
Minimum round-trip energy efficiency	90 % (25 W h cycle) to 90 % (50 W h cycle)
Cold cranking power at −30 °C (three 2 s pulses, 10 s rest between)	5 kW to 7 kW
Cycle life (for specified SOC increments)	300×10^3 25 W h cycles (=7.5 MW h) to 300×10^3 50 W h cycles (=15 MW h)
Calendar life	15 years
Maximum weight	40 kg to 60 kg
Maximum volume	32 dm^3 to 45 dm^3
Operating voltage limits	$V_{max} < 400$ V, $V_{min} > 0.55 V_{max}$
Maximum allowable self-discharge rate	50 W h per day
Temperature range: equipment operation	−30 °C to 52 °C
Temperature range: equipment survival	−46 °C to 66 °C
Production cost, at 100,000 units per year	500 $ to 800 $

[a] DOD stands for Depth of Discharge.
[b] The C rate of a current (charging or discharging) is defined as the ratio of the current in amperes to the nominal capacity of the energy unit in ampere-hours.

Table 1.1: FreedomCAR energy storage performance goals for power assist HEV (November 2002)

U.S. national program for developing more energy efficient and environmentally friendly transportation technologies. As an indication, these quantities are reported in Table 1.1, whose entries are thoroughly explained in Broussely [4]. In general, the following features are desirable: high specific power (i.e. power per unit of mass), high specific energy (i.e. energy per unit of mass), high charge acceptance rate for recharging and regenerative braking, long calendar and cycle life, high efficiency, and a reasonable cost [15]. This list, to be complete, should contain many other characteristics, like maintenance requirement, management, environmental friendliness, and safety.

So far, energy storages that can fully or partially meet the required specifications mainly include rechargeable electrochemical batteries, ultracapacitors or supercapacitors, and ultra-high-speed flywheels [11]. Fuel cells are not mentioned in this context, since, strictly speaking, they are particular types of energy converters and not storage devices.

1.2.1 Rechargeable batteries

The most common devices for storing energy in HEVs are rechargeable batteries. A battery used for high-power applications like HEVs is a collection of several modules, each of which consists of one or more interconnected electrochemical cells. These elemental units are capable of converting electrical energy, coming from the outside, into potential chemical energy during charging, and viceversa during discharging.

Every electrochemical cell can be thought as a sandwich of different materials, with two electronic conductors at the sides, called *electrodes*, an electronic insulator between the two electrodes, called *separator*, and an ionic conductor in which all the cell is immersed, called *electrolyte*. One electrode is denoted as positive, and the other as negative. During operation both are connected to an external circuit through terminals of appropriate conductive materials. The electrochemically active ingredient of the positive or negative electrode is called the *active material*. Thanks to the chemical oxidation and reduction processes in which active materials are involved, electrons are transported from one electrode to another providing usable electric current when discharging, or storing energy during charging. Because of the presence of undesired side reactions, a small current flows also when the external circuit is not completed, a phenomenon called self-discharge.

A rich variety of chemistries combinations can be successfully used in battery manufacture, and each resulting battery system can be more or less advantageous depending on the application. A brief presentation of the current main viable options for the hybrid electric automotive field, with corresponding advantages and disadvantages, is reported below [16, 15, 11]. Table 1.2 summarizes some important figures for the mentioned battery systems, as printed in Husain [15], while Figure 1.1 illustrates a similar comparison reported by Debert et al. [7], establishing approximately the same performance figures.

Lead-acid Lead-acid batteries have a very long existence: the first models to be produced are dated as early as in 1859. This is due to the relatively low cost and easy availability of raw materials (lead, lead oxide, and sulfuric acid), the ease of manufacture and the favorable electromechanical properties. Since the middle of the 19th century, these batteries have continued to be developed, and nowadays they represent the most widespread and mature technology among commercialized battery systems. Low cost, reliability and relatively high-power capability are the main advantages of this technology. However, low specific energy, poor cold temperature performance, and short calendar and cycle life are among the obstacles to their use in EVs and HEVs.

Nickel/Cadmium Nickel/cadmium technology has brought an enormous technical improvement because of the advantages of high specific power (over 220 W/kg), long cycle life (up to 2000 cycles), high tolerance to electric and mechanical abuse, a small voltage drop over a wide range of discharge currents, rapid charge capability (about 40 % to 80 % in 18 min), wide operating temperature range (−50 °C to 60 °C), low self-discharge rate (< 0.5 % per

day), excellent long-term storage due to negligible corrosion, and availability in a variety of sizes. However, the nickel/cadmium battery has also some disadvantages, including high initial cost, relatively low cell voltage, and the carcinogenicity and environmental hazard of cadmium.

Ni-MH The Ni-MH battery has been on the market since 1992. Its characteristics are similar to those of the nickel/cadmium battery. The principal difference between them is the use of hydrogen, absorbed in a metal hydride, for the active negative electrode material in place of cadmium. Its advantages are summarized as follows: it has the highest specific energy (70 Wh/kg to 95 Wh/kg) and highest specific power (200 W/kg to 300 W/kg) of nickel-based batteries; environmental friendliness (cadmium free); a flat discharge profile (smaller voltage drop); and rapid recharge capability. However, this battery still suffers from its high initial cost. It may also exhibit memory effects and produce exothermic reactions during charging. Toyota and Honda have used Ni-MH batteries in their HEVs (Prius and Insight, respectively).

Li-Polymer Li-Polymer batteries use lithium metal and a transition metal intercalation oxide (M_yO_z) for the negative and positive electrodes, respectively. A thin solid polymer electrolyte (SPE) is used, which offers the merits of improved safety and flexibility in design. It operates at a nominal voltage of 3 V and has a specific energy of 155 Wh/kg and a specific power of 315 W/kg. The corresponding advantages are a very low self-discharge rate (about 0.5 % per month), capability of fabrication in a variety of shapes and sizes, and relatively safe design (because of the reduced activity of lithium with solid electrolyte). However, it has the drawback of relatively weak low-temperature performance due to the temperature dependence of the electrolyte ionic conductivity, which dictates an ideal operating temperature range of 80 °C to 120 °C.

Li-Ion Since the first announcement of the Li-Ion battery in 1991, this battery technology has experienced an enormous growth, conquering almost all the field of portable electronic appliances and becoming very promising for high power applications. The Li-Ion battery uses a lithiated carbon intercalation material (Li_xC) for the negative electrode instead of metallic lithium, a lithiated transition metal intercalation oxide ($Li_{1-x}M_yO_z$) for the positive electrode, and a liquid organic solution or a solid polymer for the electrolyte. The materials used for the positive electrode are mainly nickel, cobalt and manganese. Nickel-based Li-Ion batteries have a nominal voltage of 4 V, a specific energy of 120 Wh/kg, an energy density of 200 Wh/L, and a specific power of 260 W/kg. The Cobalt-based type has higher specific energy and energy density, but with a higher cost and significant increase of the self-discharge rate. Manganese-based solutions have the lowest cost and their specific energy and energy density lie between those of the cobalt-based and nickel-based chemistries. In general, lithium-ion batteries have high specific energy, high specific power, high energy efficiency, good high-temperature performance,

low self-discharge, and mostly recyclable components. These characteristics make Li-Ion batteries highly suitable for applications like EV and HEV. Recently, the battery manufacturer SAFT reported the development of Li-Ion high-power batteries for HEV applications with a specific energy of 85 Wh/kg and a specific power of 1350 W/kg. SAFT also announced high-energy batteries for EV applications with about 150 Wh/kg and 420 W/kg.

Battery type	**Specific energy** Wh/kg	**Specific power** W/kg	**Energy efficiency** %	**Cycle life**	**Estimated cost** US$/KWh
Lead-acid	35 – 50	150 – 400	80	500 – 1000	100 – 150
Ni-Cd	30 – 50	100 – 150	75	1000 – 2000	250 – 350
Ni-MH	60 – 80	200 – 300	70	1000 – 2000	200 – 350
Li-Poly	150 – 200	350	n.a.	1000	150
Li-Ion	80 – 130	200 – 300	> 95	1000	200

Table 1.2: Review of battery chemistries for automotive applications [15].

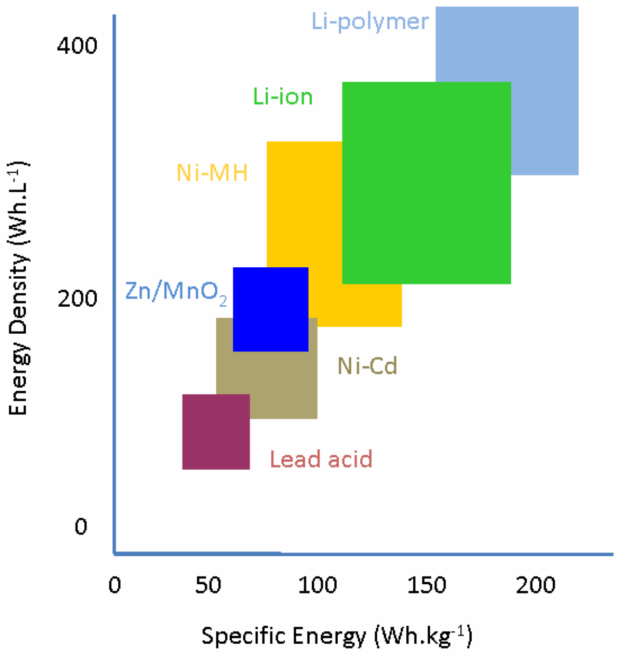

Figure 1.1: Energy and power capabilities comparison between different battery technologies suitable for HEVs [7].

Although still in the stage of development, the Li-Ion battery has already gained acceptance for EV and HEV applications. The "Mercedes S400 Class Hybrid" and "BMW 7 Series ActiveHybrid" are two commercially available mild-hybrid cars that already employ this battery technology. Because of their promising features, almost all of the major automakers have been working on prototypes of FHEV and PHEV

that exploit Li-Ion batteries [23], and it is expected to see them on the market pretty soon.

1.2.2 Ultracapacitors

The main technology representing the concept of an ultracapacitor is the double-layer capacitor produced using microporous carbon in both of the electrodes. Compared to batteries, the ultracapacitor is characterized by a much higher specific power (up to 3 kW/kg) but a much lower specific energy (a few watt-hours per kilogram). In order to justify the development of ultracapacitors as a technology separate from high power batteries, ultracapacitors should exhibit significant improvements in power capability and cycle life with respect to batteries.

Due to the low specific energy density and the dependence of terminal voltage on SOC, it is difficult to use ultracapacitors alone as an energy storage for FHEVs or PHEVs. Instead, ultracapacitors are suitable in combination with other energy units, or in mild hybrids with relatively small storage requirements (e.g. 75 Wh to 150 Wh of useable energy). If the energy storage requirement is too large, the weight, volume and cost of the ultracapacitor unit are too high, and batteries become more convenient.

One promising application is the so-called battery and ultracapacitor hybrid energy storage system, which will be briefly described in a later paragraph.

1.2.3 Ultra-high-speed flywheels

Flywheels are rotating devices that store energy in mechanical form. More than 25 years ago, the Oerlikon Engineering Company in Switzerland made the first passenger bus solely powered by a massive flywheel. This flywheel, weighing 1500 kg and operating at 3000 rpm, was recharged by electricity at each bus stop. While the traditional flywheel is a massive steel rotor with hundreds of kilograms that spins on the order of ten hundreds of rpm, the so-called ultra-high-speed flywheel is a lightweight composite rotor with tens of kilograms, rotating on the order of ten thousands of rpm,

Several positive features make the ultra-high-speed flywheel a particularly attractive solution, capable of fulfilling the above-mentioned requirements: high specific energy, high specific power, long cycle life, high energy efficiency, quick recharge, maintenance-free characteristics, cost effectiveness, and environmental friendliness. Nevertheless, its application to EVs and HEVs suffers from two specific problems. First, gyroscopic forces occur whenever a vehicle departs from its straight-line course, such as in turning and in pitching upward or downward from road grades. These forces essentially reduce the maneuverability of the vehicle. Second, if the flywheel is damaged its stored mechanical energy will be released in a very short period of time. The corresponding released power will be very high, which can cause severe damage to the vehicle. Containment in case of failure is presently the most significant obstacle to implementing the ultra-high-speed

flywheel in EVs and HEVs.

Many companies and research agencies (such as Lawrence Livermore National Laboratory (LLNL) in the United States, Ashman Technology, AVCON, Northrop Grumman, Power R&D, Rocketdyne/Rockwell Trinity Flywheel US Flywheel Systems, Power Center at UT Austin, and so on) have engaged in the development of ultra-high-speed flywheels for EVs and HEVs. However, technologies of ultra-high-speed fly- wheels are still in their infancy. Typically, the whole ultra-high-speed flywheel system can achieve a specific energy of 10 Wh/kg to 150 Wh/kg and a specific power of 2 kW/kg to 10 kW/kg.

1.2.4 Energy storage hybridization

A key issue in the present battery design is the trade-off among specific energy, specific power, and cycle life. The difficulty in simultaneously obtaining high values for all of these three characteristics has led to considering a hybridization of the energy storage device as a combination of an energy source and a power source. The energy source, mainly batteries and fuel cells, provides the high specific energy, whereas the power source has high specific power. In this way, specific energy and specific power requirements can be decoupled, thus affording an opportunity to design a battery that is optimized for specific energy and cycle life with little attention being paid to specific power. Ultracapacitors are well suited for the role of auxiliary power sources, which can be recharged from the energy sources during less demanding driving situations or through the regenerative braking. Due to the load leveling effect of the ultracapacitor, high charging/discharging currents from or to the battery can be minimized, so that available energy, endurance, and life of the battery can be significantly increased.

1.3 Battery Management System (BMS)

The power and energy capabilities of a battery pack greatly depend on operating conditions, like charge/discharge current rate, state of charge, load characteristics and temperature. Furthermore, it is important to avoid or contain the circumstances that could damage the battery or arise safety issues for the surrounding environment. Especially for battery chemistries like the lithium-based ones, and especially in a high-power context, events like overcharge, overdischarge and excessive heating can lead to irreversible and possibly destructive processes.

Rechargeable batteries, when used for traction purposes like in HEVs, are generally part of a wider and more complex system, which comprises all the hardware and software needed to proficiently make the most out of them. A crucial role is played by the battery management system, whose main goal is ensuring that the battery is operated within safe limits and achieves optimum performance over its life (and over a wide range of operating and environmental conditions) [12]. Commonly, a BMS does not directly control the electrical usage of the battery, since

a higher controller is responsible for decisions concerning the propulsion of the vehicle. However, it is up to the BMS to provide accurate data on the state of the battery for the hybrid propulsion controller algorithm to run properly, safely and reliably (Figure 1.2). The activity of a BMS can be classified into six functions.

Measuring Particular observable characteristics of the battery cells, pack, or management system are quantified. Typical measured quantities are voltages, temperatures and currents, either at the single cell or at the battery pack level.

Calculating The measurement data is processed to determine additional non-directly measurable useful information. This includes the estimation of quantities like the State-Of-Charge (SOC), the State-Of-Power (SOP) and the State-Of-Health (SOH). The first two denote the remaining energy capacity and the instantaneous power availability, respectively. The SOH quantifies the performance deviation from pristine conditions due to aging.

Monitoring Some of the measured or estimated characteristics are checked against critical thresholds and, in case, warnings are issued.

Communicating The information from monitoring, measuring, and calculating functions are provided to other subsystems or devices in a useful manner.

Control The BMS may have direct control on critical aspects of the battery pack, such as interrupting current during charge or discharge, or altering the thermal management system. This is usually done to achieve redundant protection against possibly abusive situations.

Balancing Cells are usually matched during the manufacturing of a battery pack. Over time, an imbalance in the state of charge may develop between cells and reduce the overall capacity of the pack. This can be due to slight differences in self-discharge, temperature, or many other factors, between cells. Implementing a strategy that equalizes the SOC of the cells allows the pack to operate longer.

1.3.1 SOC estimation

Among these functions, one of the most critical for the purposes of a BMS is estimating the state of charge of the battery cells. According to the charge sustaining HEV principle, batteries are meant to operate in a relatively narrow State-Of-Charge (SOC) range (e.g. 10 % to 30 %), with frequent and shallow charging and discharging cycles around a fixed intermediate SOC level. This approach has two main advantages. First, the battery cycle and calendar life is significantly extended (e.g. 15 years), compared to the life of batteries which are meant to be deeply discharged and recharged (e.g. 10 years). This follows from operating the battery away from

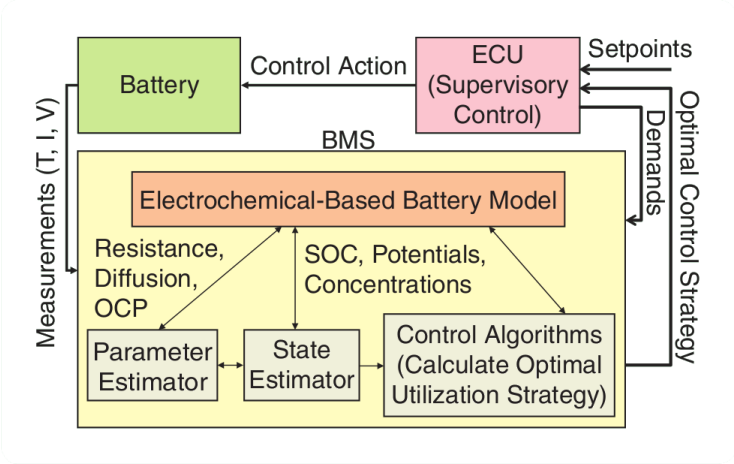

Figure 1.2: Architecture of an advanced BMS, which relies on an electrochemical model to provide accurate battery state tracking [6].

overcharge or overdischarge conditions, where side-reactions that change the internal functional structure of the cells are more likely to occur. Second, the battery is operated in a SOC region where it is capable of sustaining higher incoming or outgoing power rates. This is decisive for meeting the HEV propulsion needs, as well as for taking advantage of the sudden peaks of recharging power coming from regenerative breaking.

The efficiency, safety and reliability of this system considerably depends on the accuracy of the SOC readings. Since the SOC is a non-directly observable quantity, these readings are the result of an estimation process, which can range in complexity from simple voltage-SOC correlation calculations to more complex stochastic filtering techniques. In less stringent applications, like portable electronic devices, where the power involved is smaller and the charging/discharging dynamics are slower and more predictable, the simpler methods can be successfully implemented. Unfortunately, these approaches are not viable in more stringent environments, e.g. when using lithium-ion based batteries in a HEV design. In this case, performance and safety requirements dictates the necessity for more advanced techniques, capable of optimally combining historical and present measurement data with a satisfactory model of the battery, and of adapting the model to the aging of the battery.

Because of the increasing interest in HEV lithium-based batteries, and because of the present-day challenges and the beneficial potentials related to SOC estimation in this field, the work that follows mainly focuses on this topic. State-of-the-art solutions are proposed and tested through simulation. Also other aspects of BMS will be mentioned in the conclusions, so that to gain a general understanding of the most significant issues entailed in designing advanced BMS for HEV batteries.

Chapter 2

Lithium-ion batteries

Contents

2.1 Introduction

Among all battery technologies, the family of lithium-based rechargeable batteries is undoubtedly the one which has been experiencing the steepest rise in interest for almost all battery-powered systems in the last decades. Nowadays, it has become a common power source in mobile electronic devices, and it is foreseen to be widespread in the near future [14]. The attraction for lithium in electrochemical applications is justified by its peculiar properties:

- it is the metal with the most negative *standard electrode potential* [1] , allowing for high cell voltages when matched with a powerful oxidizing agent as the cathode (i.e. positive electrode) active material.
- it is the lightest metal, allowing for high cell specific capacities.

Nonetheless, translating this promising features into an effective reality was not an immediate process, as explained in the next section. It was only in 1991, after decades of research driven by the need for better energy storage devices, that the

[1] In an electrochemical cell, an electric potential is created between two dissimilar metals. The cell potential has a contribution from the anode, which is a measure of its ability to lose electrons (i.e. "oxidation potential"), and from the cathode, which is based on its ability to gain electrons (i.e. "reduction potential"). The oxidation/reduction potential of any electrode chemistry with respect to a standard hydrogen electrode (which is assigned a potential of 0 V), under standard thermodynamic conditions, is called standard electrode potential.

Advantages	Disadvantages
• Rechargeable cell chemistry with the highest energy per unit of weight • No memory effect • Good cycle life • High energy efficiency • Good high-rate capability • Environmentally acceptable	• Relatively expensive (although costs have nearly halved in the last decade, and are expected to lower further with the growth of the production volumes) • Safety concerns posed by overheating, overcharge and overdischarge conditions, and consequent necessity for protection circuitry

Table 2.1: Pros and cons of the Li-ion battery chemistry.

first Lithium-Ion Battery (LIB) came out. Table 2.1 schematically presents the main advantages and disadvantages of this chemistry, as reported in Brodd [3].

2.2 Brief history

The following paragraphs outline the historical development of the Li-ion technology, retracing the information that can be found in Xu [38], Matsuki and Ozawa [18] and Yoshio et al. [40].

The first primary lithium batteries

The first lithium-based primary cells were commercialized in 1970s. Lithium metal was used as the anode, and was combined with nonaqueous electrolytes such as propylene carbonate-lithium perchlorate. With regards to the cathode-active material, the most potential candidate was considered to be MnO_2. Manganese-based lithium batteries started to be developed in 1962, and 10 years later SANYO Inc. made them available to the public. The $LiMnO_2$ battery with a lithium metal anode became the first representative primary lithium battery. After that, many other cathode materials were considered and studied, such as TiSe, NbSe, and MoS_2.

Unfortunately, extending this technology to the field of rechargeable batteries was not straightforward. In fact, it was discovered that part of the lithium reacted with the electrolyte during each recharge, forming crystals that led not only to a loss in energy density, but most of all to serious safety hazards. In the worst case, this phenomenon could cause a short between the electrodes, posing thermal runaway and consequent explosion issues. This was almost inevitable in abuse cases such as short circuit, overheating, and overcharging.

The revolution of intercalation

From the 1970s to the 1980s, different electrolyte chemistries and cathode active materials were explored in order to reduce the problems related to the lithium-metal anode. In the meantime, the concept of "intercalation" (or "insertion")-type electrodes started to gain ground. These electrodes are made of materials with stable crystal lattices, like transition metal oxides or chalacogenides. Their lattice structures provide the pathways for guest ions to diffuse. A battery employing such intercalation cathodes and anodes would only have required the lithium ions to shuttle back and forth between the electrodes, without the presence of lithium metal. The enhanced stability and reversibility of these systems greatly improved safety and cycle life of lithium-based batteries, at the cost of significantly sacrificing energy density.

The research in this field was very active in that period. In the 1970s, Steele considered insertion compounds as battery electrodes of a lithium-ion battery based on a non-aqueous liquid electrolyte, while Whittingham reviewed the properties and preparation of many insertion compounds and discussed the intercalation reaction. In 1980, Goodenough filed his patent on $LiCoO_2$ as an intercalation cathode material. One year later, Ikeda of Sanyo patented the graphite as an intercalation material in an organic solvent. These, and other efforts made in this direction, led to the development of the first workable lithium-graphite anode by the Bell Labs a year later. The discovery of carbonaceous materials as anode intercalation hosts marked a turning-point in lithium batteries evolution. The main advantages of this new active material was the low cost of carbon and the high lithium ion activity in the intercalation compound, thus minimizing the energetic penalty. Also the cathode research experienced a significant development, especially thanks to the work of Goodenough and his team. In 1985, the term "lithium-ion battery" appeared for the first time in a patent filed by Yoshino and his colleagues. These Japanese researchers developed a new cell design using an intercalation carbon anode and a $LiCoO_2$ cathode. Since then, the expression they used started to be established worldwide.

The maturity of this technology was ratified by the commercialization and mass-production of the first Lithium-Ion Battery in 1990 by Sony, which revolutionized consumer electronics. The cells of this battery used coke for the anode, and lithium cobalt oxide ($LiCoO_2$) for the cathode. Soon after, a report on the principle of lithium intercalation chemistry with graphitic anodes and the effect of electrolyte solvent in the process was published.

A market in expansion

After Sony's commercialization, various modifications have been made to develop LIBs with higher energy density, while retaining their good safety characteristics. Exploring new electrode chemistries (like the lithium iron-phosphate cathodes), doping the active materials with elements like aluminium, niobium and zirconium,

and improving the design and manifacturing process led to an increase in performance, durability, and safety attributes, which favoured the diffusion of this technology.

The shapes of cells have been widely expanded from cylindrical to prismatic and laminated, and the applications of cells have also widely expanded, from phones and camcorders to laptop computers, power tools, and light electric vehicles, and it is still expanding to always higher power-demanding applications, like EV and HEV as mentioned in Chapter 1.

Lithium-metal batteries: alternative approaches

Because of the not-negligible safety concerns, research on the lithium-metal electrodes slowed nearly to a halt in the 1990s. The end of general enthusiasm in lithium metal as an anode for rechargeable cells can be dated to 1989. In that year, the Canadian company Moli Energy recalled its rechargeable lithium-metal batteries after one caught fire; the incident led to legal action, and the company declared bankruptcy. Nowadays, this type of batteries are only used for small-capacity coin cells (e.g. for memory backup or road signs). However, the research in lithium-metal electrodes have been recently reconsidered for lithium-polymer batteries, briefly discussed in the Introduction, and for the so-called lithium-air batteries, which are being developed in a handful of labs around the world because of their extreme energy density capabilities, although the safety risks are still an issue.

2.3 Working principle

Typically, a cell of a Li-ion battery can be divided into three main components:

- the negative electrode, connected to the negative current collector (or terminal) of the cell;
- the positive electrode, connected to the positive terminal of the cell;
- the separator, which does not allow electrons to flow between the two electrodes.

All these components are soaked in an electrolyte, mostly a single salt in a homogeneous solvent, the latter being a liquid, a gel or a polymer. Electrodes are good electronic conductors, while electrolytes are good ionic conductors. Other materials, like binders and fillers, are introduced in the cell to improve the conductivity of the electrodes and the stability of the cell chemical structure (Figure 2.1).

Nowadays, the most common type of Li-ion cell is the *dual-intercalation* cell, where both electrodes are made of Li-insertion compounds, i.e. porous materials which can host lithium in their lattice sites. As the cell is connected to a load, chemical reactions inside the cell start the discharge process. The lithium atoms

at the surface of the porous negative-electrode active material undergo an oxidation reaction, setting free positively charged lithium ions and negatively charged electrons. The positive ions dissolve in the electrolyte and flow from the negative-electrode lattice to the positive one. Concurrently, also the electrons flow towards the positive electrode, but not through the same path, because of the insulation of the separator. Instead, they must flow through the external circuit, resulting in an electric current that does useful work. At the positive electrode, a reduction reaction occurs, so that lithium ions in the electrolyte combine with electrons and fill up the sites of the positive-electrode host matrix. This reduction-oxidation (i.e. redox) reaction allows and sustains the flow of both ionic and electronic current. As the current is forced to flow in the opposite direction by the external circuit, the battery undergoes the process of charging, which is exactly the reverse of what has just been described.

The process of moving ions in and out of the electrodes interstitial sites is called intercalation (hence the name dual-intercalation), while the whole process of operation, involving the shuttling of lithium ions back and forth between the two insertion compounds, is often referred to as rocking-chair.

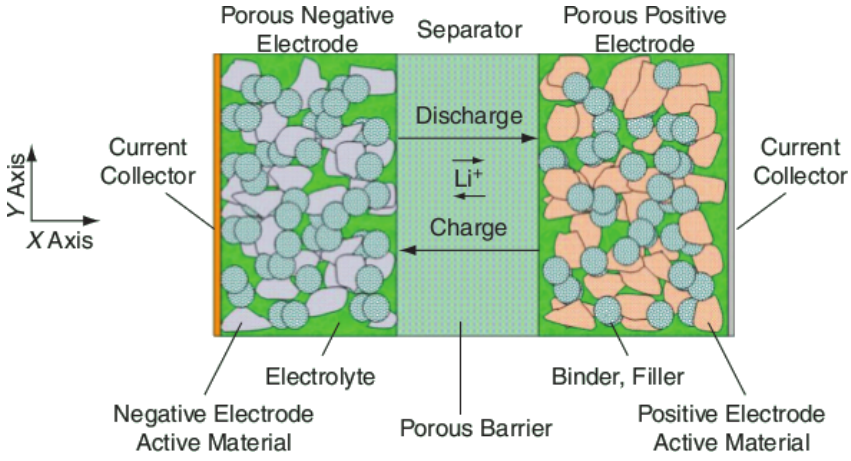

Figure 2.1: Schematic representation of a dual-intercalation Li-ion cell [6].

2.4 One name, different chemistries

Whenever speaking of Li-ion batteries, there are several possible combinations of cathode, anode and electrolyte chemistries which one may be referring to (Figure 2.2).

Table 2.2 highlights some of the characteristics relative to the main intercalation compounds used for cathodes and anodes, according to Yoshio and Noguchi [39].

Among the companies manifacturing Li-ion batteries for HEVs, it does not seem to exist a unique opinion about the best materials to be used, especially for cathodes. For instance, while the French SAFT relies on batteries with a nickel-based

Cathode						
Material	Practical capacity (mAh/g)	Energy density (mAh/cc)	Shape of discharge curve	Safety	Cost	Comment
$LiCoO_2$	160	808	Flat	Fair	High	Small-size
$LiNi_{0.8}Co_{0.2}O_2$	180	873	Sloping	Fair	Fair	Small scale
$LiNi_{0.8}Co_{0.15}Al_{0.05}O_2$	200	960	Sloping	Fair	Fair	Small scale
$LiMn_{0.5}Ni_{0.5}O_2$	160	752	Sloping	Good	Low	
$LiMn_{1/3}Ni_{1/3}Co_{1/3}O_2$	200		Sloping	Good	Low	
$LiMn_2O_4$	110	462	Flat	Good	Low	HEV, EV
$LiAlMnO_4$	100	420	Flat	Good	Low	HEV, EV
$LiFePO_4$	160	592	Flat	Good	Low	Low cond.

Carbon anode		
Material	Practical capacity (mAh/g)	Comment
Spherical graphatized mesocarbon microbeads (MCMB)	$320 - 330$	Easy coating
Graphatized carbon fiber (MCF)	$320 - 330$	Stopped to produce
Pitch base graphite	~ 350	Largest share in the market with electrolyte additives
Carbon-coated natural graphite	$360 \sim 365$	Less decomposition of electrolyte without additives

Alloy anode			
Material	Capacity (mAh/g)	Capacity/volume (mAh/cm^3)	Comment
Li	1840	1920	Safety issues
Sn	990	7230	
Si	4200	9660	
Al	990	2670	
Sb	650	4360	
$SnB_{0.5}Co_{0.5}O_3$	600	2220	High irreversible capacity
$Li_{2.6}Co_{0.4}N$	1200	2640	Unstable in air

Table 2.2: Properties of anode and cathode materials for Li-ion batteries.

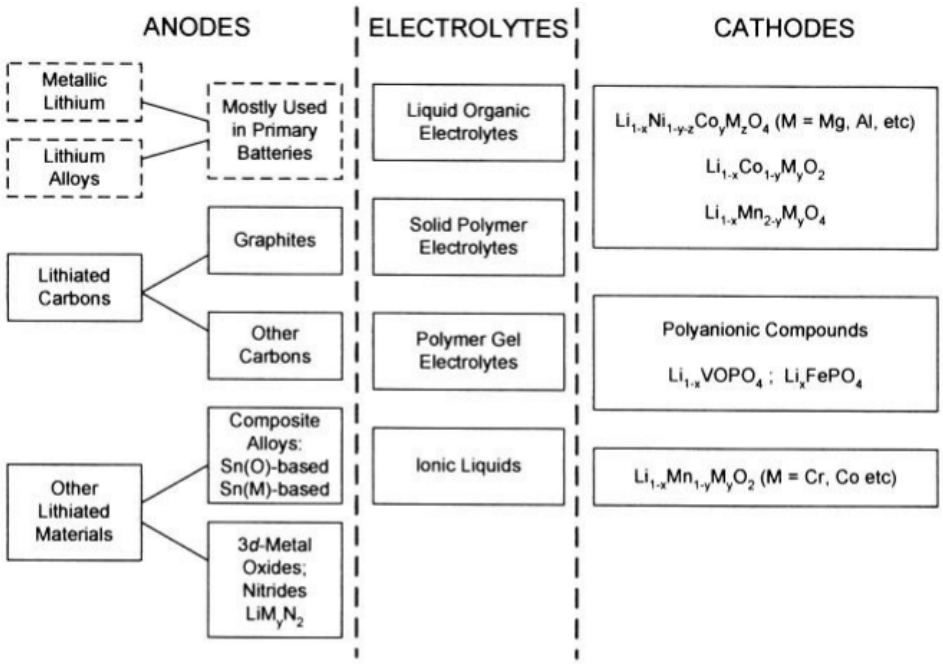

Figure 2.2: Different cathode, anode and electrolyte chemistries, which can be combined in various ways to originate numerous LIB variants, as stated in van Schalkwijk and Scrosati [35].

positive electrode material, the Korean LG and the Japanese Hitachi/Shin-Kobe are developing LIBs featuring manganese-based cathodes. Only further testing and assessment will lead to a better understanding of pros and cons of each chemistry.

2.4.1 Electrodes

Today's Li-ion cells have a carbon-based anode, usually made of graphite. A particularly suitable anode material for HEVs has been acknowledged to be hard-carbon, possessing high power density and long durability.

While the anode is generally well optimized and hardly any improvements are expected in terms of design changes, the cathode still shows promises for further enhancements. Most lithium-ion batteries for portable applications are based on a cobalt oxide ($LiCoO_2$) cathode, especially because of its high energy density. The main drawbacks are a relatively low specific power and a fast ageing process, which make them not convenient for HEV applications.

Several alternatives to cobalt cathodes have been proposed. Lithium manganese oxide cathodes in the form of a spinel structure yield high specific power. Multimetal cathodes based on lithium nickel cobalt oxide, with or without an aluminium or manganese doping, are expected to increase the specific energy. Novel systems based on the addition of phosphates in the cathode (e.g., $LiFePO_4$) are also promising.

2.4.2 Electrolyte

Like the cathode, also the electrolyte has significant potential for improving the cell performance. Furthermore, the electrochemical stability of the electrolyte plays a crucial role in maintaining the long-term reversibility of any cell chemistry, on which the durability of the battery depends.

The main requirements for an electrolyte has been stated by Xu [38]:

- it should be a good ionic conductor and electronic insulator, in order to ease the ion transport and to minimize the self-discharge;
- the potentials at which electrolyte degradation reactions occur should not fall within the range of the working potentials of both the cathode and the anode;
- it should be inert to other cell components such as cell separators, electrode substrates, and cell packaging materials;
- it should be robust against electrical, mechanical, or thermal abuses;
- its components should be environmentally friendly.

The electrolyte is typically made of a lithiated liquid solution (e.g. $LiPF_6$) dissolved in an organic solvent. A promising alternative consists of polymer electrolytes, which, however, have the drawback of low performance at low temperature, as was the case for the Li-Polymer batteries).

2.5 Safety: problems and solutions

Despite the virtues of Li-ion batteries, several factors have prevented a wider spread of this technology, and the most significant one is, without doubt, safety. In fact, the consequences of a failure event in a LIB tend to be more severe compared to other rechargeable battery chemistries. This is mainly due to the higher energy density of LIBs, which implies more heat released in case of failure, and to the flammability of the most common organic solvents used as electrolytes. The most problematic event occurs when the heat generated within a cell exceeds the heat dissipation by the cell, a phenomenon called thermal runaway.

The lack of maturity about safety concern both consumers and manufacturers, and is well described by statistics. According to Arora et al. [1], more than 2 million products containing Li-ion batteries have been recalled because of battery problems since October 2006. For successfully scaling up this technology to higher power applications like HEVs, it is imperative to reduce these concerns, i.e. to reduce the incidents and mitigate the effects of the incidents when they do occur. This is done by means of various expedients, among which a battery management system, through its thermal and charge management, plays a critical role.

2.5.1 Thermal runaway

The exothermic failure of a LIB is a rare event, yet it deserves attention because it can be highly destructive and pose a fire hazard. Whenever a charged Li-ion cell is exposed to temperatures above 60 °C, there is a risk of initiating exothermic reactions within the cell. These reactions release heat and can steadily rise the cell temperature. The point of no return is reached when the separator starts to melt, at about 180 °C. This can cause an internal short circuit, through which most of the energy stored in a cell is rapidly released in form of heat. In the worst case, the entire process can pose a fire or explosion hazard. Yet, even without that kind epilogue, it is very likely that the battery is irreversibly compromised in case of thermal runaway. There are several possible scenarios for a thermal runaway:

- external short-circuit;
- internal short-circuit, as a result of metallic contaminants (due to a poorly controlled manufacturing process), dendrite growth (i.e. deposition of needle-like lithium crystals upon charge from the electrolyte on the anode, especially if the latter is made of lithium-metal, which can reduce cell performance and pierce the separator), separator failure, mechanical abuse, or improper charging protocol;
- cell overcharge;
- cell overdischarge, which can initiate reactions that reduce the cell performance or lead to dendrite growth;
- too low or too high temperature when charging.

The last condition is primarily related to the so-called SEI layer, which is crucial for the improvement of performance and safety in LIB operation. This layer forms through electrolyte decomposition on the surface of the negative electrode at the first charge of a cell, which is normally assembled in a discharged state. On one hand, this layer provides a protective barrier between the reactive negative electrode and the electrolyte, preventing dendrite growth to develop; on the other hand, it limits the discharge rates and restricts the temperature range over which the battery may be charged. At low temperature, the rate of Li_+ transport through the SEI layer is hindered, and lithium ions can accumulate at the surface of the anode material, possibly resulting in dendrite growth. This hazard is also present at high temperature, in this case because of a possible SEI breakdown.

2.5.2 Prevention

The dangerousness of the above-mentioned events in a particular Li-ion cell highly depends on the particular chemistry of the cell. Some chemistries are more susceptible than others, and the more dangerous chemistries should be avoided for high power applications, or should be modified with appropriate additives.

Each cell should be adequately insulated from the others in the battery pack, in order to avoid the danger of chain reactions causing neighboring cells to fail due to the heat exchanged between cells.

It is responsibility of Battery Management Systems to ensure that the cells of a battery operate within their rated specifications. This can be done, for example, through cell state monitoring, charge and discharge current limiting, cooling system management, communication between the battery system and the vehicle, and state of health estimating. Also avoiding high SOC levels when the temperature is high can be desirable. In fact, the higher the state of charge of the cell is, the more likely the cell may fail when thermally stressed.

In order to minimize the risk of safety-related failures, safeguards should be adopted redundantly and at various levels, ensuring a robust chemical and mechanical battery design, controlling the quality of the manifacturing process, and employing a satisfactory electronic supervisory system.

Eventually, the development of standards to evaluate the safety performance of the resulting battery systems, will prove decisive to establish LIBs as safe energy storage devices, especially in the automotive field.

Chapter 3

Modeling

Contents

3.1 Introduction

The main task of an advanced BMS, like the one required in a HEV with a Li-ion battery, is tracking the values of a set of characteristics (i.e. the "state") of the battery, as it is operated. In order to derive useful performance and safety information, the state must include electrochemical quantities, such as concentrations of lithium ions and internal potentials, which are not directly observable, at least with the instruments usually available on a vehicle. Thus, an estimation is needed for obtaining meaningful state values, and this requires the measured data (usually voltage, current and temperature, either at cell or at battery pack level) to be matched with a mathematical model that describes the dynamics of the battery.

There are different modeling approaches, which can be classified into two main categories.

Empirical models A low order system, possibly linear, is selected as the candidate model to account for the dynamics of the battery. After taking several measurements on the latter, a set of data is chosen as representative of the

battery behaviour, and used for estimating the parameters of the model. Further measurements can be included in the process to validate the resulting model.

In this approach, parameter identification is generally not problematic, but can lead to inaccurate results, especially in the automotive environment where batteries are required to operate in a wide range of operating conditions.

The preferred empirical approach is based on RC circuit networks, which provide equivalent circuit models for the electrical behaviour of the battery. To improve accuracy, resistors and capacitors can be considered as functions of the current flow direction, SOC and temperature.

New ways of deriving empirical models have been developed by means of fuzzy logic and neural networks, which require even less a priori knowledge about the candidate battery model, and are capable of automatically adapt to the measured data.

Physics-based models A description of the battery internal transport, electrochemical and thermodynamical phenomena is given, based on physical first principles, and in accordance with a chosen set of assumptions. The resulting electrochemical models can be more accurate than the empirical ones, at the cost of increasing complexity and the number of parameters to be identified.

The dynamics of an electrochemical cell is governed by nonlinear, infinite dimensional distributed diffusive mass transport processes, and it may be too much demanding to directly use a physics-based model in a real-time estimation setting. Nonetheless, since accuracy is given highest priority in the considered context, the electrochemical approach will be retained and developed. Attention will be firstly paid to modeling a single Li-ion cell with a rigorous model, the comprehension of which is necessary for understanding how the model complexity can be subsequently reduced for online estimation purposes.

3.2 Electrochemical model

The equations presented in this section, which are thoroughly discussed by Thomas et al. [34], constitute the reference point for almost any electrochemical modeling attempt of Li-ion batteries found in the literature. The resulting model, even in its isothermal version, which will be the one here described, has demonstrated good agreement with experimental data by the authors, after an adequate validation . The form of the model presented here is not only the basis for more rigorous batteries models, which are useful in simulations for mimicking real batteries behaviour, but it also provides a starting point for deriving simpler models suited for accurate online battery state estimation, as documented by several articles on SOC estimation [8, 31, 26, 6].

In order to make the modeling of the electrochemical dynamics of intercalation electrodes tractable, J. Newman developed the porous electrode theory, which has

been successfully applied, along with concentrated solution theory, to model Li-ion cells. According to this approach, physical variables referring to an electrode are averages over a region of the electrode small with respect to the overall dimensions but large compared to the microscopic pore structure. In this way, the geometric details of the pores can be neglected, and the electrode can be treated as the superposition of two continua, i.e. the electrolytic solution and the electrode host matrix. Lithium ions at every point in space can exist either in the solid phase (intercalated in the electrode material) or in a dissolved state in the electrolyte. Furthermore, the porous structure will be thought as made up of small spherical solid particles, each one denoting a collection of interstitial sites (Figure 3.1).

For the sake of computational tractability, only three coordinates will be eventually considered: the time coordinate t, the spatial macroscopic coordinate x (along the thickness of the cell sandwich), and the spatial radial microscopic coordinate r (inside each spherical particle). The x coordinate ranges from 0 to L, where L is the length of the cell, while the r coordinate ranges from 0 to R, where R is the radius of each sphere of active material. The negative electrode, the separator and the positive electrode have an x length of L_-, L_s and L_+, respectively, while the current collectors will be thought to have negligible length. Each location on the x-axis belonging to an electrode region is associated with one spherical particle and the corresponding r-coordinate system.

Note on notation

Some quantities appear both with a normal and a bold font. A symbol with a bold font refers to a vector quantity, while without boldface it refers to the same quantity after being restrained to just one component, and thus reduced to a scalar. The context will clarify which direction this component is relative to.

3.2.1 Potential in the electrolyte

The electrolyte will be assumed to be made of a single salt in a homogeneous solvent. This choice reduces the modeling complexity while covering most of the real cases, and providing satisfactory results even when modeling electrolytes with mixtures of solvents. To simplify expressions further, a 1:1 binary electrolyte will be considered. Binary means that only two charged species can be found in the electrolytic solution, along with the solvent: Li^+ cations and X^- anions (of some species X). 1:1 means that the electrolyte's charge number, i.e. the number of elementary charges of each sign appearing on dissociation of one molecule of electrolyte, is 1. Under these assumptions, the gradient of the potential in the solution is given by :

$$\nabla\Phi_e = -\frac{\mathbf{i}_e}{\kappa} + \frac{2RT}{F}(1-t_+^o)\left(1+\frac{d\ln f_\pm}{d\ln c_e}\right)\nabla\ln c_e \tag{3.1}$$

where:

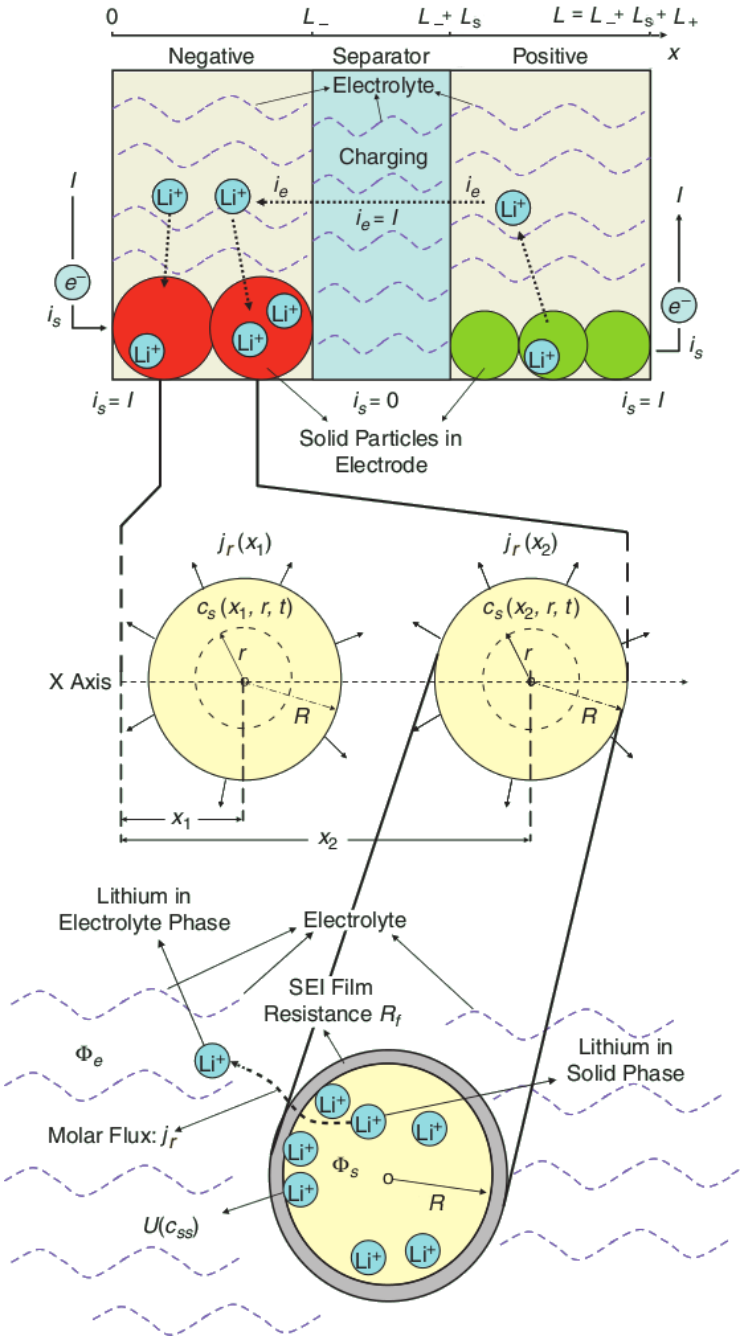

Figure 3.1: Schematic representation of the cell electrochemical model, highlighting the two different spatial coordinates x and r [6].

Φ_e is the electrical potential of the electrolytic solution phase measured with a lithium metal reference electrode in solution (V);

$\mathbf{i}_e$ is the current density in the electrolyte (A/m^2, with respect to the superficial

area[1]);

κ is the effective ionic conductivity of the electrolyte (S/m);

R is the universal gas constant ($\simeq 8.3143\,\mathrm{J/(mol\,K)}$);

T is the temperature of the cell (K);

F is the Faraday's constant, equal to the magnitude of electric charge per mole of electrons ($\simeq 96\,485\,\mathrm{C/mol}$);

t_+^o is the transference number[2] of the positive ions with respect to the solvent velocity;

$f_\pm$ is the mean ionic activity coefficient of the electrolyte, which accounts for deviations of the electrolyte solution from ideal behaviour and is a function of the electrolyte concentration;

c_e is the concentration of the electrolyte salt (mol/m^3 of solution).

In accordance with the chain rule, the last two factors can be rewritten as:

$$\left(1 + \frac{d\ln f_\pm}{d\ln c_e}\right)\nabla \ln c_e = \nabla \ln f_\pm + \nabla \ln c_e.$$

Assuming the mean ionic activity to be spatially invariant, these factors can be replaced simply by $\nabla \ln c_e$. With this adjustment, after limiting the dynamics along the x-axis Eq. 3.1 becomes:

$$\frac{\partial \Phi_e}{\partial x} = -\frac{i_e}{\kappa} + \frac{2RT}{F}(1 - t_+^o)\frac{\partial \ln c_e}{\partial x}. \tag{3.2}$$

Since only potential differences can be measured, arbitrary values can be given to Φ_e for the boundary conditions. Conventionally, it is set to zero at the positive electrode-current collector interface.

3.2.2 Transport in the electrolyte

The transport of lithium ions in the electrolyte is well described by means of concentrated solution theory. This, compared to dilute solution theory, provides a more adequate framework for modelling the interactions between solute and solvent, it fits both liquid and polymer electrolytes behaviour, and allows a greater flexibility in including further possible complexities (e.g. volume changes, polymer flow, interaction with additional species in the polymer phase).

[1] The interfacial area between the intercalant electrode material and the pore solution will be simply referred to as superficial area.

[2] The transference number, or transport number, is the fraction of the total current carried by a given ion in a solution. Ions may carry drastically different portions of the total current if their mobilities are different. However, the transport numbers of anions and cations must add up to unity.

A development of concentrated solution theory results, combined with porous electrode theory, electroneutrality and mass balance considerations, brings to the following equation:

$$\varepsilon \frac{\partial c_e}{\partial t} = \nabla \cdot \varepsilon D_e \left(1 - \frac{d \ln c_o}{d \ln c_e}\right) \nabla c_e + \frac{t_-^o \nabla \cdot \mathbf{i}_e + \mathbf{i}_e \cdot \nabla t_-^o}{F} - \nabla \cdot c_e \mathbf{v_o} + a j_- \tag{3.3}$$

where:

ε is the volume fraction of the electrolyte;

D_e is the diffusion coefficient of the lithium salt in the electrolyte (m^2/s);

c_o is the concentration of solvent in the electrolytic solution (mol/m^3);

$t_-^o = 1 - t_+^o$ is the transference number of the negative ions with respect to the solvent velocity;

$\mathbf{v}_o$ is the velocity of the solvent in the electrolytic solution (m/s);

a is the superficial area per unit of volume of electrode (1/m);

j_- is the rate of production of negative ions per unit of superficial area ($mol/(m^2\ s)$).

An expression for the divergence of the current flow in the electrolyte is obtained through Faraday's law:

$$\nabla \cdot \mathbf{i}_e = F a j_r \tag{3.4}$$

where j_r is the pore wall flux of lithium ions ($mol/(m^2\ s)$) resulting from the reaction between lithium and the sites of insertion material. If a site is represented with θ_s, this reaction can be expressed as:

$$\mathrm{Li}^+ + \mathrm{e}^- + \theta_s \rightleftharpoons \mathrm{Li} - \theta_s. \tag{3.5}$$

The term j_r accounts only for the faradaic transfer of lithium ions in the reaction, and is found by averaging over the interfacial area between the electrolyte and the solid matrix. Before being included in the final set of equations governing the current model, Eq. 3.4 is rewritten so as to account for changes only along the x-axis:

$$\frac{\partial i_e}{\partial x} = F a j_r. \tag{3.6}$$

In order to simplify Eq. 3.3, the following reasonable assumptions will be considered:

- convection in the electrolyte is negligible, as well as its corresponding term $\nabla \cdot c_e \mathbf{v_o}$;
- the anion transference number t_-^o is spatially invariant;

- side reactions are ignored, and the main reaction involves only cations, thus j_- can be assumed to be zero (otherwise, also the current flux of side reactions should be included into Eq. 3.6);
- volume and porosity of the active material are constant over time, so that no mass balance for the solvent has to be specified;
- changes in solvent concentration as the salt concentration changes are negligible, and then $d\ln c_o/d\ln c_e = 0$.

The resulting equation governing the transport in the electrolyte limited to the x-axis is:

$$\varepsilon\frac{\partial c_e}{\partial t} = \frac{\partial}{\partial x}\left(\varepsilon D_e\frac{\partial c_e}{\partial x}\right) + \left(1-t_+^o\right)aj_r. \tag{3.7}$$

Within the separator, the equation further simplifies since j_r is simply 0, and ε is equal to 1 if no inert separator material is used.

With regard to the boundary conditions, at the current collectors all of the current is transported by the matrix phase, so that $\partial c_e/\partial x = 0$, while continuity of concentration and flux must be established at the interface between the separator and each porous electrode.

3.2.3 Potential in the solid

Let $\mathbf{i}_s$ be the current density in the solid electrode phase (A/m^2, with respect to the superficial area), σ be the effective electronic conductivity of an electrode (S/m), and Φ_s be the potential in the solid phase. The variation in potential is tied to the current density by Ohm's law:

$$\mathbf{i}_s = -\sigma\nabla\Phi_s. \tag{3.8}$$

Assuming that the electric charge is conserved, and reasoning with unidimensional current densities along the x-axis with the same positive direction, the superficial current density I (A/m^2) of the cell must be equal to the sum of the current densities in the solid phase and in the electrolyte phase:

$$I = i_s + i_e. \tag{3.9}$$

With these considerations, Eq. 3.8 becomes:

$$I - i_e = -\sigma\frac{\partial\Phi_s}{\partial x}. \tag{3.10}$$

This equation requires one boundary condition for each electrode region. For galvanostatic operation, i.e. for a constant external applied current density $I_{ext} = I$, the following requirements are enforced:

$$i_e|_{x=L_-} = I \quad \text{and} \quad i_e|_{x=L} = 0. \tag{3.11}$$

For potentiostatic operation, instead, the voltage difference at the terminals of the cell is constrained to be a given value V:

$$\Phi_s|_{x=L} - \Phi_s|_{x=0} = V. \tag{3.12}$$

3.2.4 Transport in the solid

Neglecting the effects of stress and anisotropic diffusion, and the diffusion between adjacent solid particles, the mass balance for lithium ions transported in the solid phase can be accounted by an equation similar to the one used for the transport in the electrolyte:

$$\frac{\partial c_s}{\partial t} = \nabla \cdot D_s \left(1 - \frac{d \ln c_o}{d \ln c_s}\right) \nabla c_s + \frac{\mathbf{i}_s \cdot \nabla t_-^o}{z_+ \nu_+ F} - \nabla \cdot c_s \mathbf{v}_o \tag{3.13}$$

where:

c_s is the concentration of lithium in the solid particle phase ($\mathrm{mol/m^3}$);

D_s is the diffusion coefficient of lithium in the solid matrix ($\mathrm{m^2/s}$);

$\mathbf{i}_s$ is the current density ($\mathrm{A/m^2}$, with respect to the superficial area).

For most electrode materials, diffusion is the main mechanism of transport in the solid phase, and thus the last two terms of Eq. 3.13 will be omitted. Also the term $d \ln c_o / d \ln c_s$ can be considered equal to 0, under the hypothesis that the volume changes in the solid are negligible. Finally, it is convenient to rewrite the del operators in spherical coordinates, so as to express the diffusion dynamics only along the radial coordinate of each spherical particle, assuming this as the predominant phenomenon. In general, given a scalar field f and a vector field $\mathbf{A}$, the gradient of f in spherical coordinates becomes:

$$\nabla f = \frac{\partial f}{\partial r}\hat{\mathbf{r}} + \frac{1}{r}\frac{\partial f}{\partial \theta}\hat{\theta} + \frac{1}{r \sin\theta}\frac{\partial f}{\partial \phi}\hat{\phi} \tag{3.14}$$

where r is the radial distance from a prescribed origin, θ and ϕ represent the inclination and azimuth angles, and $\hat{\mathbf{r}}$, $\hat{\theta}$ and $\hat{\phi}$ are the local orthogonal unit vectors in the directions of increasing r, θ and ϕ respectively. In the same coordinates, the divergence of $\mathbf{A}$ is:

$$\nabla \cdot \mathbf{A} = \frac{1}{r^2}\frac{\partial}{\partial r}(r^2 A_r) + \frac{1}{r \sin\theta}\frac{\partial}{\partial \theta}(\sin\theta\ A_\theta) + \frac{1}{r \sin\theta}\frac{\partial A_\phi}{\partial \phi} \tag{3.15}$$

where A_r, A_θ and A_ϕ are the components of $\mathbf{A}$ along the r, θ and ϕ coordinates, respectively. Applying the aforementioned simplifications and reformulations, Eq. 3.13 becomes:

$$\frac{\partial c_s}{\partial t} = \frac{1}{r^2}\frac{\partial}{\partial r}\left(D_s r^2 \frac{\partial c_s}{\partial r}\right) \tag{3.16}$$

which is a much simpler description of the transport of lithium in the solid particle associated with each x location in each electrode. The corresponding boundary conditions are:

$$\left.\frac{\partial c_s}{\partial r}\right|_{r=0} = 0 \quad \text{and} \quad -D_s \left.\frac{\partial c_s}{\partial r}\right|_{r=R} = j_r \tag{3.17}$$

where a subscript will be added to R to discriminate between positive and negative active material particles radius, thus also avoiding any ambiguity with the universal gas constant symbol.

3.2.5 Reaction rate

The electrochemical reaction rate can be expressed in terms of concentrations and potentials through the following Butler-Volmer rate equation:

$$j_r = \frac{i_o}{F}\left[\exp\left(\frac{\alpha_a F}{RT}\eta\right) - \exp\left(\frac{\alpha_c F}{RT}\eta\right)\right] \tag{3.18}$$

where:

η is the surface overpotential, i.e. the deviation from thermodynamic potential difference between the solid and solution at the existing surface concentrations (V),

i_o is the exchange current density, i.e. the density of current in the absence of net electrolysis and at zero overpotential (A/m^2)

α_a, α_c are the anodic and cathodic transfer coefficients, i.e. the fractions of the applied overpotential which favor the anodic or cathodic direction of the overall reaction, respectively.

Eq. 3.18 sets the surface overpotential, with respect to the local potential in the electrolyte and in the solid, required to drive reaction (3.5). Mathematically, η can be defined as:

$$\eta = \Phi_s - \Phi_e - U(c_{ss}) \tag{3.19}$$

where U is the open-circuit potential (V) of the solid material, evaluated at its surface concentration with respect to a hypothetical lithium reference electrode in solution, and c_{ss} is the concentration of lithium ions (mol/m^3) at the surface of the solid particles.

As emphasized in Eq. 3.19, U is a function of lithium ions surface concentration, i.e. $c_{ss}(x,t) = c_s(x,R,t)$. The dependence of U on c_s varies considerably among different insertion materials, and has a large effect on the model performance. Thus, it is important to fit carefully this dependence on appropriate experimental data for the materials of interest.

The exchange current density is given by:

$$i_o = F r_k (c_{s,max} - c_{ss})^{\alpha_c} (c_{ss})^{\alpha_a} (c_e)^{\alpha_a} \tag{3.20}$$

where r_k is the rate constant for the anodic or cathodic direction of the reaction, while $(c_{s,max} - c_{ss})$ is the concentration of unoccupied sites in the insertion material. Attention should be paid when polymer electrolytes are used, in which case a slightly different expression for the exchange current density may be more accurate [9].

Since the reaction-rate equation is algebraic, no boundary conditions are needed.

3.2.6 Effective properties in porous materials

The values of κ (effective ionic conductivity of the electrolyte, Eq. 3.2), D_e (diffusion coefficient of the lithium salt in the electrolyte, Eq. 3.7), and σ (effective electronic conductivity of an electrode, Eq. 3.10) within a porous electrode are lower than their bulk values. This is due to the tortous path which the ions in solution must make around the solid particles, or which the electrons must make around the pores filled with electrolyte.

Generally, given a property P in a certain phase, the Bruggeman relation is used to account for volume fraction ε and tortuosity of that phase. Denoting the bulk value of P as P_∞, the Bruggeman relation states that:

$$P = \frac{\varepsilon P_\infty}{\tau} \tag{3.21}$$

where τ is the tortuosity of the phase of interest, usually related to the porosity ε by $\tau = 1/\varepsilon^{0.5}$. Because of the choices made to derive Eq. 3.7, D already gets multiplied once by ε, so that $D = D_\infty \varepsilon^{0.5}$ instead of $D_\infty \varepsilon^{1.5}$.

The calculation of the effective diffusivity and ionic conductivity of gel electrolytes, where a liquid electrolyte is absorbed into a polymer matrix, may be more complicated. Difficulties arise from the interaction of the polymer both with the electrolyte solvent and salt, and from the increased tortuosity of the polymer. One way to deal empirically with this issues is to treat the tortuosity as an adjustable parameter fit to measurements of diffusivity in actual gels.

Finally, a parameter affecting the overall electronic conductivity of a composite electrode is the weight fraction of conductive filler. Conductive fillers are used to maintain contact among active material particles and hence to reduce ohmic losses in the electrodes. If also the conductive filler is going to be included in the model, their effect on electronic conductivity must be determined experimentally.

3.2.7 Equations summary

The equations presented in the previous sections involve three ordinary differential equations (Eq. 3.2, 3.10 and 3.6), two partial differential equations (Eq. 3.7 and 3.16), and one algebraic equation (Eq. 3.18). The whole set of equations pertains to each of the two electrode regions, while the separator requires only a simplified subset of them. In fact, the separator does not involve equations concerning the solid-phase intercalation dynamics, $j_r = 0$, and $i_e = I$. All of the resulting equations are listed in Tables 3.3, 3.2 and 3.1, where the subscripts p, sep and n

are used to denote quantities belonging either to the positive electrode, to the separator or to the negative electrode domain, respectively. The x-axis coordinate for the negative electrode-separator interface is called x_n, which is equal to L_-, while for the separator-positive electrode the symbol x_p, equal to $L_- + L_s$, is used.

Given a particular charge/discharge mode (e.g. for a specified external current, cell voltage, power or load), the variables c_s (concentration of lithium in the solid particle phase), c_e (concentration of lithium salt in the electrolyte phase), Φ_s (potential in the solid phase), Φ_e (potential in the electrolyte phase), i_e (current density in the electrolyte) and j_r (pore wall flux of lithium ions) can be computed by means of these equations. Boundary conditions are expressed according to the choice of considering the external current density I as the input to the model, while the voltage of the cell $V = \Phi_s|_{x=L} - \Phi_s|_{x=0}$ will be considered the output. Besides the input current, also the initial conditions (relative to the first instant) for c_s and c_e must be specified.

Negative electrode governing equations ($0 \leq x \leq x_n$)			
Eq. no	Equation	Boundary conditions	
	Electrolytic-phase Ohm's law		
(3.2)	$i_e = -\kappa_n \dfrac{\partial \Phi_e}{\partial x} + \dfrac{2\kappa_n RT}{F}(1 - t_+^o)\dfrac{\partial \ln c_e}{\partial x}$	$\Phi_e\big\vert_{x=0}$	$= 0$
		$-\kappa_n \dfrac{\partial \Phi_e}{\partial x}\Big\vert_{x=x_n^-}$	$= -\kappa_{sep} \dfrac{\partial \Phi_e}{\partial x}\Big\vert_{x=x_n^+}$
	Electrolyte material balance		
(3.7)	$\varepsilon_n \dfrac{\partial c_e}{\partial t} = \dfrac{\partial}{\partial x}\left(\varepsilon_n D_{e,n} \dfrac{\partial c_e}{\partial x}\right) + (1 - t_+^o)\, a_n j_r$	$\varepsilon_n D_{e,n} \dfrac{\partial c_e}{\partial x}\Big\vert_{x=0}$	$= 0$
		$\varepsilon_n D_{e,n} \dfrac{\partial c_e}{\partial x}\Big\vert_{x=x_n^-}$	$= \varepsilon_{sep} D_{e,sep} \dfrac{\partial c_e}{\partial x}\Big\vert_{x=x_n^+}$
	Solid-phase Ohm's law		
(3.10)	$I - i_e = -\sigma_n \dfrac{\partial \Phi_s}{\partial x}$	$-\sigma_n \dfrac{\partial \Phi_s}{\partial x}\Big\vert_{x=0}$	$= I$
		$-\sigma_n \dfrac{\partial \Phi_s}{\partial x}\Big\vert_{x=x_n}$	$= 0$
	Solid material balance		
(3.16)	$\dfrac{\partial c_s}{\partial t} = \dfrac{1}{r^2}\dfrac{\partial}{\partial r}\left(D_{s,n} r^2 \dfrac{\partial c_s}{\partial r}\right)$	$D_{s,n} \dfrac{\partial c_s}{\partial r}\Big\vert_{r=0}$	$= 0$
		$D_{s,n} \dfrac{\partial c_s}{\partial r}\Big\vert_{r=R_n}$	$= -j_r$
	Charge conservation		
(3.6)	$\dfrac{\partial i_e}{\partial x} = F a_n j_r$	$i_e\big\vert_{x=0}$	$= 0$
		$\dfrac{\partial i_e}{\partial x}\Big\vert_{x=x_n}$	$= 0$
	Butler-Volmer insertion kinetics		
(3.18)	$j_r = \dfrac{i_{o,n}}{F}\left[\exp\left(\frac{\alpha_{a,n} F}{RT}\eta_n\right) - \exp\left(\frac{\alpha_{c,n} F}{RT}\eta_n\right)\right]$		—
	where $\eta_n = \Phi_s - \Phi_e - U_n(c_{ss}) - F R_{f,n} j_r$		

Table 3.1: Set of governing equations for the negative electrode.

Separator governing equations ($x_n \leq x \leq x_p$)			
Eq. no	Equation	Boundary conditions	
	Electrolytic-phase Ohm's law		
(3.2)	$I = -\kappa_{sep}\frac{\partial \Phi_e}{\partial x} + \frac{2\kappa_{sep}RT}{F}(1-t_+^o)\frac{\partial \ln c_e}{\partial x}$	$\Phi_e\big\vert_{x=x_n^-}$	$= \Phi_e\big\vert_{x=x_n^+}$
		$\Phi_e\big\vert_{x=x_p^-}$	$= \Phi_e\big\vert_{x=x_p^+}$
	Electrolyte material balance		
(3.7)	$\varepsilon_{sep}\frac{\partial c_e}{\partial t} = \frac{\partial}{\partial x}\left(\varepsilon_{sep}D_{e,sep}\frac{\partial c_e}{\partial x}\right)$	$c_e\big\vert_{x=x_n^-}$	$= c_e\big\vert_{x=x_n^+}$
		$c_e\big\vert_{x=x_p^-}$	$= c_e\big\vert_{x=x_p^+}$

Table 3.2: Set of governing equations for the separator.

Positive electrode governing equations ($x_p \leq x \leq L$)			
Eq. no	Equation	Boundary conditions	
	Electrolytic-phase Ohm's law		
(3.2)	$i_e = -\kappa_p \frac{\partial \Phi_e}{\partial x} + \frac{2\kappa_p RT}{F}(1-t_+^o)\frac{\partial \ln c_e}{\partial x}$	$\Phi_e\vert_{x=L}$	$= 0$
		$-\kappa_p \frac{\partial \Phi_e}{\partial x}\Big\vert_{x=x_p^+}$	$= -\kappa_{sep}\frac{\partial \Phi_e}{\partial x}\Big\vert_{x=x_p^-}$
	Electrolyte material balance		
(3.7)	$\varepsilon_p \frac{\partial c_e}{\partial t} = \frac{\partial}{\partial x}\left(\varepsilon_p D_{e,p}\frac{\partial c_e}{\partial x}\right) + (1-t_+^o)\, a_p j_r$	$\varepsilon_p D_{e,p}\frac{\partial c_e}{\partial x}\Big\vert_{x=L}$	$= 0$
		$\varepsilon_p D_{e,p}\frac{\partial c_e}{\partial x}\Big\vert_{x=x_p^+}$	$= \varepsilon_{sep} D_{e,sep}\frac{\partial c_e}{\partial x}\Big\vert_{x=x_p^-}$
	Solid-phase Ohm's law		
(3.10)	$I - i_e = -\sigma_p \frac{\partial \Phi_s}{\partial x}$	$-\sigma_p \frac{\partial \Phi_s}{\partial x}\Big\vert_{x=L}$	$= I$
		$-\sigma_p \frac{\partial \Phi_s}{\partial x}\Big\vert_{x=x_p}$	$= 0$
	Solid material balance		
(3.16)	$\frac{\partial c_s}{\partial t} = \frac{1}{r^2}\frac{\partial}{\partial r}\left(D_{s,p} r^2 \frac{\partial c_s}{\partial r}\right)$	$D_{s,p}\frac{\partial c_s}{\partial r}\Big\vert_{r=0}$	$= 0$
		$D_{s,p}\frac{\partial c_s}{\partial r}\Big\vert_{r=R_p}$	$= -j_r$
	Charge conservation		
(3.6)	$\frac{\partial i_e}{\partial x} = F a_p j_r$	$i_e\vert_{x=L}$	$= 0$
		$\frac{\partial i_e}{\partial x}\Big\vert_{x=x_p}$	$= 0$
	Butler-Volmer insertion kinetics		
(3.18)	$j_r = \frac{i_{o,p}}{F}\left[\exp\left(\frac{\alpha_{a,p}F}{RT}\eta_p\right) - \exp\left(\frac{\alpha_{c,p}F}{RT}\eta_p\right)\right]$		—
	where $\eta_p = \Phi_s - \Phi_e - U_p(c_{ss}) - FR_{f,p}j_r$		

Table 3.3: Set of governing equations for the positive electrode.

3.3 Reduced electrochemical model

In view of tackling real-time SOC estimation, a simpler model than the one presented before is needed. Several procedures have been proposed in the literature to reduce the rigorous model to a finite-dimensional low-order system, suited for real-time applications. A brief selection of such models is reported below. These models share the assumptions made for the rigourous model, like the absence of thermal dynamics or capacity fading with cycling, adding further assumptions to allow the development of a mathematically simpler set of equations.

Single particle model with polynomial approximation [27] Each electrode is represented by a single spherical particle, whose area is equivalent to that of the active area of the solid phase in the porous electrode. The dynamics of the solution phase, and thus the resulting limitations, are neglected. The solid phase concentration is represented by a second order polynomial, whose coefficients depend on the average and superficial concentrations, hence the dependence on the radial variable in each particle is eliminated.

Porous electrode model with polynomial approximation [27] The complexity of the rigorous model is mostly retained, since the spatial distribution of concentrations and potentials along the thickness of the electrode, both in solid and in solution phase, are taken into account. The only difference is how the r dynamics is treated: similarly to the single particle model, the concentration within each spherical particle of each electrode is assumed to have a parabolic profile.

Model reduced in the frequency domain [31] A complex procedure is implemented for identifying a low-order model from the infinite-dimensional frequency response of the rigourous model. Several local linear models, corresponding to a range of interest of cell operating conditions, are combined into an approximate global nonlinear model, exploiting the physical knowledge of the system.

Electrode averaged model [8] The spatial solid concentration distribution along the x coordinate in both electrodes is neglected, while the diffusion dynamics along the r coordinate is considered only inside a representative solid material particle, one for each electrode. The electrolyte concentration is assumed to be constant, which is reasonable for high concentrated electrolytes.

Different mathematical techniques are used in these reduction approaches, such as spatial discretizations, either in the x or in the r direction, linear or volume averaging of variables, reformulations, linearizations and possibly frequency domain considerations. The reduced complexity resulting from the adoption of each one of these mathematical devices can be varyingly acceptable, depending on the application requirements, on the chemistry considered and on the operating conditions of interest.

Among the cited models, the last one, developed by C. Speltino, appears to be an attractive compromise between simplicity and accuracy for real-time SOC estimation of Li-ion cells operated under high currents rates [33]. In fact, by capturing the diffusion dynamics in the solid particles, it is able to represent the most essential and limiting phenomenon in those circumstances, with respect to which other processes like electrolyte concentration dynamics or nonuniform distribution of variables along the x axis are less significant. This is especially satisfactory for cells with thin electrodes (used when power is preferred over energy) and with highly concentrated electrolytes.

3.3.1 Derivation of the Electrode Averaged Model (EAM)

First, let consider the governing equation of the transport of lithium in the solid particle associated with each x location in each electrode (Eq. 3.16):

$$\frac{\partial c_s}{\partial t} = \frac{1}{r^2}\frac{\partial}{\partial r}\left(D_s r^2 \frac{\partial c_s}{\partial r}\right) = D_s\left(\frac{2}{r}\frac{\partial c_s}{\partial r} + \frac{\partial^2 c_s}{\partial r^2}\right) \tag{3.22}$$

which describes how diffusion causes the concentration field of lithium ions to change with time inside each solid particle. The corresponding boundary conditions are:

$$\left.\frac{\partial c_s}{\partial r}\right|_{r=0} = 0 \quad \text{and} \quad -D_s \left.\frac{\partial c_s}{\partial r}\right|_{r=R} = j_r \tag{3.23}$$

where a subscript will be added to R to denote whether the positive or the negative active material particles radius is being referred to.

According to the notation used by Di Domenico et al. [8], the pore wall flux of lithium ions j_r (mol/(m^2 s)) will be replaced by j^{Li} (A/m^3), which still quantifies the flux of lithium ions transferred in the intercalation process, but in terms of charge per second per unit of volume and not in terms of moles exchanged per unit of superficial area of intercalant material. j_r and j^{Li} are related by:

$$j^{Li} = F a j_r \tag{3.24}$$

where F is the electrical charge per mole and a is the average superficial area per unit of electrode volume, as written before. The second boundary condition of Eq. 3.16 can be easily rewritten as:

$$-D_s \left.\frac{\partial c_s}{\partial r}\right|_{r=R} = \frac{j^{Li}}{aF}. \tag{3.25}$$

In order to achieve a state-space representation of the system dynamics, the partial differential equation 3.16 is first cast into a set of ordinary differential equations through a discretization process called the method of lines. This numerical method is a technique for solving partial differential equations by discretizing in all but one dimension, and then integrating the semi-discrete problem as a system of

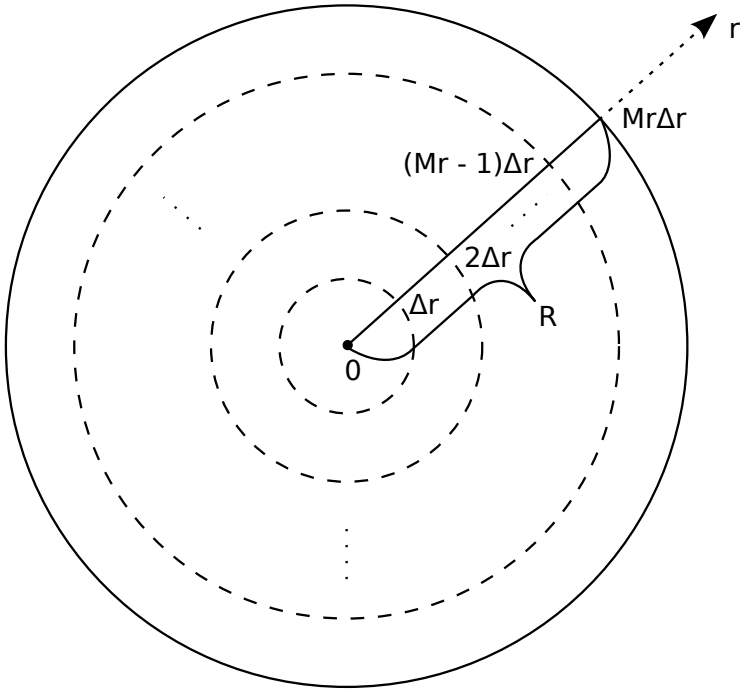

Figure 3.2: Schematic representation of the radial discretization used in the Electrode Averaged Model.

ODEs or DAEs. In this case, only the radial dimension is discretized, while, at least for the moment, the time is considered a continuous variable. No mention is made of the x dimension, because it will eventually be neglected through the averaging calculations explained below.

In the discretization process, the spherical partical radius of length R is divided into M_r slices, each of size $\Delta r = R/M_r$ (Figure 3.2). By denoting with c_{sq} the solid concentration at the radial coordinate $\Delta r \cdot q$, for q integer ranging from 1 to $M_r - 1$, the state vector associated to the original PDE for a given x coordinate is:

$$\mathbf{c_s} = \begin{bmatrix} c_{s1} & c_{s2} & \cdots & c_{sq} & \cdots & c_{s(M_r-1)} \end{bmatrix}'.$$

The concentration for $r = 0$, i.e. c_{s0}, is not included in the state vector, since its dynamics is restricted to a constant by the first of the two boundaries conditions of Eq. 3.23. The other boundary condition restrains the concentration for $r = M_r \Delta r = R$, i.e. c_{sM_r}, which also does not appear in the state vector, and corresponds to the surface concentration previous called c_{ss}. An approximated value can be given to c_{sM_r} by assuming that $\partial c_s / \partial r$ is constant and equal to the boundary value of

Eq. 3.25. In this case:

$$\begin{aligned} c_{ss} = c_{sM_r} &= c_{s(M_r-1)} + \int_{(M_r-1)\Delta r}^{M_r\Delta r} \frac{\partial c_s}{\partial r}\, dr \\ &\simeq c_{s(M_r-1)} - \frac{\Delta r}{D_s a F} j^{Li} \end{aligned} \tag{3.26}$$

Using first- and second-order finite differences to treat first and second partial derivatives, for a given x in the electrodes domain Eq. 3.22 becomes:

$$\begin{aligned} \dot{c}_{sq} &= D_s \left(\frac{2}{q\Delta r} \frac{c_{s(q+1)} - c_{s(q-1)}}{2\Delta r} + \frac{c_{s(q+1)} - 2c_{sq} + c_{s(q-1)}}{(\Delta r)^2} \right) \\ &= \frac{D_s}{(\Delta r)^2} \left(\frac{q+1}{q} c_{s(q+1)} - 2c_{sq} + \frac{q-1}{q} c_{s(q-1)} \right) \end{aligned} \tag{3.27}$$

for $q = 1, \cdots, M_r - 1$. In particular, for $q = M_r - 1$ this expression can be combined with Eq. 3.26 and rewritten to emphasize the actual coefficients for the state variables and for j^{Li} (which eventually will take the role of the input of the system):

$$\begin{aligned} \dot{c}_{s(M_r-1)} &= \frac{D_s}{(\Delta r)^2} \left[\frac{M_r}{M_r - 1} \left(c_{s(M_r-1)} - \frac{\Delta r}{D_s a F} j^{Li} \right) - 2c_{s(M_r-1)} + \frac{M_r - 2}{M_r - 1} c_{s(M_r-2)} \right] \\ &= \frac{D_s}{(\Delta r)^2} \frac{M_r - 2}{M_r - 1} \left(c_{s(M_r-2)} - c_{s(M_r-1)} \right) - \frac{M_r}{M_r - 1} \frac{1}{aF\Delta r} j^{Li}. \end{aligned} \tag{3.28}$$

The resulting state-space update equation is:

$$\begin{bmatrix} \dot{c}_{s1} \\ \dot{c}_{s2} \\ \\ \vdots \\ \\ \\ \dot{c}_{s(M_r-2)} \\ \dot{c}_{s(M_r-1)} \end{bmatrix} = \frac{D_s}{(\Delta r)^2} \begin{bmatrix} -2 & 2 & 0 & 0 & \cdots & & 0 \\ 1/2 & -2 & 3/2 & 0 & \cdots & & 0 \\ & & & & & & \\ \vdots & & & & \ddots & & \vdots \\ & & & & & & \\ & & & & & & \\ 0 & & \cdots & 0 & \frac{M_r-3}{M_r-2} & -2 & \frac{Mr-1}{Mr-2} \\ 0 & & \cdots & 0 & 0 & \frac{M_r-2}{M_r-1} & -\frac{Mr-2}{Mr-1} \end{bmatrix} \begin{bmatrix} c_{s1} \\ c_{s2} \\ \\ \vdots \\ \\ \\ c_{s(M_r-2)} \\ c_{s(M_r-1)} \end{bmatrix}$$

$$+ \begin{bmatrix} 0 & 0 & \cdots & 0 & -\left(\frac{M_r}{M_r-1} \frac{1}{aF\Delta r} \right) \end{bmatrix}' j^{Li} \tag{3.29}$$

or, equivalently, in a more compact form:

$$\dot{\mathbf{c}}_\mathbf{s} = A\mathbf{c}_\mathbf{s} + Bj^{Li} \tag{3.30}$$

where $A \in \mathbb{R}^{(M_r-1)\times(M_r-1)}$ and $B \in \mathbb{R}^{(M_r-1)\times 1}$ are the coefficients of the state

vector and j^{Li}, respectively, in Eq. 3.29. The cell voltage, designated as the only output of the system, is defined as follow:

$$V = \Phi_s(L) - \Phi_s(0) + R_f I \tag{3.31}$$

where $R_f I$ is a resistive modeling component proportional to the applied current density I with proportionality constant R_f, which represents the overall film resistance on the electrodes surface. Moreover, given the definition of overpotential (Eq. 3.19):

$$\eta(x) = \Phi_s(x) - \Phi_e(x) - U(c_{ss}(x))$$

the cell voltage can be expressed in an alternative form:

$$V = \eta_p(L) - \eta_n(0) + \Phi_e(L) - \Phi_e(0) + U_p(c_{ss}(L)) - U_n(c_{ss}(0)) + R_f I \tag{3.32}$$

which will proof to be useful further on.

The model simplification accomplished so far has not led to a sufficiently convenient system representation yet. First, after discretizing the width of the two electrodes domain into a finite number N_x of points (as high as the the desired precision requires), there will be N_x equations like 3.30, since both j^{Li} and the state vector depend on x. However small N_x is taken, the overall set of coupled dynamical equations would be hardly cast into a usable form for real-time control and estimation purposes. Second, j^{Li} depends also on the surface concentration (see the Butler-Volmer equation 3.18), and consequently on a subset of the state variables, while it would be desirable to correlate j^{Li} only with the external applied current, so that it could be used as the input to the system. Finally, the output of Eq. 3.31 is not clearly expressed as a function of the chosen input and state variables.

One way to deal with these issues is by neglecting the solid concentration distribution along the electrodes and considering the material diffusion only inside a representative solid material particle, one for each electrode. The procedure, as presented by Di Domenico et al. [8], is based on the linear averaging of the variables involved in the model, starting with the flux density j^{Li}. Expliciting the dependence on the x coordinate, the current density in the electrolyte i_e at the negative electrode-separator interface can be rewritten as:

$$\begin{aligned} i_e(x_n) &= i_e(0) + \int_0^{x_n} \frac{\partial i_e(x')}{\partial x'}\, dx' \\ &= \int_0^{x_n} j^{Li}(x')\, dx' \\ &= I \end{aligned} \tag{3.33}$$

where the boundary conditions for i_e:

$$i_e(0) = I \qquad\qquad i_e(x_n) = 0$$

and the charge conservation equation 3.6:

$$\frac{\partial i_e(x')}{\partial x'} = j^{Li}(x')$$

have been exploited. It is now straightforward to calculate the average value of j^{Li} along the negative electrode, which will be denoted with $\bar{j}_n^{Li}$:

$$\bar{j}_n^{Li} = \frac{1}{x_n}\int_0^{x_n} j^{Li}(x')\,dx' = \frac{I}{L_-} \tag{3.34}$$

yielding a convenient algebraic relation between the flux density and the input. A similar calculation can be done also for the average positive flux density $\bar{j}_p^{Li}$:

$$\begin{aligned} i_e(L) &= i_e(x_p) + \int_{x_p}^{L} j^{Li}(x')\,dx' = I + \int_{x_p}^{L} j^{Li}(x')\,dx' = 0 \\ \bar{j}_p^{Li} &= \frac{1}{L - x_p}\int_{x_p}^{L} j^{Li}(x')\,dx' = -\frac{I}{L_+}. \end{aligned} \tag{3.35}$$

By replacing $j^{Li}(x)$ with $\bar{j}_n^{Li}$ or $\bar{j}_p^{Li}$, depending on which electrode domain x belongs to, the simplification of the state representation is straightforward:

$$\begin{aligned} \dot{\bar{\mathbf{c}}}_{\mathbf{sn}} &= A_n \bar{\mathbf{c}}_{\mathbf{sn}} + B_n \bar{j}_n^{Li} \\ \dot{\bar{\mathbf{c}}}_{\mathbf{sn}} &= A_p \bar{\mathbf{c}}_{\mathbf{sp}} + B_p \bar{j}_p^{Li} \end{aligned} \tag{3.36}$$

where $\bar{\mathbf{c}}_{\mathbf{sn}}$ and $\bar{\mathbf{c}}_{\mathbf{sp}}$ are the state vectors of the average solid concentration dynamics inside the negative and the positive solid particles, respectively. A subscript has been added to the matrices A and B for taking into account possible differences between anodic and cathodic parameters (i.e. the diffusional coefficient D_s, the radial step size ΔR, and the superficial specific area a). Similar considerations lead to redefine the superficial concentrations for the negative and the positive electrode as follows:

$$\bar{c}_{ssn} = \bar{c}_{sn_{(M_r-1)}} - \frac{\Delta r_n}{D_{sn} a_n F}\bar{j}_n^{Li} \tag{3.37}$$

$$\bar{c}_{ssp} = \bar{c}_{sp_{(M_r-1)}} - \frac{\Delta r_p}{D_{sp} a_p F}\bar{j}_p^{Li}. \tag{3.38}$$

Also the determination of current densities and potentials simplify significantly. Starting with the anode ($0 \le x \le x_n$), the current density in the electrolyte simply becomes proportional to x with $\bar{j}_p^{Li}$ as the proportionally constant:

$$i_e(x) \simeq i_e(0) + \int_0^{x} \bar{j}_n^{Li}\,dx' = \frac{I}{L_-}x \tag{3.39}$$

while the potential in the electrolyte, combining Eqs. 3.2 and 3.39, exhibits a

quadratic dependence on x:

$$\begin{aligned}\Phi_e(x) &= \Phi_e(0) + \int_0^x \frac{\partial \Phi_e(x')}{\partial x'}\, dx' \\ &\simeq \Phi_e(0) - \int_0^x \frac{i_e(x')}{\kappa_n} \\ &= \Phi_e(0) - \frac{\bar{j}_n^{Li}}{\kappa_n}\frac{x'^2}{2}\bigg|_0^x \\ &= \Phi_e(0) - \frac{I}{2\kappa_n L_-}x^2 \end{aligned} \tag{3.40}$$

where the logarithmic term in Eq. 3.2 has been dropped, being c_e constant. Equations for the electrolytic current density and potential in the cathode ($x_p \le x \le L$) can be developed in a similar way:

$$i_e(x) \simeq i_e(x_p) + \int_{x_p}^x \bar{j}_p^{Li}\, dx' = I - \frac{I}{L_+}(x - x_p) \tag{3.41}$$

$$\begin{aligned}\Phi_e(x) &= \Phi_e(x_n) + \int_{x_n}^{x_p} \frac{\partial \Phi_e(x')}{\partial x'}\, dx' + \int_{x_p}^x \frac{\partial \Phi_e(x')}{\partial x'}\, dx' \\ &\simeq \Phi_e(0) - \frac{I}{2\kappa_n L_-}(L_-)^2 - \int_{x_n}^{x_p} \frac{I}{\kappa_{sep}}\, dx' - \int_{x_p}^x \frac{i_e(x')}{\kappa_p}\, dx' \\ &= \Phi_e(0) - \frac{I}{2\kappa_n}L_- - \frac{I}{\kappa_{sep}}(x_p - x_n) - \frac{1}{\kappa_p}\left(I\, x'|_{x_p}^x + \bar{j}_p^{Li}\frac{(x' - x_p)^2}{2}\bigg|_{x_p}^x \right) \\ &= \Phi_e(0) - \frac{I}{2\kappa_n}L_- - \frac{I}{\kappa_{sep}}L_s - \frac{I}{\kappa_p}\left((x - x_p) - \frac{(x - x_p)^2}{2L_+} \right). \end{aligned} \tag{3.42}$$

In view of deriving a new and more convenient cell voltage equation, it is useful to evaluate an averaged expression also for the overpotentials and for the potential difference $\Phi_e(L) - \Phi_e(0)$. The latter one easily follows from Eqs. 3.40 and 3.42:

$$\begin{aligned}\Phi_e(L) - \Phi_e(0) &\simeq -\frac{I}{2\kappa_n}L_- - \frac{I}{\kappa_{sep}}L_s - \frac{I}{\kappa_p}\left((L - x_p) - \frac{(L - x_p)^2}{2L_+} \right) \\ &= -I\left(\frac{L_-}{2\kappa_n} + \frac{L_s}{\kappa_{sep}} + \frac{L_+}{2\kappa_p} \right). \end{aligned} \tag{3.43}$$

An average value of the negative and positive overpotentials, i.e. $\bar{\eta}_n$ and $\bar{\eta}_p$, can be deduced from the mean flux densities through the Butler-Volmer equation 3.18:

$$\begin{aligned}\bar{j}_n^{Li} &= a_n i_{o,n}\left[\exp\left(\frac{\alpha_a F}{RT}\bar{\eta}_n \right) - \exp\left(\frac{-\alpha_c F}{RT}\bar{\eta}_n \right) \right] \\ \bar{j}_p^{Li} &= a_p i_{o,p}\left[\exp\left(\frac{\alpha_a F}{RT}\bar{\eta}_p \right) - \exp\left(\frac{-\alpha_c F}{RT}\bar{\eta}_p \right) \right] \end{aligned} \tag{3.44}$$

where the exchange current densities $i_{o,n}$ and $i_{o,p}$ are defined according to Eq. 3.20.

Assuming that the anodic and cathodic transfer coefficients α_a and α_c have the same value α, and introducing the two following auxiliary variables:

$$\begin{aligned}\xi_n &\triangleq \frac{\bar{j}_n^{Li}}{2a_n i_{o,n}} = \frac{1}{2}\left[\exp\left(\frac{\alpha F}{RT}\bar{\eta}_n\right) - \exp\left(\frac{-\alpha F}{RT}\bar{\eta}_n\right)\right] = \sinh\left(\frac{\alpha F}{RT}\bar{\eta}_n\right)\\ \xi_p &\triangleq \frac{\bar{j}_p^{Li}}{2a_p i_{o,p}} = \frac{1}{2}\left[\exp\left(\frac{\alpha F}{RT}\bar{\eta}_p\right) - \exp\left(\frac{-\alpha F}{RT}\bar{\eta}_p\right)\right] = \sinh\left(\frac{\alpha F}{RT}\bar{\eta}_p\right)\end{aligned} \tag{3.45}$$

the average overpotentials can be explicited in terms of the ξ's (and ultimately, in terms of the $\bar{j}^{Li}$'s) by inverting the hyperbolic sines:

$$\begin{aligned}\bar{\eta}_n &= \frac{RT}{\alpha F}\ln\left(\xi_n + \sqrt{\xi_n^2+1}\right)\\ \bar{\eta}_p &= \frac{RT}{\alpha F}\ln\left(\xi_p + \sqrt{\xi_p^2+1}\right).\end{aligned} \tag{3.46}$$

Eventually, the output of the system can be rewritten in terms of the average quantities introduced so far, starting from Eq. 3.32:

$$\begin{aligned}V &= \eta_p(L) - \eta_n(0) + \Phi_e(L) - \Phi_e(0) + U_p(c_{ss}(L)) - U_n(c_{ss}(0)) + R_f I\\ &\simeq \bar{\eta}_p - \bar{\eta}_n - I\left(\frac{L_-}{2\kappa_n} + \frac{L_s}{\kappa_{sep}} + \frac{L_+}{2\kappa_p}\right) + U_p(\bar{c}_{ssp}) - U_n(\bar{c}_{ssn}) + R_f I.\end{aligned} \tag{3.47}$$

In view of easing the model identification procedure, which will be the subject of the next section, the conductivity coefficients κ_n, κ_p and κ_{sep} are replaced by a single conductivity value κ, which reduces the total number of parameters to estimate without introducing practically significant imprecisions.

3.4 Model identification

Before any model may be successfully used in any real application, it is essential to find adequate values for its parameters. More specifically, parameters are usually chosen to optimally fit a convenient series of input/output data generated by the real system to be modeled. The word "optimally" implies the minimization of a cost function to be specified, which is related to the discrepancy between simulated and real data.

With regards to the simplified Li-ion cell model developed in the previous section, parameter identification may reveal itself to be a hard task, given the number of parameters and the two open-circuit potential (OCP) functions, i.e. $U_p(\bar{c}_{ssp})$ and $U_n(\bar{c}_{ssn})$, to be estimated. Since only the difference of the latter two quantities is observable from the output, observability issues can arise, motivating the need for a further simplification of the model as explained in the next chapter, when the SOC concept will be introduced.

From now on, it will be assumed that the chemistry of the electrodes in the Li-ion cell of interest is known, and that nominal data for the corresponding elec-

trochemical parameters and open-circuit potentials already exist. Unfortunately, Li-ion battery manufacturers are not always willing to provide detailed information about the chemistry of their products. For accurate OCP's estimation, a half-cell setup with a reference electrode is necessary to discriminate between the two functions. This possibility may not be viable with an already manufactured cell. In this case, a parametric model for the OCP functions can be used, reducing the function estimation problem to a parameter estimation problem. Alternatively, a set of guesses can be tried with a statistical hypothesis testing approach, exploiting the OCP functions of cathodes and anodes already available in the literature.

Table 3.4 reports all of the parameters used in the EAM, either to be estimated, to be measured, or to be fixed before the identification process. One further parameter that should be taken into account in real situations is the cell plate area for calculating the input current density. However, in the present framework the current density will be always assumed to be directly available, thus avoiding any reference to the above mentioned area in the estimation process.

The most natural choice for addressing the above grey-box identification problem is an iterative prediction-error minimization (PEM) (maximum likelihood) algorithm. For the simulations that follow, the Levenberg-Marquardt method implemented in the Matlab System Identification Toolbox has been adopted. This nonlinear least-squares regression technique minimizes the cost function:

$$f_c \triangleq \frac{\tilde{\mathbf{y}}'\tilde{\mathbf{y}}}{N} \tag{3.48}$$

where $\tilde{\mathbf{y}}$ is the column matrix of residual errors (i.e. the differences between measured and simulated outputs at corresponding sampling instants) and N is the total number of samples. This algorithm is a very popular choice for solving generic curve-fitting problems, and has already been successfully used in the context of fitting the charge and discharge data of a Li-ion cell for parameter estimation by Santhanagopalan et al. [28], even if for a different reduced model.

Below, the steps for accomplishing the identification of the EAM for a cell of a lithium-ion HEV battery pack are summarized, along with a simulation exemplification.

Parameters to be estimated		
Description	**Symbol**	**Nominal value[a]**
Concentration of electrolyte	c_e	$1000\,\mathrm{mol/m^3}$
Max solid concentration in the anode	$c_{s,max,n}$	$24\,983.7\,\mathrm{mol/m^3}$
Max solid concentration in the cathode	$c_{s,max,p}$	$51\,218.8\,\mathrm{mol/m^3}$
Reaction rate constant for negative reaction	$r_{k,n}$	1×10^{-5}
Reaction rate constant for positive reaction	$r_{k,p}$	3×10^{-11}
Conductivity of the salt	κ	$0.181\,504\,\mathrm{S/m}$
Negative particle radius	R_n	$1 \times 10^{-5}\,\mathrm{m}$
Positive particle radius	R_p	$1 \times 10^{-5}\,\mathrm{m}$
Negative electrode thickness	L_-	$10 \times 10^{-5}\,\mathrm{m}$
Positive electrode thickness	L_+	$10 \times 10^{-5}\,\mathrm{m}$
Separator thickness	L_{sep}	$2.5 \times 10^{-5}\,\mathrm{m}$
Negative active surface area per electrode unit volume	a_n	$1.8 \times 10^5\,1/\mathrm{m}$
Positive active surface area per electrode unit volume	a_p	$1.5 \times 10^5\,1/\mathrm{m}$
Negative solid phase diffusion coefficient	$D_{s,n}$	$3.9 \times 10^{-14}\,\mathrm{m^2/s}$
Positive solid phase diffusion coefficient	$D_{s,p}$	$1 \times 10^{-13}\,\mathrm{m^2/s}$
Film resistance at electrode surface	R_f	$1 \times 10^{-5}\,\Omega$
Fixed[b] parameters and constants		
Description	**Symbol**	**Value**
Number of radial discrete points	M_r	$M_r \geq 3, M_r \in \mathbb{N}$
Anodic/Cathodic transfer coefficient[c]	α	0.5
Temperature	T	$298\,\mathrm{K}$
Faraday constant	F	$96\,485.3\,\mathrm{C/mol}$
Universal gas constant	R	$8.314\,47\,\mathrm{J/(mol\,K)}$

[a] for a Li-ion cell with a $LiCoO_2$ cathode, a MCMB 2528 graphite (Bellcore) anode, and a $LiPF_6$ in EC : DMC electrolyte.
[b] "fixed" in the sense of "not estimated", and thus directly measured (like T) or chosen a priori (like M_r and α).
[c] in the absence of more detailed information about reaction mechanisms, the anodic and cathodic transfer coefficients are commonly considered equal to 0.5 [34].

Table 3.4: Parameters and constants for the Electrode Averaged Model.

1. The cell is set up in a controlled environment and in an initial known state (i.e. fully charged/fully discharged). A reference discharging/charging scheme is applied to generate the identification data.

   Simulation A Li-ion cell with a $LiCoO_2$ cathode, a MCMB 2528 graphite (Bellcore) anode, and a $LiPF_6$ in EC : DMC electrolyte is simulated through the "Dualfoil 5.1" program by John Newman [20] with the configuration reported in Appendix A. The cell is set in what will be considered a fully charged state, corresponding to a relaxed open-circuit voltage of $\simeq 4.2\,\mathrm{V}$, and is discharged with a current density input of $10\,\mathrm{A/m^2}$ for $2\,\mathrm{h}$ (Figure 3.3). In this new state, the cell will be considered fully discharged, with a relaxed open-circuit voltage of $\simeq 3.7\,\mathrm{V}$. The data series generated by the program is resampled at a constant sample time of $1\,\mathrm{s}$ and superimposed with a $0\,\mathrm{V}$ mean and $0.01\,\mathrm{V}$ standard deviation white gaussian noise, resulting in a more realistic data set for the following parameter estimation step.

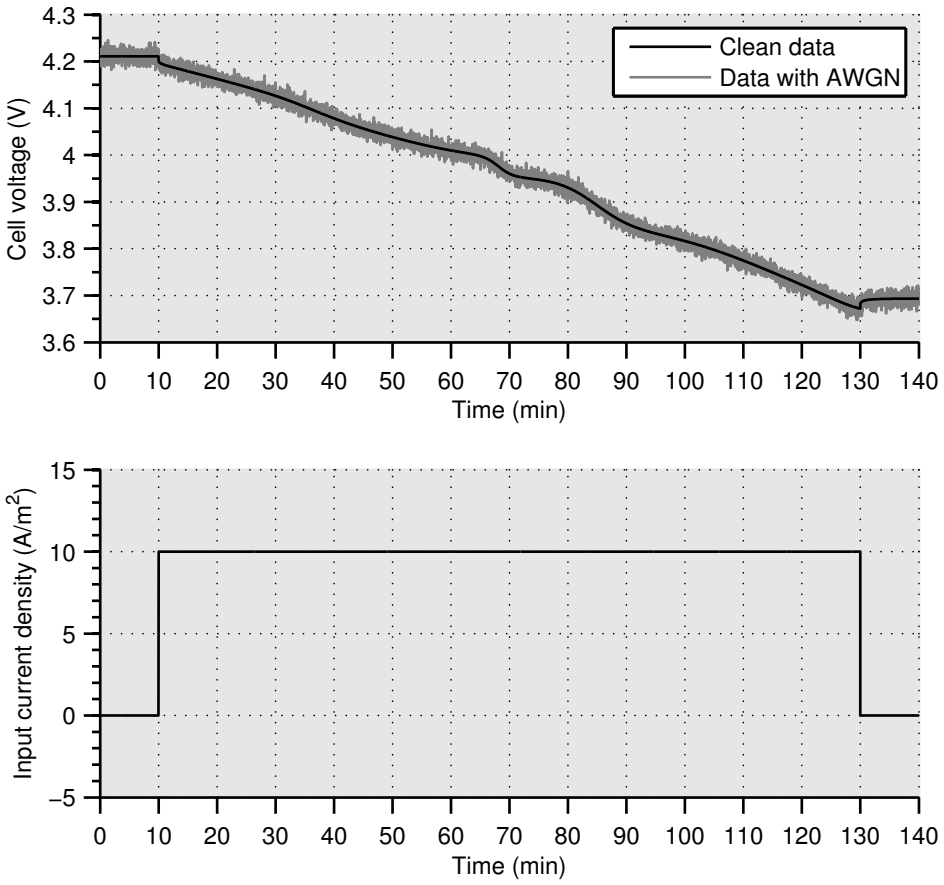

Figure 3.3: Simulated discharge profile data.

From now on, this output data will be referred to as the measured data, having the role of actual measured data, even if it is simulated.

2. Depending on the application, only a smaller portion of the available data sets may be significant for the identification. By limiting the data to just what is needed, speed and accuracy of the parameter estimation can be improved. For a HEV, the battery state-of-charge is commonly enforced to remain between 30 % and 70 %.

   Simulation With regards to the full discharge curve at constant current of the previous step, charge (which is the integral of current) is drained linearly with time, thus only the 30 % to 70 % window of the data can be considered, neglecting the remaining parts of the discharge curve (Figure 3.4).

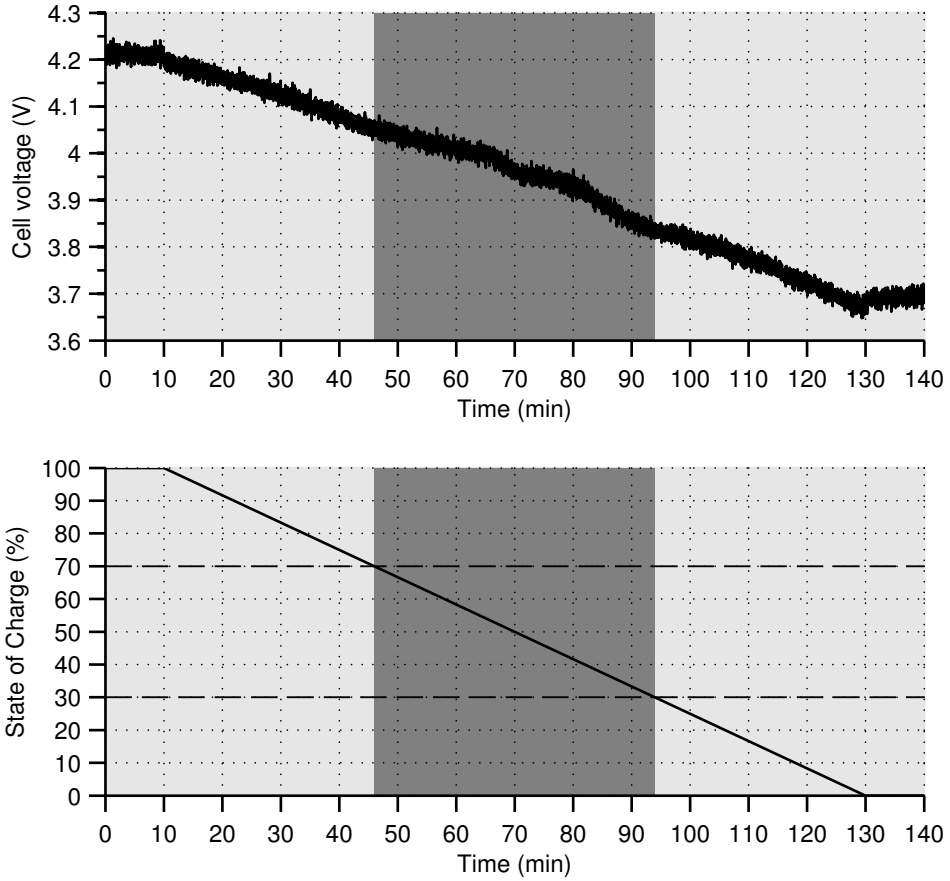

Figure 3.4: 30 % to 70 % data window selection.

3. After choosing M_r, assigning initial values to the other parameters and to the states, and configuring the model simulation and estimation options, the Levenberg-Marquardt algorithm is run on the selected data. This step is repeated until a satisfactory fit has been reached, trying higher values for M_r, choosing different values for the initial parameters and states, and possibly increasing the number of iterations and accuracy tolerances of the algorithm.

   Simulation In order to choose M_r, several identifications are run for a set of M_r choices. The quality of the resulting fits is quantified with the figure returned by the `compare` function of the Matlab System Identification Toolbox. Designating the column vector of N "measured" outputs with $\mathbf{y}$, its mean with $\bar{y}$, and the column vector of simulated outputs with $\hat{\mathbf{y}}$, this fit indicator is given by:

$$\text{fit} \triangleq 100 \left(1 - \frac{||\hat{\mathbf{y}} - \mathbf{y}||}{||\mathbf{y} - [\underbrace{1 \; 1 \; \cdots \; 1}_{N}]' \bar{y}||} \right) \tag{3.49}$$

   and represents the percentage of the output variation that is explained by the model. As shown in Figure 3.5, increasing M_r leads to a distinguishable improvement only below a value of 4, above which the fit levels off. In fact, the potential benefit due to a finer radial discretization is balanced with the increased effort in correctly identifying the states, the number of algorithm iterations being the same for each identification.

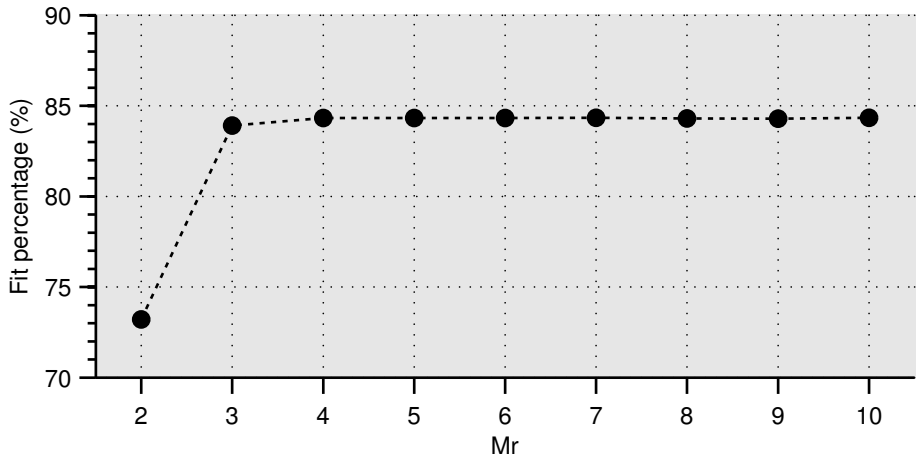

Figure 3.5: Model fit versus M_r.

In particular, using $M_r = 4$, the nominal values of Table 3.4, and a set of initial state values that equalize the initial cell voltage of measured and simulated curves, the identified model has a fit of $\simeq 84.3\,\%$, which results to be $\simeq 14.4\,\%$ higher than the fit before the identification. The simulated output of the model before and after the identification is shown with the measured data in Figure 3.6.

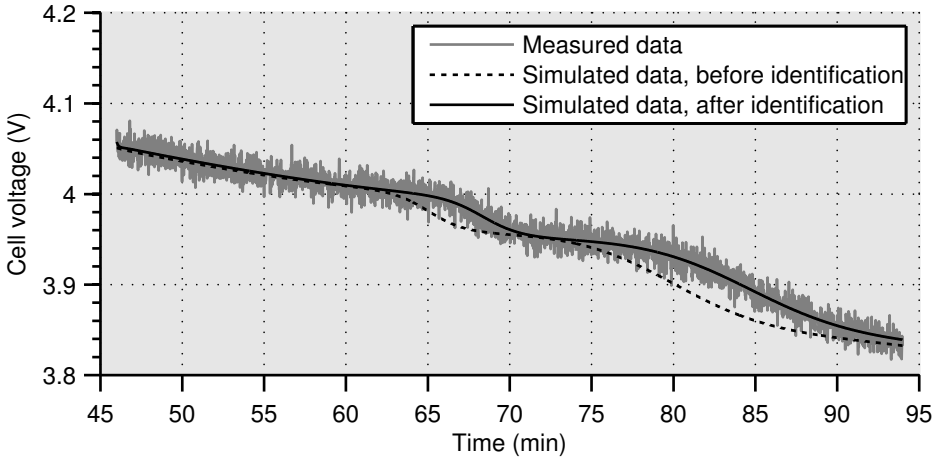

Figure 3.6: Output measured and simulated data.

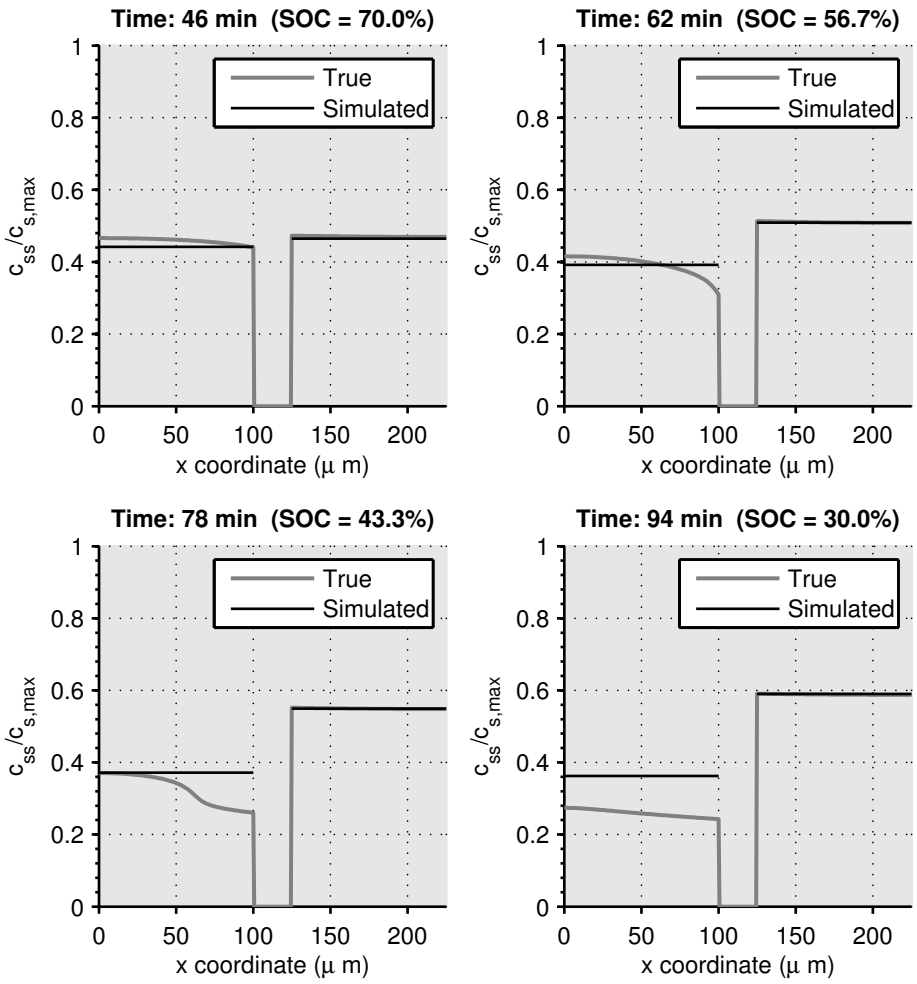

Figure 3.7: Concentration ratio at the surface of the solid particles.

Since the measured data is actually generated by simulation of the full rigorous model, it is possible to have access to the true states, and to compare those states with the ones of the EAM. Figure 3.7 shows the values of $c_{ss}/c_{s,max}$, i.e. the ratio between the concentration at the surface of the solid particles and the maximum concentration allowed, which will be designated as the utilization ratio. These are distributed along the profile of the cell, while for the EAM only the averages values for each electrode are available. The identified EAM captures very accurately the dynamics of the cathode utilization ratio, while it poorly tracks the fluctuation of the anode one. Recalling Eq. 3.47, it can be seen that both $\bar{c}_{ssn}$ and $\bar{c}_{ssp}$ contribute to the output through the open voltage potentials, but the contribution of the two is actually very different. As Figure 3.8 reports, the anode OCP values are much lower than the cathode ones, and also exhibit a very flat profile for most of c_{ss} values. These facts make the anode state weakly observable from the output, thus biasing the identification process and favouring the positive electrode tracking. To deal with this observability issue, in the next Chapter the EAM presented so far, which will be referred to as the Double Electrode Averaged Model (DEAM), will be replaced by a single electrode version of the same model. In this new formulation, the anode concentration dynamics is algebraically related to the cathode one, thus limiting the tracking of the solid concentration levels just to the latter electrode.

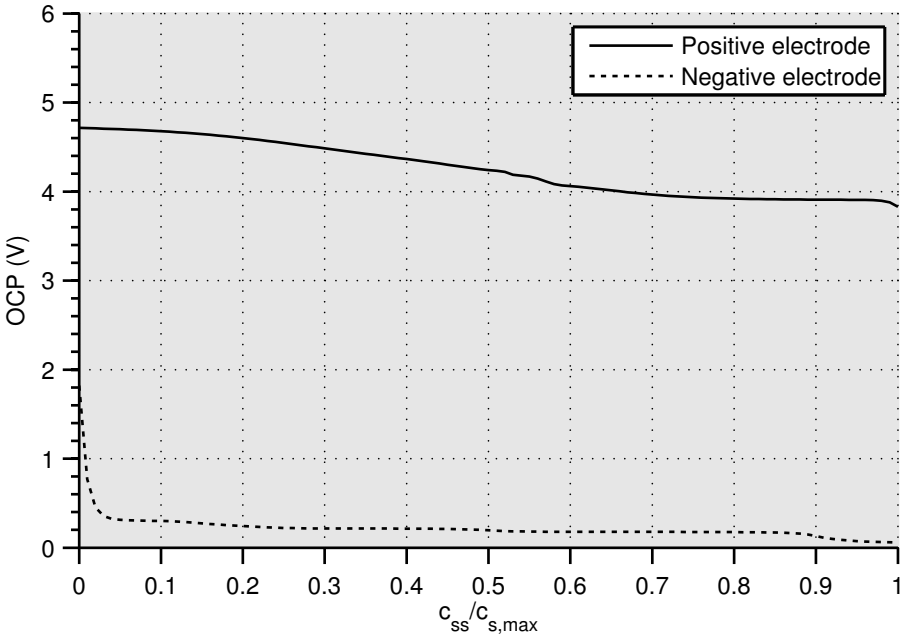

Figure 3.8: Open Circuit Potential (OCP) functions for the electrodes of the considered lithium-ion cell.

Chapter 4

State-Of-Charge Estimation

Contents

4.1 Introduction

The State-Of-Charge (SOC) of a battery, as stated in the Handbook of Batteries by Linden and Reddy [16], is a measure of the available capacity in the battery, and is usually expressed as a percentage of rated capacity. Here, "capacity" may equivalently refer to the coulometric capacity (A h), or to the energy (W h) available for a given discharge rate. Sauer et al. [29] define SOC more specifically as:

$$S(t) = \frac{Q_b - \int_{t_0}^{t} i_{ext}(t')\,dt'}{Q_b} \tag{4.1}$$

where $S(t)$ is the State-Of-Charge at the instant t, Q_b is the available discharging capacity of the battery at the instant t_0, when it is considered fully charged, and i_{ext} is the current applied by the battery to its load (positive when discharging, negative otherwise).

A crucial issue in the above definitions is the ability to determine when a battery can be considered fully charged or discharged, and thus how its nominal capacity can be evaluated. Usually, coulometric measurements are done by charging or discharging the cell between predefined voltage limits at a prescribed current rate. Efforts have also been made to standardize these and other potential ambiguities arising in the field of storage cells and batteries testing. For example, according to DIN 43539, the full SOC of a battery is reached when the battery current is not changing during 2 h at a constant charge voltage and constant temperature.

This kind of tests is run by battery manufacturers to provide the specifications of their products, which are precious information for the users of those batteries. Nonetheless, the resulting nominal values strongly depend on the test conditions and are subject to change over time, making the SOC measurements, which involve those nominal values, not so straightforward. This has led to several solutions, addressing a variety of technical goals and framework of applications.

From an electrochemical point of view, SOC is defined as a nondimensional quantity calculated in terms of lithium concentration, which is related to the charge contained in each electrode of a cell available for energy conversion [6]. In this context, it is convenient to introduce the notion of utilization of an electrode. In particular, the utilization of a given electrode at a certain point x and radius r, which will be denoted with $\theta(x, r)$, is defined as:

$$\theta(x, r) \triangleq c_s(x, r)/c_{s,max} \tag{4.2}$$

where $c_s(x, r)$ and $c_{s,max}$ are taken from the modeling framework developed in Chapter 3, and represent the local lithium ions concentration and the corresponding maximum possible concentration, respectively. For simplicity, $c_{s,max}$ is supposed to be constant along x and r in the electrode. The average utilization of the entire electrode is called the bulk state of charge of the electrode, while the average utilization at the surface of the solid particles is referred to as surface SOC. The bulk SOC is related to the charge exchanged between the battery and the load, and can be tracked through current integration, assuming precise current measurements and correct initial conditions are available. It is usually used for estimating the energy stored in a battery. The surface SOC is directly referable to the instantaneous available power and, unlike the bulk SOC, requires an adequate electrochemical model to be estimated. The knowledge of these two quantities allows to estimate and predict energy, power and feasible load currents, as well as to look for optimal battery usage profiles.

In the following sections, the concept of bulk and surface SOC will be introduced in the Electrode Averaged Model framework presented in the previous chapter. Then, a Kalman Filter approach will be developed to address the SOC estimation problem in a reliable and accurate way.

4.2 Methods for SOC estimation

Coulomb counting, or current integration, has been the most commonly used technique for SOC determination, given the direct relation between the time integral of the cell/battery current measurements and SOC (see Eq. 4.1). However, the reliance on integration involves the cumulation of any errors in terminal measurements due to noise, resolution, and rounding, and leads to possibly large SOC reading errors. Therefore, a reset or recalibration action is required at regular intervals and at known SOC states, which could be unpractical during normal HEV operation, where potential reference conditions, e.g. corresponding to full or zero SOC,

are rarely achieved. Additional complications for the traditional integration-based techniques include the variation of cell capacity with discharge rate, temperature, and Coulombic efficiency losses, all phenomena which are not negligible for the long-term and highly dynamical battery usage in HEVs.

Several other methods have been considered for estimating the SOC of a cell. According to Piller et al. [24], SOC can be also calculated from:

electrochemical properties i.e. unobservable processes following some physical properties of the cell, like lithium ions concentrations, current density, potential, internal resistance and electrolyte density, which are estimated online with a model calibrated against experimental data;

open cell voltage (OCV) at equilibrium, for those chemistries with a well-known OCV-SOC relationship;

impedance characteristics exploiting the fact that SOC affects the frequency response, even though the latter is affected also by other factors;

optical properties using sensors inside the battery to detect changes in optical absorption, which correspond to changes in composition occurring with charge/discharge in certain batteries;

Foucault's eddy currents which a cell manifests when exposed to an appropriate inductive field, enabling contact-less impedance measurements;

equivalent circuit states or parameters estimated through circuit-based models, simpler than the electrochemical ones thus providing a faster real-time execution but a less accurate SOC reading in highly dynamical contexts;

fuzzy-logic algorithms which use experimental training data to infer a feasible cell model, avoiding the need for an a priori knowledge of the system.

Up till now, the most reliable and complete approach remains the one based on the estimation of electrochemical quantities that can be related to SOC. The preferred mathematical tool to estimate those quantities minimizing the effect of noise disturbance and modeling inaccuracy is the Kalman Filter, in any of its variants.

The use of equivalent circuit models in the design of a BMS has become popular due to their good performance with portable electronics, where the approximation of the battery model with an equivalent circuit is adequate. Then, this modeling approach has been extended to Li-ion batteries in the automotive field, which is an application area that can expose it to serious pitfalls. As already discussed, the high accuracy required by automotive applications cannot be achieved through equivalent circuit models, which are based on the response of the battery to a dynamic range which does not fully capture the operational regime of a HEV. The latter involves both current charge/discharge pulses with small changes in SOC (microcycling), and low current pulses with large SOC changes (deep cycling). A linear system is simply not enough to represent all of these dynamics.

The equivalent circuit model can be extended by letting the circuit parameters depend on SOC and temperature, or even the applied current. However, this leads to a large number of parameters and functions to fit, the meaning of which has possibly no physical intuition. For the same complexity, it is then more convenient to exploit an electrochemical model, where parameters value can be understood and tracked more easily.

Fuzzy-logic and neural networks are two interesting tools for modeling Li-ion batteries, since they do not require any physical understanding of the system being modeled, but just a series of input-output data. However, the resulting model is highly dependent on the characteristics of the training data, and may not represent in a satisfactory way the model behaviour for the entire operational regime of interest. Like for the equivalent circuit models, it is possible to train several models for matching as many different operational regions, at the cost of increasing training and real-time execution complexity.

OCV methods are hardly practical in a HEV context, where the battery is almost always far from equilibrium when in use. Furthermore, some cell chemistries exhibit only a very small change in voltage over most of the charge/discharge cycle, making it unpractical to exploit any voltage-SOC relationship.

Other methods mentioned above are not discussed here, since they play a secondary or controversial role in the literature about the subject under consideration. From now on, emphasis will be given exclusively to the Kalman Filter approach, and in particular to one of its nonlinear variant called the Unscented Kalman Filter.

4.3 The Electrode Averaged Model revisited

Since the availability of charge in a cell is related to the availability of lithium ions in the solid particles, the cell SOC can be thought as a function of the solid concentration at the electrodes. This quantity is accounted in the EAM in the state variables, thus motivating the design of an estimator coupled with that model to address the on-line SOC estimation problem.

Before exploiting the Kalman Filter framework for this purpose, it is necessary to discuss the observability of the dynamical system under consideration. Even though this model can describe the solid concentration dynamics at the radius of a representative spherical solid particle in both electrodes, the output depends on $U_p(\bar{c}_{ssp}) - U_n(\bar{c}_{ssn})$ (see Eq. 3.47), which makes it hard to determine the contribution of each electrode from the output itself. This leads to a model that is weakly observable (in the linear sense) from the output cell voltage when considering both positive and negative electrodes.

Observability can be improved by keeping track of just the solid concentration of the positive electrode. The negative electrode surface concentration $\bar{c}_{ssn}$, which is needed in the output equation, can be calculated through an appropriate algebraic relation involving the SOC. In order to determine this relation, after defining the

average bulk positive solid concentration $\bar{c}_{sbp}$ as:

$$\bar{c}_{sbp} \triangleq \frac{\bar{c}_{sp_1} + \cdots + \bar{c}_{sp_{(M_r-1)}}}{M_r - 1} \tag{4.3}$$

it is convenient to introduce the average bulk positive utilization ratio θ_p:

$$\theta_p \triangleq \frac{\bar{c}_{sbp}}{c_{s,max,p}} \qquad \theta_{p100\,\%} \leq \theta_p \leq \theta_{p0\,\%} \tag{4.4}$$

where $\theta_{p0\,\%}$ and $\theta_{p100\,\%}$ correspond to the average concentration in a full discharged or charged cell, respectively. The two reference values for θ_p are related to the positive electrode capacity Q_p (C) by the equation:

$$|\theta_{p100\,\%} - \theta_{p0\,\%}| = \frac{Q_p}{\Sigma_p \delta_p F \varepsilon_p c_{s,max,p}} \tag{4.5}$$

where Σ_p is the trasversal area (m^2) of the electrode, δ_p is its thickness (m), and ε_p is its porosity. Then, the bulk SOC of the electrode, which will be named SOC_b, can be assumed to be linearly varying with θ_p [32]:

$$SOC_b = \frac{\theta_p - \theta_{p0\,\%}}{\theta_{p100\,\%} - \theta_{p0\,\%}}. \tag{4.6}$$

Statements similar to Eqs. 4.3, 4.4, 4.5 and 4.6 are valid also for the average negative electrode solid concentration, with the difference that :

$$\theta_n \triangleq \frac{\bar{c}_{sbn}}{c_{s,max,p}} \qquad \theta_{n100\,\%} \leq \theta_p \leq \theta_{p0\,\%}. \tag{4.7}$$

In good approximation, the SOC associated with θ_n has the same instantaneous value of the one derived from the positive concentration, in which case the following holds:

$$\theta_n = \theta_{n0\,\%} + SOC_b(\theta_{n100\,\%} - \theta_{n0\,\%}) \qquad \theta_{n100\,\%} \geq \theta_n \geq \theta_{n0\,\%}. \tag{4.8}$$

In the above equations, it is assumed that $\theta_{p0\,\%} > \theta_{p100\,\%}$ and $\theta_{n0\,\%} < \theta_{n100\,\%}$. These inequalities agree with what has been previously expressed in words: during the discharge of a fully charged cell, lithium ions are withdrawn from the negative electrode (θ_n decreases from a maximum to a minimum) and injected in the positive one (θ_p increases from a minimum to a maximum). Once the value of θ_n is available, it is possible to calculate the average anode solid bulk concentration $\bar{c}_{sbn}$ with:

$$\bar{c}_{sbn} = \theta_n c_{s,max,n} \tag{4.9}$$

and finally obtain the surface concentration by using Eq. 3.37:

$$\bar{c}_{ssn} = \bar{c}_{sbn} - \frac{\Delta r_n}{D_{sn} a_n F} \bar{j}_n^{Li} \tag{4.10}$$

which allows to calculate the desired output.

4.4 The Unscented Kalman Filter

Given a linear stochastic dynamical system satisfying proper assumptions, the Kalman filter is the optimal estimatator of the system state when the noise is Gaussian, and provides the optimal linear estimate when the noise is not Gaussian [30]. Due to its well-developed theoretical framework, and to the efficiency of its computational implementation, the filter has gained wide acceptance for filtering and estimation problems in almost all the engineering fields.

The most limiting assumption for Kalman Filter applicability is the linearity of the underlying model. Unfortunately, many real systems exhibit a behaviour that can be hardly approximated in a satisfactory way by simple linear models. This has motivated the reasearch for extending the basic KF, leading to the development of several nonlinear estimation approaches.

In the past few decades, the so-called Extended Kalman Filter (EKF) has been without doubt the most widely applied nonlinear state estimation technique. This method involves finding a linear system whose state represents the deviation from a nominal trajectory of the nonlinear system, and whose dynamics derives from a linearization of the original equations.

More recently, "higher-order"[1] approaches to nonlinear Kalman filtering have appeared, which provide ways to reduce the linearization errors that are inherent in the EKF. These filters perform generally better than the EKF, at the price of higher complexity and computational expense.

One significant example of these filters is the Unscented Kalman Filter (UKF), proposed in 1996 by Julier and Uhlmann, and further developed by Wan and van der Merwe a few years later [36]. A simple illustration of this approach is depicted in Figure 4.1. for a 2-dimensional system. In the leftmost plots, the true mean and covariance are propagated using Monte-Carlo sampling. In the center plots it is shown how the propagation occurs through a linearization approach, analogous to the one used in the EKF. Finally, the rightmost plots show the performance of the UKF sampling technique. The latter is a straightforward application of the Unscented Transformation, which will be described later on. The idea is to propagate the original mean and covariance of the state distribution through a minimal set of carefully chosen sample points on which the non-approximated nonlinearity is applied.

Two main reasons make the UKF a more preferable option with respect to the EKF when dealing with high precision nonlinear estimation requirements. First, the linearization approach exploited by the EKF can only guarentee a first order accuracy (in the Taylor series expansion), while the UKF results in approximations that are accurate to at least the second-order for all nonlinearities. If the inputs are Gaussian, then approximations are accurate even to the third order. Second, while

[1] involving more than a direct linearization of the nonlinear system

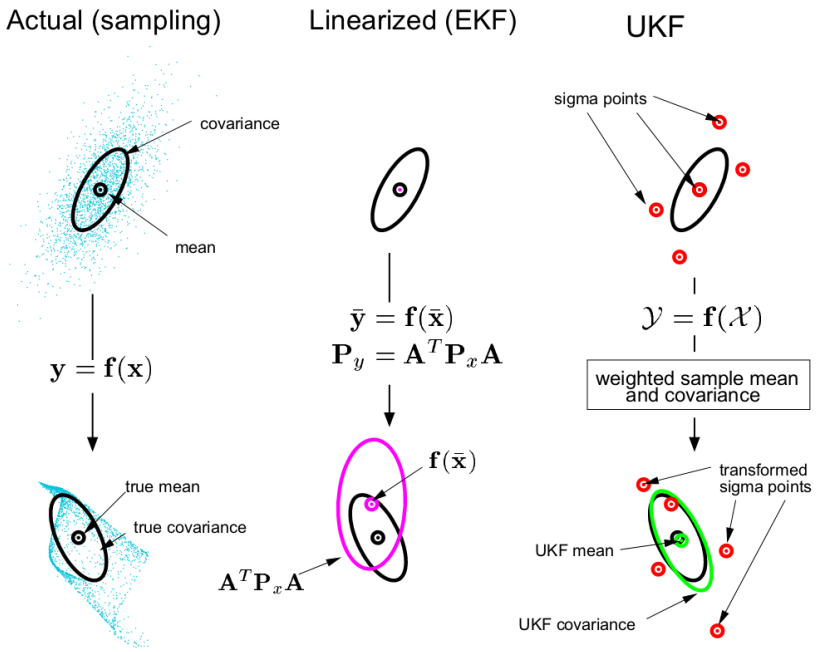

Figure 4.1: How mean and covariance of an example random variable nonlinear transformation are propagated through EKF and UKF approaches [37].

the EKF requires the Jacobian matrix of the model equations, which is not always available or easy to calculate, the UKF does not require this information, since the nonlinear equations are used without approximation.

4.4.1 The Unscented Transformation

The difficulty with nonlinear estimation problems is due to the necessity of transforming probability density functions through a general nonlinear function. The Extended Kalman Filter works on the principle that a linearized transformation of means and covariances is approximately equal to the true nonlinear transformation. As previously observed, this may lead to unsatisfactory results.

The unscented transformation (UT) is another method for calculating the statistics of a random variable which undergoes a nonlinear transformation. Let consider a random vector $\mathbf{x}$ of dimension L, with mean $\bar{\mathbf{x}} \in \mathbb{R}^L$ and covariance $\mathbf{P}_\mathbf{x} \in \mathbb{R}^{L\times L}$. Let also consider a random vector $\mathbf{y}$=$\mathbf{f}(\mathbf{x})$ with mean $\bar{\mathbf{y}}$ and covariance $\mathbf{P}_\mathbf{y}$, where $\mathbf{f}(\cdot)$ is a generic nonlinear function. To calculate the statistics of $\mathbf{y}$, first the matrix $\mathcal{X}$ is formed by juxtaposition of $2L+1$ column vectors $\mathcal{X}_i, i \in 0, \ldots, 2L$, called *sigma*

vectors, defined according to the following:

$$\begin{aligned}
\mathcal{X}_0 &= \bar{\mathbf{x}} \\
\mathcal{X}_i &= \bar{\mathbf{x}} + \left(\sqrt{(L+\lambda)\mathbf{P}_{\mathbf{x}}}\right)_i && i = 1, \ldots, L \\
\mathcal{X}_i &= \bar{\mathbf{x}} - \left(\sqrt{(L+\lambda)\mathbf{P}_{\mathbf{x}}}\right)_{i-L} && i = L+1, \ldots, 2L \\
\mathcal{X} &= [\mathcal{X}_0 \;\; \mathcal{X}_1 \;\; \cdots \;\; \mathcal{X}_{2L}]
\end{aligned} \tag{4.11}$$

where λ is a scaling parameter and $(\sqrt{(\cdot)})_i$ denotes the i-th column of the matrix square root (e.g. lower-triangular Cholesky factorization) of the argument. More specifically, λ is assumed equal to $\alpha^2(L+\kappa) - L$, where α here[2] determines the spread of the sigma points around $\mathbf{x}$, and is usually set to a small positive value (e.g. $10^{-4} \leq \alpha \leq 1$), while κ is a secondary scaling parameter usually set to $3 - L$.

The sigma vectors of Eq. 4.11 are transformed through $\mathbf{f}(\cdot)$ to obtain as many new vectors $\mathcal{Y}_i$:

$$\mathcal{Y}_i = \mathbf{f}\left(\mathcal{X}_i\right) \qquad i = 0, \ldots, 2L. \tag{4.12}$$

Finally, a weighted sample mean and covariance of the just calculated posterior sigma points is used to approximate the mean and covariance of $\mathbf{y}$, respectively:

$$\bar{\mathbf{y}} \simeq \sum_{i=0}^{2L} W_i^{(m)} \mathcal{Y}_i \tag{4.13}$$

$$\mathbf{P}_{\mathbf{y}} \simeq \sum_{i=0}^{2L} W_i^{(c)} \left(\mathcal{Y}_i - \bar{\mathbf{y}}\right)\left(\mathcal{Y}_i - \bar{\mathbf{y}}\right)' \tag{4.14}$$

with weighting coefficients W_i given by:

$$W_0^{(m)} = \frac{\lambda}{L+\lambda} \qquad W_i^{(m)} = \frac{1}{2(L+\lambda)} \qquad i = 1, \ldots, 2L \tag{4.15}$$

$$W_0^{(c)} = \frac{\lambda}{L+\lambda} + 1 - \alpha^2 + \beta \qquad W_i^{(c)} = \frac{1}{2(L+\lambda)} \qquad i = 1, \ldots, 2L \tag{4.16}$$

where β is used to incorporate prior knowledge of the distribution of $\mathbf{x}$ (for Gaussian distributions, $\beta = 2$ is optimal).

The whole procedure for the UT is summarized in the block diagram of Figure 4.2. This method differs substantially from general Monte Carlo sampling methods, which require orders of magnitude more sample points for propagating an accurate (possibly non-Gaussian) distribution of the state. Recalling the example of Figure 4.1, only 5 samples are required for the UKF by means of the UT to obtain fairly good estimates. As mentioned before, approximations introduced with Eqs. 4.13 and 4.14 are accurate to at least the second order, with the accuracy

[2] From now on, the constants α and κ are used with the meaning given in the present context, and will not refer to the electrochemical parameters denoted with the same symbols in the previous chapter.

of third- and higher-order moments being determined by the choice of the tuning parameters α and β.

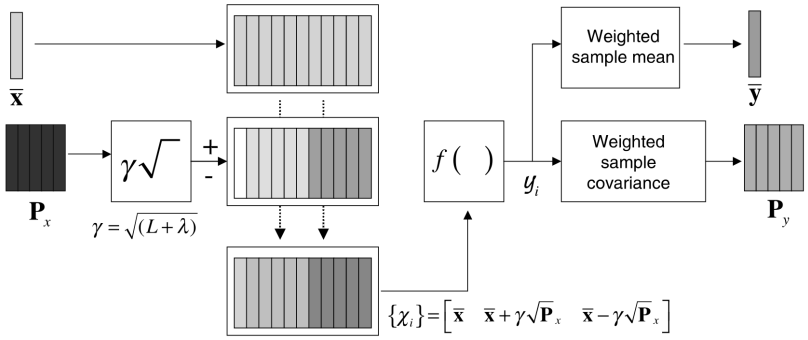

Figure 4.2: UT block diagram [36].

4.4.2 The standard UKF algorithm

A straightforward extension of the UT leads to the formulation of the UKF recursive estimation algorithm. Its basic framework involves a discrete-time nonlinear dynamical system of the form:

$$\mathbf{x}_{k+1} = \mathbf{f}(\mathbf{x}_k, \mathbf{u}_k) + \mathbf{v}_k \tag{4.17}$$

$$\mathbf{y}_k = \mathbf{h}(\mathbf{x}_k, \mathbf{u}_k) + \mathbf{n}_k \tag{4.18}$$

where $\mathbf{u}_k$ is the deterministic known input at instant k, while $\mathbf{x}_k$, $\mathbf{y}_k$, $\mathbf{v}_k$ and $\mathbf{n}_k$ are the random variables sampled at instant k from the corresponding discrete-time second-order stochastic processes $\mathbf{x}$, $\mathbf{y}$, $\mathbf{v}$ and $\mathbf{n}$, with the following meaning:

$\mathbf{x}$ is the unobserved state of the system (of dimension L),

$\mathbf{y}$ is the observed measurement (of dimension M),

$\mathbf{v}$ is the process noise (of dimension L), representing the model inaccuracies,

$\mathbf{n}$ is the observation noise (of dimension M), representing the measurement inaccuracies.

The process and observation noise are supposed to be stationary and have zero mean, with covariance matrices $\mathbf{R}^{\mathbf{v}} \in \mathbb{R}^{L\times L}$ and $\mathbf{R}^{\mathbf{n}} \in \mathbb{R}^{M\times M}$ respectively. Furthermore, it is assumed that the noise processes are purely additive with respect to the undisturbed equations, as it will also be the case in the Li-ion cell simulations later on. Then, the steps forming the UKF algorithm for calculating the estimates of the mean and covariance of $\mathbf{x}$ at time k, i.e. $\hat{\mathbf{x}}_k$ and $\mathbf{P}_{\mathbf{x}}$, are outlined below.

- For $k = 0$:
  Initialize the algorithm with:

$$\begin{aligned}\hat{\mathbf{x}}_0 &= \mathbb{E}\left[\mathbf{x}_0\right] \\ \mathbf{P}_0 &= \mathbb{E}\left[\left(\mathbf{x}_0 - \hat{\mathbf{x}}_0\right)\left(\mathbf{x} - \hat{\mathbf{x}}_0\right)'\right]\end{aligned} \tag{4.19}$$

- For $k = 1, \ldots, +\infty$:

  1. Calculate the sigma points:

$$\begin{aligned}\mathcal{X}_{k-1}^{0} &= \hat{\mathbf{x}}_{k-1} \\ \mathcal{X}_{k-1}^{i} &= \hat{\mathbf{x}}_{k-1} + \left(\sqrt{(L+\lambda)\mathbf{P}_{k-1}}\right)_i \qquad i = 1, \ldots, L \\ \mathcal{X}_{k-1}^{i} &= \hat{\mathbf{x}}_{k-1} - \left(\sqrt{(L+\lambda)\mathbf{P}_{k-1}}\right)_{i-L} \qquad i = L+1, \ldots, 2L\end{aligned} \tag{4.20}$$

  2. Update the prior estimate of $\mathbf{x}_k$ mean and covariance:

$$\begin{aligned}\mathcal{X}_{k|k-1}^{\star,i} &= \mathbf{f}\left(\mathcal{X}_{k-1}^{i}, \mathbf{u}_{k-1}\right) \qquad i = 0, \ldots, 2L \\ \hat{\mathbf{x}}_k^- &= \sum_{i=0}^{2L} W_i^{(m)} \mathcal{X}_{k|k-1}^{\star,i} \\ \mathbf{P}_k^- &= \sum_{i=0}^{2L} W_i^{(c)} \left(\mathcal{X}_{k|k-1}^{\star,i} - \hat{\mathbf{x}}_k^-\right)\left(\mathcal{X}_{k|k-1}^{\star,i} - \hat{\mathbf{x}}_k^-\right)' + \mathbf{R}^{\mathbf{v}}\end{aligned} \tag{4.21}$$

     where the weighting coefficients $W_i^{(m)}$ and $W_i^{(c)}$ are those defined in Eqs. 4.15 and 4.16.

  3. Redraw a new set of sigma points to incorporate the effect of process noise:

$$\begin{aligned}\mathcal{X}_{k|k-1}^{0} &= \hat{\mathbf{x}}_k \\ \mathcal{X}_{k|k-1}^{i} &= \hat{\mathbf{x}}_k + \left(\sqrt{(L+\lambda)\mathbf{P}_k^-}\right)_i \qquad i = 1, \ldots, L \\ \mathcal{X}_{k|k-1}^{i} &= \hat{\mathbf{x}}_k - \left(\sqrt{(L+\lambda)\mathbf{P}_k^-}\right)_{i-L} \qquad i = L+1, \ldots, 2L\end{aligned} \tag{4.22}$$

  4. Update the prior estimate of $\mathbf{y}_k$ mean, covariance and covariance with

$\mathbf{x}_k$:

$$\begin{aligned}
\mathcal{Y}^i_{k|k-1} &= \mathbf{h}\left(\mathcal{X}^i_{k|k-1}, \mathbf{u}_k\right) && i = 0, \ldots, 2L \\
\hat{\mathbf{y}}^-_k &= \sum_{i=0}^{2L} W_i^{(m)} \mathcal{Y}^i_{k|k-1} \\
\mathbf{P}_{\mathbf{y}_k} &= \sum_{i=0}^{2L} W_i^{(c)} \left(\mathcal{Y}^i_{k|k-1} - \hat{\mathbf{y}}^-_k\right)\left(\mathcal{Y}^i_{k|k-1} - \hat{\mathbf{y}}^-_k\right)' + \mathbf{R}^{\mathbf{n}} \\
\mathbf{P}_{\mathbf{x}_k\mathbf{y}_k} &= \sum_{i=0}^{2L} W_i^{(c)} \left(\mathcal{X}^i_{k|k-1} - \hat{\mathbf{x}}^-_k\right)\left(\mathcal{Y}^i_{k|k-1} - \hat{\mathbf{y}}^-_k\right)' && (4.23)
\end{aligned}$$

5. Update the filter gain and use it, along with the new measurement reading $\mathbf{y}_k$, to calculate the posterior estimate of $\mathbf{x}_k$ mean and covariance:

$$\begin{aligned}
\mathcal{K}_k &= \mathbf{P}_{\mathbf{x}_k\mathbf{y}_k}\mathbf{P}^{-1}_{\mathbf{y}_k} \\
\hat{\mathbf{x}}_k &= \hat{\mathbf{x}}^-_k + \mathcal{K}_k\left(\mathbf{y}_k - \hat{\mathbf{y}}^-_k\right) \\
\mathbf{P}_k &= \mathbf{P}^-_k - \mathcal{K}_k\mathbf{P}_{\mathbf{y}_k}\mathcal{K}'_k && (4.24)
\end{aligned}$$

The complexity of the algorithm is of order L^3, which is the same as the EKF. If the process and measurement noise cannot be considered additive, then the state has to be augmented to include also $\mathbf{v}$ and $\mathbf{n}$, increasing the state dimension and thus the computational complexity.

4.4.3 The Square Root implementation

The standard UKF algorithm, described in the previous section, leaves space to a number of variations for improving its numerical performance. The most computationally expensive operation in the UKF is calculating the matrix square root $\mathbf{S}_k$ of $\mathbf{P}_k = \mathbf{S}_k\mathbf{S}'_k$ to draw a new set of sigma points at each time update. If this operation is done efficiently using a Cholesky factorization, the algorithm exhibits a complexity of $\mathcal{O}(1/6L^3)$. A different implementation of the algorithm, called the Square-Root Unscented Kalman Filter (SR-UKF) propagates the Cholesky factor $\mathbf{S}_k$ instead of $\mathbf{P}_k$, avoiding the refactorization step. For state estimation, the algorithm will in general still be $\mathcal{O}(L^3)$, but with improved numerical properties (e.g., guaranteed positive-semidefiniteness of the state covariances).

Behind the superior numerical properties of the SR-UKF there are three powerful linear-algebra techniques, which are briefly reviewed below [36].

QR decomposition of a matrix $\mathbf{A} \in \mathbb{R}^{L\times N}$. For $N \geq L$, it is given by $\mathbf{A}' = \mathbf{QR}$, where $\mathbf{Q} \in \mathbb{R}^{N\times N}$ is orthogonal, and $\mathbf{R} \in \mathbb{R}^{N\times L}$ is such that $\mathbf{R} = [\tilde{\mathbf{R}}' \quad \mathbf{0}']'$, where $\tilde{\mathbf{R}} \in \mathbb{R}^{L\times L}$ is upper triangular and equal to the transpose of the Cholesky factor of $\mathbf{P} = \mathbf{A}\mathbf{A}'$, while $\mathbf{0}$ is a $(N-L)\times L$ zero matrix. The notation $\mathrm{qr}\{\cdot\}$ will be used to denote the $\tilde{\mathbf{R}}$ matrix returned by the

QR composition of the argument inside curly brakets. The computational complexity per time update is $\mathcal{O}(NL^2)$.

Cholesky factor updating of $\mathbf{P} = \mathbf{A}\mathbf{A}' \in \mathbb{R}^{L\times L}$. Given a column matrix $\mathbf{u} \in \mathbb{R}^{L\times 1}$, the Cholesky factor of the rank-1 update/downdate $\mathbf{P} \pm \sqrt{\nu}\mathbf{u}\mathbf{u}'$ can be calculated in terms of the original lower-triangular Cholesky factor $\mathbf{S}$ with a $\mathcal{O}(L^2)$ algorithm[3]. The Cholesky factor resulting from this procedure will be denoted by cholupdate$\{\mathbf{S}, \mathbf{u}, \pm\nu\}$. If $\mathbf{u}$ is a matrix with M columns, then the result is M consecutive updates of the Cholesky factor, one for each column of $\mathbf{u}$.

Efficient least squares for solving the equation $(\mathbf{A}\mathbf{A}')\mathbf{x} = \mathbf{A}'\mathbf{b}$. The latter problem can be formulated as an overdetermined least squares problem, which can be solved efficiently using a QR decomposition with pivoting[4].

All of these techniques are exploited in the SR-UKF procedure, whose steps are described below.

- For $k = 0$:
  Initialize the algorithm with:

$$\begin{aligned}\hat{\mathbf{x}}_0 &= \mathbb{E}\left[\mathbf{x}_0\right] \\ \mathbf{S}_0 &= \mathrm{chol}\left\{\mathbb{E}\left[(\mathbf{x}_0 - \hat{\mathbf{x}}_0)\,(\mathbf{x} - \hat{\mathbf{x}}_0)'\right]\right\}.\end{aligned} \tag{4.25}$$

  Unlike the original UKF, here only the Cholesky factor of $\mathbf{P}$ will be propagated and updated in the subsequent iterations.

- For $k = 1, \ldots, +\infty$:

  1. Calculate the sigma points using directly the Cholesky factor instead of the square root of $\mathbf{P}$:

$$\begin{aligned}\mathcal{X}_{k-1}^0 &= \hat{\mathbf{x}}_{k-1} \\ \mathcal{X}_{k-1}^i &= \hat{\mathbf{x}}_{k-1} + \sqrt{L+\lambda}\,(\mathbf{S}_k)_i \qquad\qquad i = 1, \ldots, L \\ \mathcal{X}_{k-1}^i &= \hat{\mathbf{x}}_{k-1} - \sqrt{L+\lambda}\,(\mathbf{S}_k)_{i-L} \qquad i = L+1, \ldots, 2L\end{aligned} \tag{4.26}$$

[3] Such as the one implemented in the `cholupdate` command in Matlab.
[4] Such as the operation performed by the `mrdivide` or "/" command in Matlab.

2. Update the prior estimate of $\mathbf{x}_k$ mean and of the Cholesky factor of $\mathbf{P}_k$:

$$\begin{aligned}
\mathcal{X}^{\star,i}_{k|k-1} &= \mathbf{f}\left(\mathcal{X}^{i}_{k-1}, \mathbf{u}_{k-1}\right) && i = 0, \dots, 2L \\
\hat{\mathbf{x}}^{-}_{k} &= \sum_{i=0}^{2L} W^{(m)}_{i} \mathcal{X}^{\star,i}_{k|k-1} \\
\tilde{\mathcal{X}}^{\star,1:2L}_{k|k-1} &= \begin{bmatrix} \left(\mathcal{X}^{\star,1}_{k|k-1} - \hat{\mathbf{x}}^{-}_{k}\right) & \cdots & \left(\mathcal{X}^{\star,2L}_{k|k-1} - \hat{\mathbf{x}}^{-}_{k}\right) \end{bmatrix} \\
\mathbf{S}^{-}_{k} &= \mathrm{qr}\left\{ \begin{bmatrix} \sqrt{W^{(c)}_{1}} \tilde{\mathcal{X}}^{\star,1:2L}_{k|k-1} & \sqrt{\mathbf{R}^{\mathbf{v}}} \end{bmatrix} \right\} && (4.27) \\
\mathbf{S}^{-}_{k} &= \mathrm{cholupdate}\left\{ \mathbf{S}^{-}_{k}, \mathcal{X}^{\star,0}_{k|k-1} - \hat{\mathbf{x}}^{-}_{k}, W^{(c)}_{0} \right\} && (4.28)
\end{aligned}$$

where $W^{(m)}_{i}$ and $W^{(c)}_{i}$ are the same weighting coefficients used for the standard UKF. The time update of the Cholesky factor $\mathbf{S}^{-}_{k}$ is calculated using the aforementioned QR decomposition, which is applied to the compound matrix containing the weighted propagated sigma points and the matrix square root of the additive process noise covariance. The subsequent Cholesky update (or downdate) in the latter equation is required to deal with the case of a possibly negative zeroth weight. These two steps replace the time-update of $\mathbf{P}^{-}_{k}$ in the UKF and have the same time complexity of $\mathcal{O}(L^3)$.

3. Redraw a new set of sigma points to incorporate the effect of process noise:

$$\begin{aligned}
\mathcal{X}^{0}_{k-1} &= \hat{\mathbf{x}}_{k-1} \\
\mathcal{X}^{i}_{k-1} &= \hat{\mathbf{x}}_{k-1} + \sqrt{L+\lambda}\left(\mathbf{S}^{-}_{k}\right)_{i} && i = 1, \dots, L \\
\mathcal{X}^{i}_{k-1} &= \hat{\mathbf{x}}_{k-1} - \sqrt{L+\lambda}\left(\mathbf{S}^{-}_{k}\right)_{i-L} && i = L+1, \dots, 2L \qquad (4.29)
\end{aligned}$$

4. Update the prior estimate of $\mathbf{y}_k$ mean, covariance Cholesky factor, and covariance with $\mathbf{x}_k$:

$$\begin{aligned}
\mathcal{Y}^{i}_{k|k-1} &= \mathbf{h}\left(\mathcal{X}^{i}_{k|k-1}, \mathbf{u}_{k}\right) && i = 0, \dots, 2L \\
\hat{\mathbf{y}}^{-}_{k} &= \sum_{i=0}^{2L} W^{(m)}_{i} \mathcal{Y}^{i}_{k|k-1} \\
\tilde{\mathcal{Y}}^{1:2L}_{k|k-1} &= \begin{bmatrix} \left(\mathcal{Y}^{1}_{k|k-1} - \hat{\mathbf{y}}^{-}_{k}\right) & \cdots & \left(\mathcal{Y}^{2L}_{k|k-1} - \hat{\mathbf{y}}^{-}_{k}\right) \end{bmatrix} \\
\mathbf{S}_{\mathbf{y}_k} &= \mathrm{qr}\left\{ \begin{bmatrix} \sqrt{W^{(c)}_{1}} \tilde{\mathcal{Y}}^{1:2L}_{k|k-1} & \sqrt{\mathbf{R}^{\mathbf{n}}} \end{bmatrix} \right\} && (4.30) \\
\mathbf{S}_{\mathbf{y}_k} &= \mathrm{cholupdate}\left\{ \mathbf{S}_{\mathbf{y}_k}, \mathcal{Y}^{0}_{k|k-1} - \hat{\mathbf{y}}^{-}_{k}, W^{(c)}_{0} \right\} \\
\mathbf{P}_{\mathbf{x}_k\mathbf{y}_k} &= \sum_{i=0}^{2L} W^{(c)}_{i} \left(\mathcal{X}^{i}_{k|k-1} - \hat{\mathbf{x}}^{-}_{k}\right)\left(\mathcal{Y}^{i}_{k|k-1} - \hat{\mathbf{y}}^{-}_{k}\right)' . && (4.31)
\end{aligned}$$

The same two-step approach adopted in Eqs. 4.27 and 4.28 is applied here to the calculation of the Cholesky factor of the observation error covariance.

5. Update the filter gain and use it, along with the new measurement reading $\mathbf{y}_k$, to calculate the posterior estimate of $\mathbf{x}_k$ mean and covariance Cholesky factor:

$$\begin{aligned}
\mathcal{K}_k &= \left(\mathbf{P}_{\mathbf{x}_k\mathbf{y}_k} / \mathbf{S}'_{\mathbf{y}_k}\right) / \mathbf{S}_{\mathbf{y}_k} \\
\hat{\mathbf{x}}_k &= \hat{\mathbf{x}}_k^- + \mathcal{K}_k \left(\mathbf{y}_k - \hat{\mathbf{y}}_k^-\right) \\
\mathbf{U} &= \mathcal{K}_k \mathbf{S}_{\mathbf{y}_k} \qquad (4.32) \\
\mathbf{S}_k &= \text{cholupdate}\left\{\mathbf{S}_k^-, \mathbf{U}, -1\right\} \mathbf{P}_k^- - \mathcal{K}_k \mathbf{P}_{\mathbf{y}_k\mathbf{y}_k} \mathcal{K}'_k. \qquad (4.33)
\end{aligned}$$

In the first equation, $\mathcal{K}_k$ is obtained as the result of two nested least-squares solutions, starting from the original equation:

$$\mathcal{K}_k \mathbf{S}_{\mathbf{y}_k} \mathbf{S}'_{\mathbf{y}_k} = \mathbf{P}_{\mathbf{x}_k\mathbf{y}_k}.$$

Since $\mathbf{S}_{\mathbf{y}_k}$ is square and triangular, efficient "back-substitutions" avoid the need for matrix inversions, making the time complexity of this operation $\mathcal{O}(LM^2)$.

The posterior measurement update of the state covariance Cholesky factor is calculated by applying M sequential Cholesky downdates to $\mathbf{S}_k^-$, the downdate vectors being the columns of $\mathbf{U}$. This replaces the posterior update of $\mathbf{P}_k$ of Eq. 4.24.

Similar observations to those made for the basic UKF hold in this context for the case of non-additive noises.

4.5 Simulation results

At the end of the previous Chapter, the Double Electrode Averaged Model (DEAM) was identified and simulated against the simulation of a rigorous model of a Li-ion cell. The same approach will be used in this section to test the Single Electrode Averaged Model (SEAM): the same simulated and corrupted data will be considered in a $30\,\% - 70\,\%$ range, and used as reference measured data for the identification procedure. The resulting model will be exploited to implement a Square Root Unscented Kalman Filter for bulk and superficial SOC estimation. This last step requires a further manipulation of the model, since the basic UKF framework involves a discrete-time state equation while the SEAM describes the state dynamics with a continuous-time equation. The latter being linear, one of the many discretization techniques available for linear systems may be applied. In particular, the time-domain conversion will be done through a simple zero-order hold for any of the reported simulations, with the sample time specified each time.

With respect to the DEAM, the single electrode model has half the number of states, M_r being the same. However, the number of parameters is greater, since the values of $\theta_{n0\,\%}$, $\theta_{n100\,\%}$, $\theta_{p0\,\%}$ $\theta_{p100\,\%}$ are now required for relating the dynamics of each electrode solid concentration with one another and with the SOC. This involves the identification of 20 free parameters (4 more than in the DEAM), along with the estimation of the $Mr - 1$ states if they are not known. The same nominal values of Table 3.4 are used, plus the following ones:

$$\begin{aligned} \theta_{p0\,\%} &= 0.6747 & \theta_{p100\,\%} &= 0.379 \\ \theta_{n0\,\%} &= 0.1205 & \theta_{p100\,\%} &= 0.621 \end{aligned}$$

which are calculated according to the Dualfoil configuration (see Appendix A), and the full discharge simulation of Figure 3.3. After 40 iterations of the Levenberg-Marquardt algorithm on the same reference data window used in Section 3.4, the resulting fit indicator[5] settles at about 84.3 % for $M_r \geq 5$. This level of accuracy is very close to the one previously obtained, implying that no significant loss of information has occured.

After validating the model parameters, an SR-UKF state estimator has been implemented in Matlab and tested with Dualfoil simulated data[6] in a variety of operating conditions. In each of these simulations, the initial bulk SOC level has been arbitrarly set to a value of 50 %.

First, the behaviour of the filter has been observed with the cell in an open-circuit steady state, i.e. with zero input current. While temporarily fixing $M_r = 5$, a large number of tuning parameters combinations has been tried in the attempt to minimize the bulk SOC mean squared error (MSE). As a result, the following set of values has been chosen:

$$\begin{aligned} \alpha &= 1 & \beta &= 2 \\ \kappa &= 0 & \mathbf{R^n} &= (0.01)^2 \\ \mathbf{P}_0 &= 1.93 \times 10^4 \cdot \mathbf{I}_{(M_r-1)} & \mathbf{R^v} &= 1 \times 10^3 \cdot \mathbf{I}_{(M_r-1)} \end{aligned}$$

where $\mathbf{I}_{(M_r-1)}$ is the identity matrix of dimension $M_r - 1$. For simplicity, these values will be used also in filters with M_r other than 5, and in operating conditions other than steady state, even if this decision may not lead to optimal perfomance in all the cases considered.

Figure 4.3 shows how three estimators, respectively with $M_r = 3$, 5 and 9, behaves under the above-mentioned assumptions when initialized with a bulk SOC reading of 0 % (i.e. $\bar{c}_{sp_1} = \cdots = \bar{c}_{sp_{(M_r-1)}} = \theta_{p0\,\%} \cdot c_{s,max,p}$). With a sample time of 0.1 s, after 4 s to 8 s depending on M_r, all of them track with negligible error the output and the bulk SOC, whose relationship with the state is expressed in

[5] as defined in Eq. 3.49

[6] as done before, the cell voltage simulated in Dualfoil and corrupted with zero mean and 0.01 V standard deviation will be referred to as "measured" rather than "simulated"

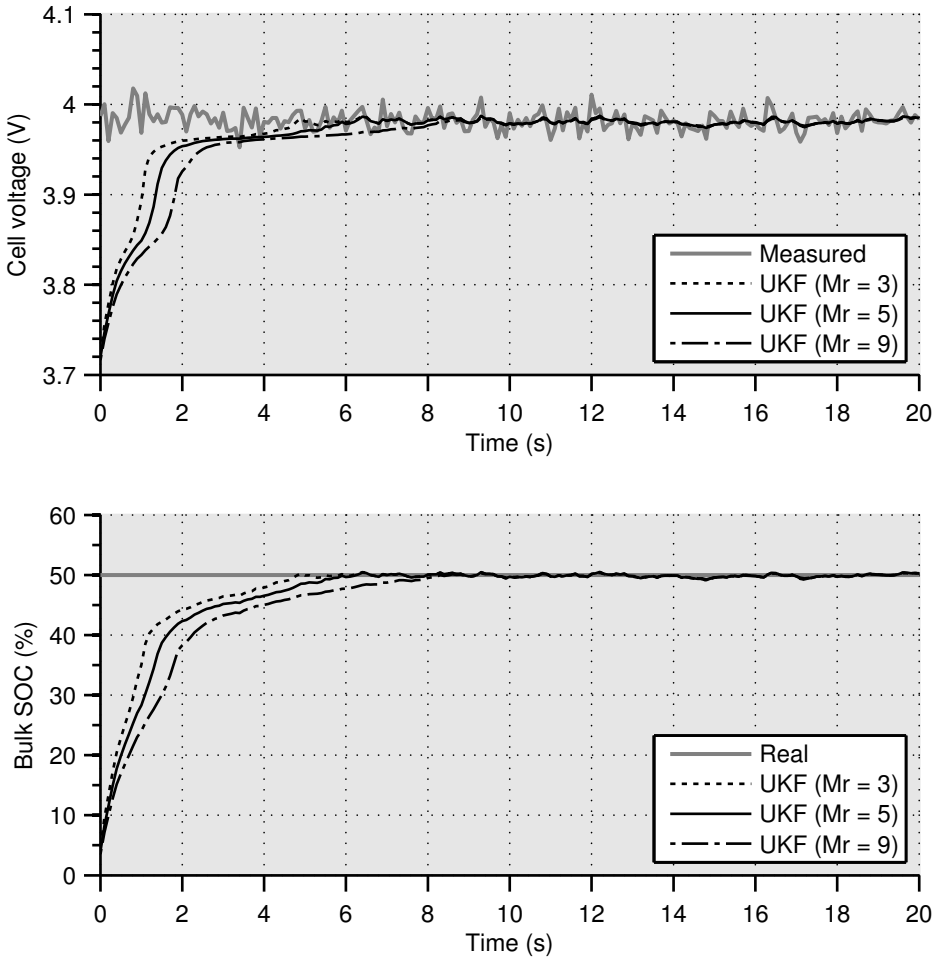

Figure 4.3: UKF performance with no input current and half-charged cell.

Eqs. 4.3, 4.4 and 4.6. In this particular case, lower M_r's lead to faster estimations, since the diffusion has to propagate through a lower number of states to reach the correct concentration levels. However, in dynamical situations a higher M_r will generally correspond to a higher accuracy, as discussed further on.

In order to verify the long-term bulk SOC tracking properties of these filters, two apposite test input profiles have been considered, one with positive (i.e. discharging) and one with negative (i.e. charging) input current density steps of varying intensity. Supposing that the estimators are correctly initialized, and that the sample time is 1 s, the results are reported in Figure 4.4 and 4.5. While the output tracking is mostly accurate with all the filters, the bulk SOC estimation emphasizes some discrepancies between different choices of M_r. The advantage of a higher M_r is clear, especially for higher currents, when the limitations dictated by the diffusion dynamics need a finer discretization for being accurately represented. In particular, for $M_r = 9$ the bulk SOC error remains in the $\pm 1\%$ range, in terms of absolute percentage points, and greater precision can be obtained by further increasing M_r. The disadvantages of a higher M_r lie in the higher computational complexity and in a potentially slower convergence when the filter is initialized far away from the real value, as previously commented in the steady state case.

A last simulation case involves fast and intense current pulses, which may commonly occur in a HEV in situations of sharp accelerations or brakings. The input current profile can be seen in Figure 4.6, along with the output and the superficial SOC both of cell and filters. The superficial SOC is defined similarly to the bulk SOC of Eq. 4.6, where the utilization ratio θ_p is replaced with the superficial utilization ratio $\bar{c}_{ssp}/c_{s,max,p}$, while $\theta_{p0\,\%}$ and $\theta_{p100\,\%}$ are considered the same. In this case, the bulk SOC is not as significant as the superficial SOC, since the time horizon is narrow and, even for high currents, the inner concentration of the cell solid particles cannot swing abruptly. What undergo major changes are the superficial concentrations, that are directly related to the current voltage and ultimately to the available instantaneous power, for a given current. The error is slightly greater than in the cases above, especially for the lower M_r's, while the estimator with $M_r = 9$ yields an absolute error that remains in the range of $\pm 2\%$.

Increasing the amplitude of the input current steps makes the actual non-uniformity along the x-axis of some electrochemical quantities more significant, like the concentration electrolyte (Figure 4.7, and thus some of the model assumptions more inadequate. Moreover, input affects directly the superficial concentration at the same time instant, so that when an input step occurs also $\bar{c}_{ssp}$ changes abruptly. The distributed dynamics of the simulated rigorous cell provides a smoother behaviour, which is more similar to what would happen in a real lithium-ion cell. Nonetheless, the Kalman Filter is able to partially compensate for all of these inaccuracies, within certain operating conditions and for a sufficiently high M_r.

For the last simulation, the sample time has been set to 0.1 s. It has been observed that choosing a sample time of lower order does not only make the filter react faster, but also leads to a more unstable response. 0.1 s has demonstrated to be a reasonable tradeoff in the studied cases.

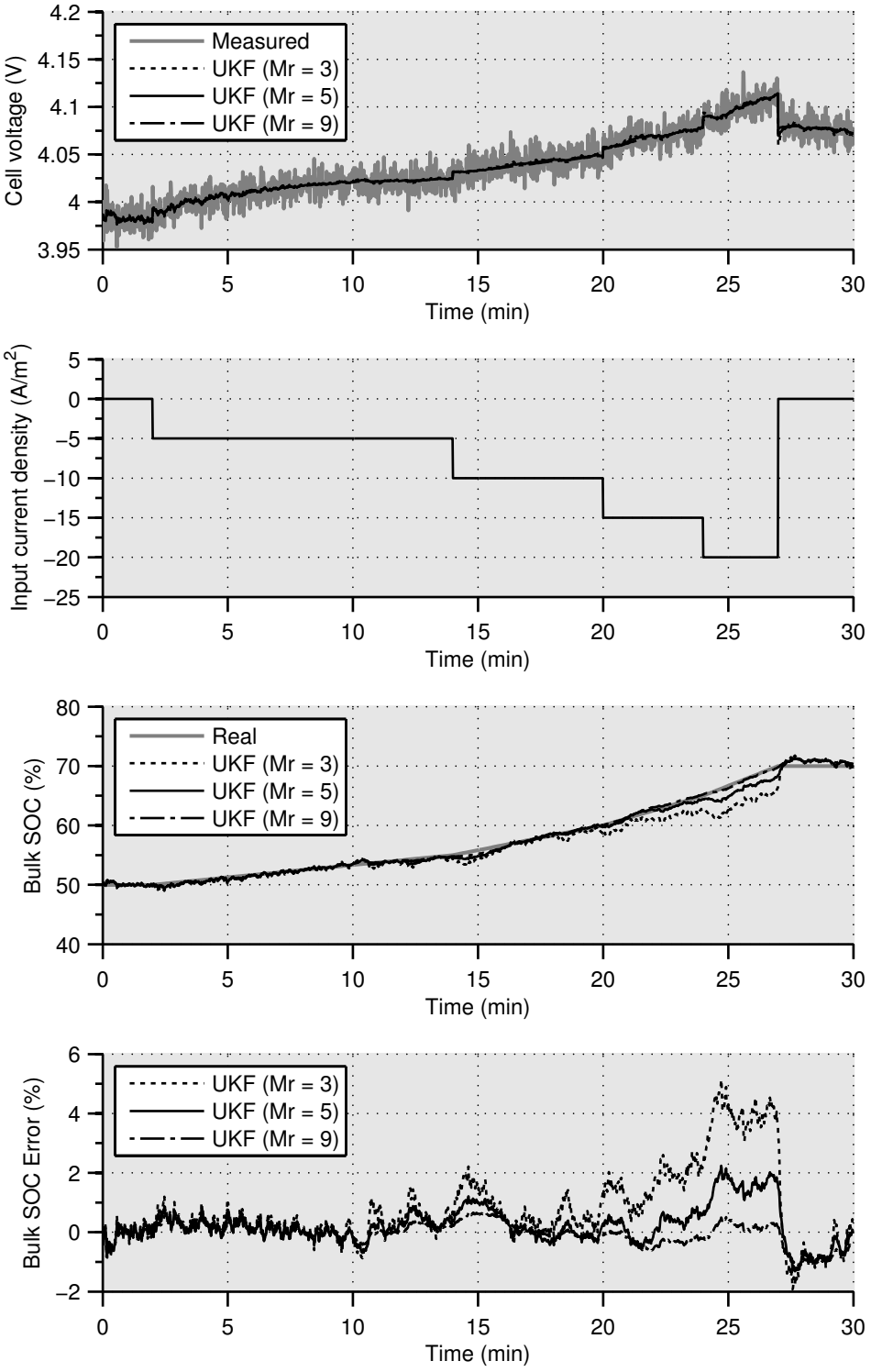

Figure 4.4: UKF bulk SOC tracking performance with several charging input current densities steps.

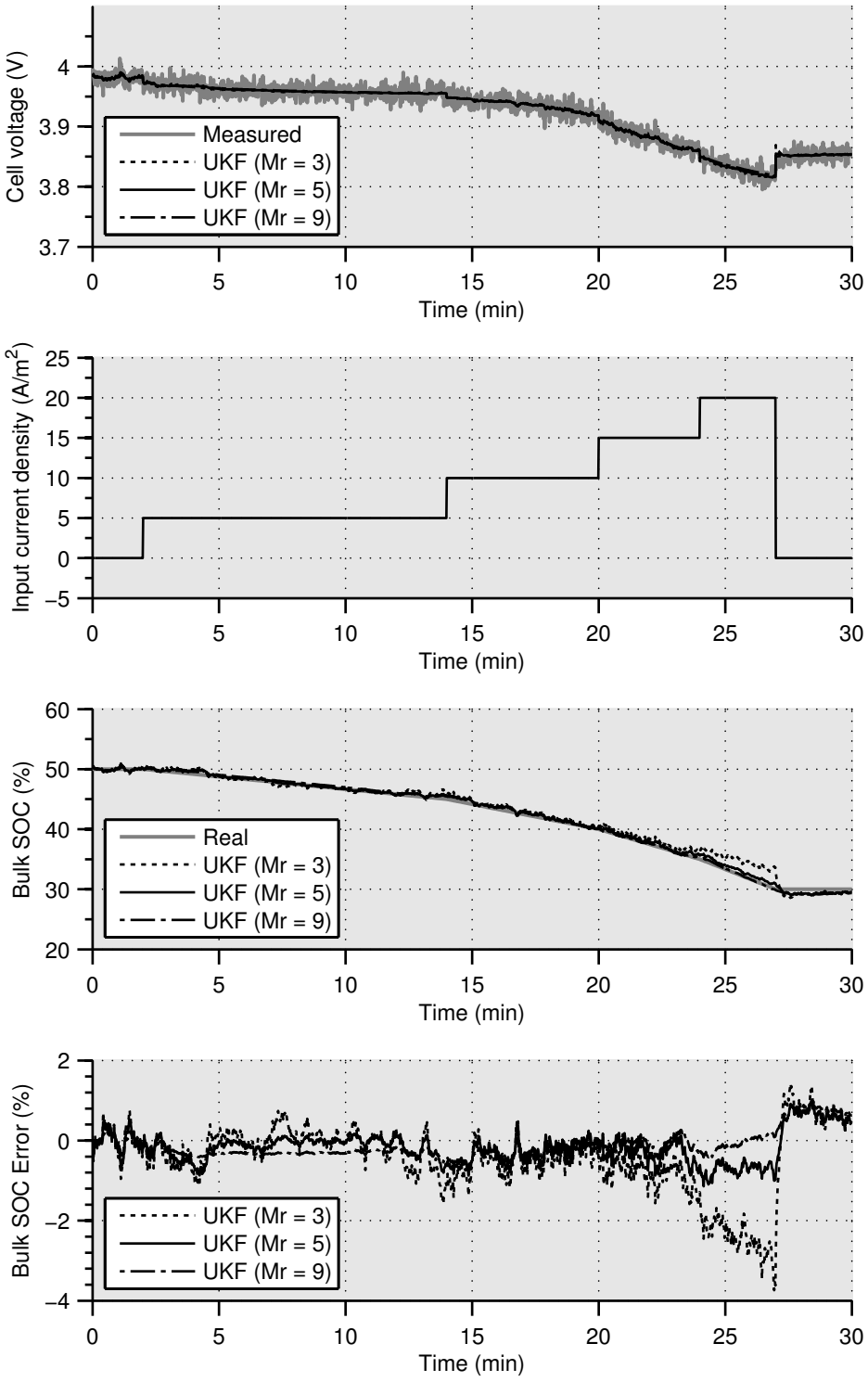

Figure 4.5: UKF bulk SOC tracking performance with several discharging input current densities steps.

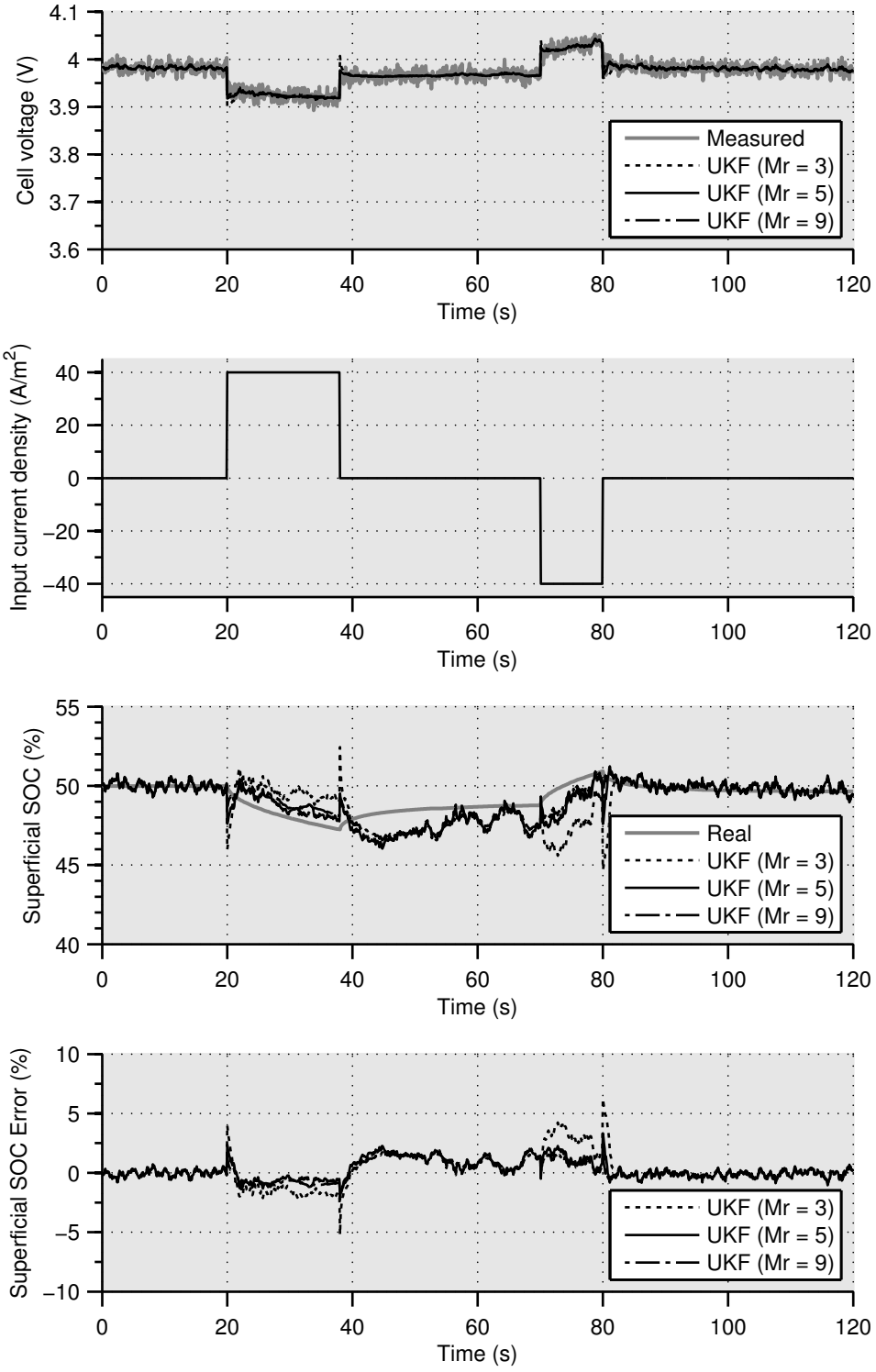

Figure 4.6: UKF superficial SOC tracking performance with charging and discharging input current densities pulses.

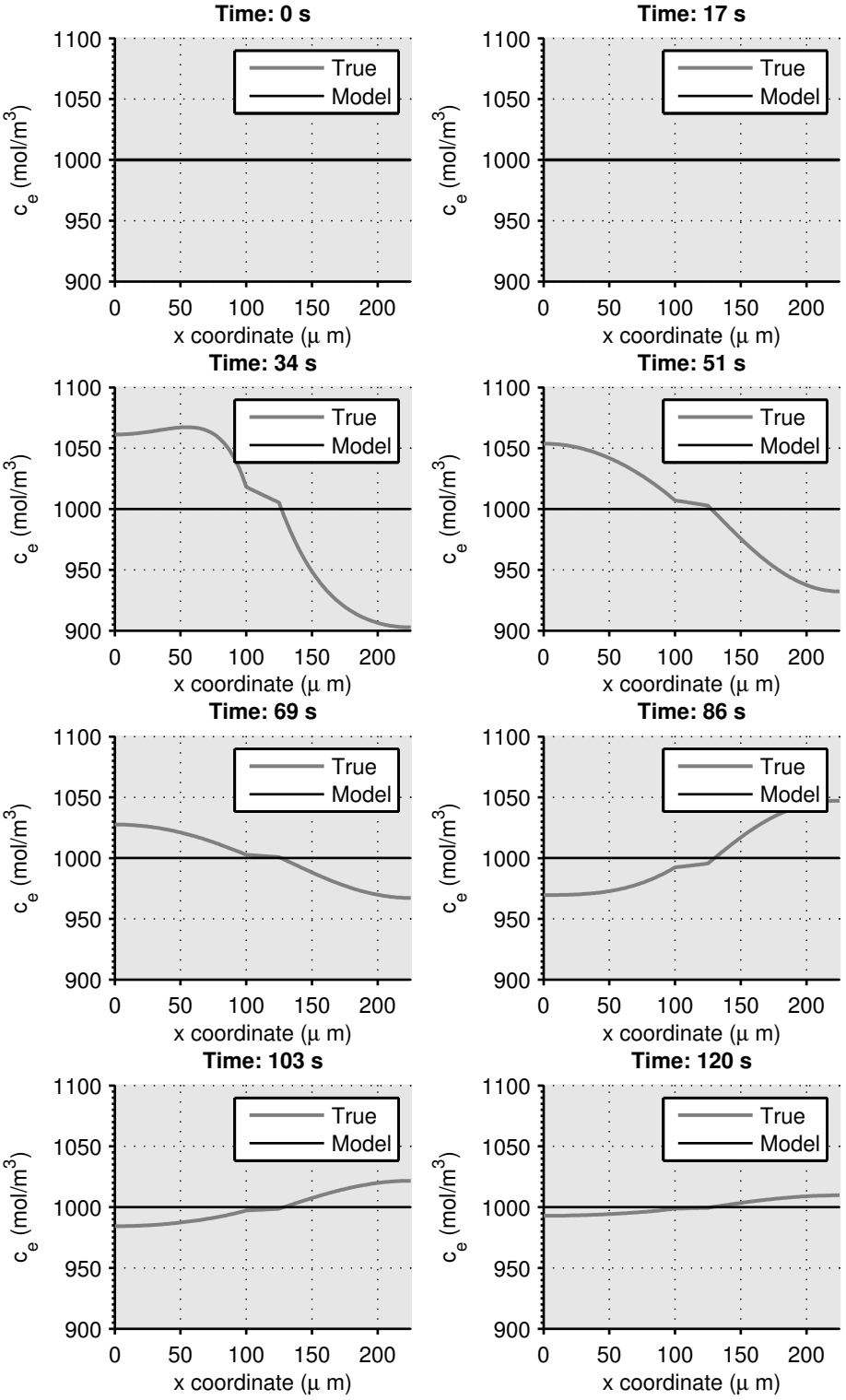

Figure 4.7: Comparison between real electrolyte concentration and SEAM constant concentration in the two pulses simulation case.

Chapter 5

Conclusions

Contents

5.1 The present work

The present work starts in a very general way, i.e. by defining the concept of hybrid electric vehicle, and ends in a very specific way, i.e. by discussing a particular technique for SOC estimation of Li-ion cells. This kind of path has been followed to guide the reader's attention from a general overview of the problem to what is considered its most crucial point.

In the Introduction many words are spent on the key role of the energy storage device management for the full success of the HEV strategy. In terms of currently available mature technologies, this translates into choosing adequate high-power rechargeable batteries, and subsequently designing reliable and efficient Battery Management Systems for them. Among the several chemistries considered, lithium-ion batteries stand out as the best candidates for energy accumulation in the automotive field, and the whole second Chapter is devoted to exploring their virtues and defects.

The most significant drawback of the lithium-ion battery technology is its intolerance to overcharge and underdischarge conditions. When these events occur, the battery may malfunction, damage itself and in the worst case constitute a danger for the surroundings. Given that none of these fatalities should happen, especially when dealing with high power batteries like those required for HEVs, the need for a BMS becomes evident. A second noteworthy reason that motivates the adoption of a BMS is efficiency optimization. In fact, batteries exhibit a different performance for different operating conditions. The ability to dispose of this information in the hybrid propulsion strategy leaves margin for further consumptions reductions.

The management of a battery can consist of several activities and can be done at several levels of complexity. One of the main features of a BMS is monitoring and some of the aspects pertaining to the internal state of the battery. The State of Charge (SOC), for example, accounts for the quantity of energy available in the battery for a given discharge rate. Other indicators may be useful, like the loss of

performance since the batter was new, which is quantified by the so called State of Health (SOH), or the amount of available instantaneous power, which is usually referred to as State of Power (SOP). The availability of part or all of these indicators represent the basis for a reliable and efficient usage of the battery itself.

In general, only current, voltage and temperature measurements are available, while the most useful figures, like SOC, SOH and SOP, are not observable. For this reason, measurements are coupled with appropriate battery models to infer information about the battery internal state. Depending on the requirements of the application, several models and approaches can be adopted for representing and tracking the battery state. While a simple electrical equivalent circuit may be satisfactory for portable electronic devices, a much more accurate description is desirable in the context of HEVs. Here, power exchanges involve highly dynamical scenarios, where the battery is possibly subjected to very high input currents, either drained or supplied. Two representative situations are the need for power after a sharp acceleration, and the need for energy accumulation during a sharp braking. A simple circuit model may not be able to capture all of these dynamics accurately, thus causing inaccuracies in the estimation of the battery state and invalidating the usefulness of the BMS activity.

In order to increase the state estimation accuracy, it is mandatory to work on the model, which is the main subject of the third Chapter. Attention is given to a rigorous electrochemical model that is widely used in the literature. This model develops from the the basic lithium-ion cell working principles, and through a series of assumptions lead to a set of coupled partial differential equations. Even though this model is a reasonably good compromise between model complexity and completeness in the physical description, further manipulation is required in view of a real-time usage for estimation purposes. This leads to the Single Electrode Averaged Model (SEAM), which can be represented in state-space with a linear equation of state and a nonlinear output function.

With regards to the SEAM, the state estimation problem is formulated in stochastical terms in Chapter 4, and tackled in the same Chapter by means of a nonlinear variation of the Kalman Filter, called the Unscented Kalman Filter. This mathematical device provides two main advantages over its most popular alternative, i.e. Extended Kalman Filter. First, it requires no derivative calculations, since it relies only on functional evaluations through the use of deterministically drawn samples from the prior distribution of the state random variable. Second, compared to the EKF, it achieves a generally better level of performance at a comparable level of complexity.

In order to verify the performance of the developed theoretical framework, the rigorous model has been simulated to generate plausible charge and discharge profiles against which the UKF estimator could be tested. Before proceeding to the actual tests, the 20 parameters of the reduced model has been identified offline with an iterative algorithm run on a predefined reference discharge data. The good fit obtained at this stage is an evidence of the ability of the reduced model to capture the most important dynamics of the actual cell. With the identified model, the

UKF has demonstrated a successful ability to filter the measurement noise and the model inaccuracies in each considered simulation case, leading to very satisfactory estimates of SOC and SOP.

The main advantages of the whole approach are summarized in the following list.

- The state of the cell is expressed in terms of electrochemical quantities, from which a variety of indicators can be accurately calculated, like SOC, SOP and SOH.
- Model parameters have a physical meaning, thus the knowledge developed in electrochemical studies of lithium-ion cells can be directly exploited in the parameter estimation procedure.
- Model complexity and accuracy is partially tunable through the parameter M_r.
- The same UKF framework may be extended for the online estimation of some of the model parameters along with the state estimation [36]. This may be useful for tracking the aging of the cell.
- The same UKF framework may be extended to predict the levels of available charge and power in the near future for a more optimized hybrid propulsion strategy.
- Moderate computational complexity.

On the other side, it is important to be aware also of the main disadvantages of this approach, which are outlined below.

- Initial identification of 20 parameters and of the 2 open-circuit potential functions is required.
- Choice of the UKF tuning parameters may not be straightforward.
- General theoretical properties about UKF convergence and performance are not available.
- For very intense input currents, the accuracy may degrade due to the appearence of the influence of neglected phenomena.

5.2 Further work

Passing from the SOC estimation problem to the implementation of a complete BMS involves a series of steps, which can be considered further possible work to be done.

First, the UKF should be extended to address the dual estimation problem, i.e. the simultaneous estimation of states and all or part of the model parameters of a

dynamical system subjected to uncertainty. This extension could be very beneficial in the context of HEV battery management, where the battery aging can cause significant changes in the electrochemical properties of its cells. Also, the ability to obtain more accurate SOH data, based on updated model parameters values, enables the prompt identification of faulty cells in a battery. The most straightforward approach for UKF dual estimation implies the combination of both state variables and unknown parameters in a joint state-space representation. The evolution of parameters is generally supposed to be driven only by noise, since in most cases no dynamical a priori information is available. Alternatively, two separate Kalman filters may be used, one for signal estimation and another for model estimation. The signal filter uses the current estimate of the parameters, while the other uses the signal estimates to minimize a prediction error cost.

A second step towards a complete BMS should address the cell balancing problem. A battery is usually made of several theoretically equal cells, which in practice always have small differences. This may lead to a non-uniform usage of the battery cells, with a consequent non-optimal utilization of the overall potential battery capacity. As for the dual estimation, all the framework developed can used as a basis for dealing with this issue. In fact, an accurate SOC cell reading is the necessary starting point for implementing any cell equalization algorithm. In the literature several already available methods can be found, since the problem has already been studied also for other chemistries.

Further steps include the cell thermal management, the integration and implementation of all the BMS functions into a dedicated hardware, and the interfacing of the BMS with the electronic control unit of the vehicle. All of these are not trivial tasks, but still the internal state estimator set up in the present work offers a good starting point. Also the theoretical aspects may be improved, e.g. by more deeply exploring the role of the UKF tuning parameters, or by considering slightly more advanced reduced electrochemical models that account for secondary phenomena like capacity fading and thermal balances.

All of these expedients possibly define a new generation of BMS, which can guarantee a better level of hybrid electric propulsion performance especially when applied to lithium-ion batteries. Due to the advances in the BMS field, these batteries will be used in an always less conservative way, allowing the diffusion of smaller, cheaper and more efficient energy device systems. This is a necessary step for the HEV technology to bring more tangible benefits in the transportation systems.

Appendix A

Dualfoil configuration file

The code reported below corresponds to the Dualfoil configuration needed for simulating the Li-ion cell with a $LiCoO_2$ cathode, a MCMB 2528 graphite (Bellcore) anode, and a $LiPF_6$ in EC : DMC electrolyte used in Chapter 3 and 4. Even though this may not be the best chemistry for HEV batteries, the availability of plenty of information in the literature about its electrochemical properties makes it a good candidate for simulations.

Some parameters vary from simulation to simulation, like the initial stoichiometric coefficients (here initialized to what is considered a fully charged state) and the input current profile. The output generated by the Dualfoil program has been resampled to a constant time step before being employed, varying from case to case. The `tmmax` parameter has been set equal to the time step used in the subsequent resampling.

```
10        ! lim,   limit on number of iterations
100.0d-06 ! h1,  thickness of negative electrode (m)
25.d-06   ! h2,  thickness of separator (m)
100.0d-06 ! h3,  thickness of positive electrode (m)
25.d-06   ! hcn, thickness of negative current collector (m)
25.d-06   ! hcp, thickness of positive current collector (m)
80        ! n1,    number of nodes in negative electrode
40        ! n2,    number of nodes in separator
80        ! n3,    number of nodes in positive electrode
100       ! n4, number of nodes in solid particle
0     ! mvdc1, flag for variable solid diff coeff in anode
0         ! mvdc3, flag for variable solid diff coeff in cathode
20     ! lims, number of iterations for solid phase convergence
298.d0    ! T      temperature (K)
1000.0    ! xi(1,1), initial salt concentration (mol/m3)
0.621     ! x,     initial stoichiometric parameter for negative electrode
0.379     ! y,     initial stoichiometric parameter for positive electrode
30.0d0    ! tmmax, maximum time step size (s)
3.9d-14   ! dfs1,  diffusion coef. in negative solid (m2/s)
1.0d-13   ! dfs3,  diffusion coef. in positive solid (m2/s)
10.0d-6   ! Rad1,  radius of negative particles (m)
10.0d-6   ! Rad3,  radius of positive particles (m)
0.3       ! ep1,   volume fraction of electrolyte in negative electrode
0.0d0     ! epp1,  volume fraction of polymer in negative electrode
0.1       ! epf1,  volume fraction of inert filler in negative electrode
0.0d0     ! epg1,  volume fraction of gas in negative
1.0       ! ep2,   ep2+epp2=1.0 volume fraction of electrolyte in sep
```

```
0.0d0     ! epp2,  volume fraction of polymer in separator
0.0d0     ! epg2,  volume fraction gas in separator
0.3       ! ep3,   volume fraction of electrolyte in positive electrode
0.0d0     ! epp3,  volume fraction of polymer in positive electrode
0.2       ! epf3,  volume fraction of inert filler in positive electrode
0.0d0     ! epg3,  volume fraction of gas in positive
100.0d0   ! sig1,  conductivity of negative matrix (S/m)
10.0d0    ! sig3,  conductivity of positive matrix (S/m)
1.0d-5    ! rka1,  rate constant for negative reaction
3.d-11    ! rka3,  rate constant for positive reaction,
0.001d0   ! ranode, anode film resistance (ohm-m2)
0.000d0   ! rcathde,  cathode film resistance (ohm-m2)
372.d0    ! cot1,  coulombic capacity of negative material (mAh/g)
274.d0    ! cot3,  coulombic capacity of positive material (mAh/g)
1324.0    ! re,    density of electrolyte (kg/m3)
1800.0    ! rs1,   density of negative insertion material (kg/m3)
5010.0    ! rs3,   density of positive insertion material (kg/m3)
1800.0    ! rf,    density of inert filler (kg/m3)
1780.0    ! rpl,   (not used here) density of polymer material (kg/m3)
0.0d0     ! rc,    density of inert separator material (kg/m3)
8954.0    ! rcn,   density of neg. current collector (kg/m3)[copper]
2707.0    ! rcp,   density of pos. current collector (kg/m3)[aluminum]
0.0d0     ! htc,   heat-transfer coefficient at ends of cell stack (W/m2K)
2000.0d0  ! Cp,    heat capacity of system (J/kg-K)
298.d0    ! Tam,   ambient air temperature (K)
1         ! ncell, number of cells in a cell stack
2         ! lht,   0 uses htc,  1 calcs htc,  2 isothermal
1         ! il1,   1 for long print-out  0 for short print-out
10        ! il2,   prints every il2 th node in long print-out
10        ! il3,   prints every il3 th time step in long print-out
1         ! lflag, 0 for electrolyte in separator only, 1 for uniform
0         ! imp,   0 for no impedance, 1 for impedance
0.0d0     ! capp1, capacitance of negative material (F/m2)
0.0d0     ! capp3, capacitance of positive material (F/m2)
0         ! lpow   0 for no power peaks, 1 for power peaks
0         ! jsol   calculate solid profiles if 1 < jsol < nj
0         ! nside  flag to turn on (1) or off (0) side reactions
0.0d0     ! rksa1   rate constant side reaction 1 negative
0.0d0     ! rksc1   rate constant side reaction 1 positive
0.0d0     ! rksa2   rate constant side reaction 2 negative
0.0d0     ! rksc2   rate constant side reaction 2 positive
0.0d0     ! rksa3   rate constant side reaction 3 negative
0.0d0     ! rksc3   rate constant side reaction 3 positive
3         ! nneg   MCMB 2528 graphite (Bellcore)
11        ! nprop  LiPF6 in EC:DMC (liquid)
6         ! npos    CoO2 (Cobalt dioxide)
1         ! lcurs, number of current changes
10.0d0  120.0d0  1  2.0d0  4.70d0 !Discharge at 10A/m2 for 120min,
                                  !low/high cutoff 2.0/4.7 V
```

Bibliography

[1] A. Arora, N. K. Medora, T. Livernois, and J. Swart. Safety of lithium-ion batteries for hybrid electric vehicles. In G. Pistoia, editor, *Electric and Hybrid Vehicles: Power Sources, Models, Sustainability, Infrastructure and the Market*, pages 463–491. Elsevier, 2010. 18

[2] V. Boovaragavan, S. Harinipriya, and V. R. Subramanian. Towards real-time (milliseconds) parameter estimation of lithium-ion batteries using reformulated physics-based models. *Journal of Power Sources*, 183(1):361–365, August 2008.

[3] R. J. Brodd. Synopsis of the Lithium-Ion Battery market. In M. Yoshio, R. J. Brodd, and A. Kozawa, editors, *Lithium-Ion batteries: Science and Technologies*. Springer, 2009. 12

[4] M. Broussely. Battery requirements for HEVs, PHEVs, and EVs: An overview. In G. Pistoia, editor, *Electric and Hybrid Vehicles: Power Sources, Models, Sustainability, Infrastructure and the Market*, pages 305–347. Elsevier, 2010. 3

[5] A. F. Burke. Batteries and ultracapacitors for electric, hybrid, and fuel cell vehicles. *Proceedings of the IEEE*, 95(4):806–820, April 2007. 2

[6] N. Chaturvedi, R. Klein, J. Christensen, J. Ahmed, and A. Kojic. Algorithms for advanced battery-management systems. *IEEE Control Systems Magazine*, 30(3):49–68, June 2010. 10, 15, 22, 24, 52

[7] M. Debert, G. Colin, M. Mensler, Y. Chamaillard, and L. Guzzella. Li-ion battery models for HEV simulator. In *Les Rencontres Scientifiques de l'IFP: Advances in Hybrid Powertrains*, IFP, Rueil-Malmaison, France, November 2008. 4, 6

[8] D. Di Domenico, G. Fiengo, and A. Stefanopoulou. Lithium-ion battery state of charge estimation with a kalman filter based on a electrochemical model. In *17th IEEE International Conference on Control Applications*, pages 702–707, San Antonio, Texas, USA, September 2008. Part of 2008 IEEE Multi-conference on Systems and Control. 22, 35, 36, 39

[9] M. Doyle, T. F. Fuller, and J. Newman. Modeling of galvanostatic charge and discharge of the lithium/polymer/insertion cell. *Journal of The Electrochemical Society*, 140(6): 1526–1533, 1993. 30

[10] Editors. In search of the perfect battery. *The Economist*, 6$^{\text{th}}$ March 2008.

[11] M. Ehsani, Y. Gao, and A. Emadi. *Modern Electric, Hybrid Electric, and Fuel Cell Vehicles: Fundamentals, Theory, and Design, Second Edition*. CRC Press, 2010. 1, 3, 4

[12] D. D. Friel. Management of batteries for electric traction vehicles. In G. Pistoia, editor, *Electric and Hybrid Vehicles: Power Sources, Models, Sustainability, Infrastructure and the Market*, pages 490–515. Elsevier, 2010. 8

[13] T. F. Fuller, M. Doyle, and J Newman. Simulation and optimization of the dual lithium ion insertion cell. *Journal of The Electrochemical Society*, 141(1):1–10, 1994.

[14] T. Horiba. HEV application. In M. Yoshio, R. J. Brodd, and A. Kozawa, editors, *Lithium-Ion batteries: Science and Technologies*, pages 267–273. Springer, 2009. 11

[15] I. Husain. *Electric and Hybrid Vehicles: Design Fundamentals*. CRC Press, 2003. 3, 4, 6

[16] D. Linden and T. B. Reddy, editors. *Handbook of batteries*. McGraw-Hill, 2002. 4, 51

[17] C. Manzie. Relative fuel economy potential of intelligent, hybrid and intelligent-hybrid passenger vehicles. In G. Pistoia, editor, *Electric and Hybrid Vehicles: Power Sources, Models, Sustainability, Infrastructure and the Market*, pages 69–98. Elsevier, 2010. 2

[18] K. Matsuki and K. Ozawa. General concepts. In K. Ozawa, editor, *Lithium Ion Rechargeable Batteries*, pages 1–9. Wiley-VCH, 2009. 12

[19] R. F. Nelson. Power requirements for batteries in hybrid electric vehicles. *Journal of Power Sources*, 91:2–26, 2000.

[20] J. Newman. Dualfoil 5.1, February 2008. URL `http://www.cchem.berkeley.edu/jsngrp/fortran.html`. 45

[21] J. Newman and W. Tiedemann. Porous-electrode theory with battery applications. *AIChE Journal*, 21(1):25–41, 1975.

[22] I. J. Ong and J. Newman. Double-layer capacitance in a dual lithium ion insertion cell. *Journal of The Electrochemical Society*, 146(12):4360–4365, 1999.

[23] F. Orecchini and A. Santiangeli. Automakers' powertrain options for hybrid and electric vehicles. In G. Pistoia, editor, *Electric and Hybrid Vehicles: Power Sources, Models, Sustainability, Infrastructure and the Market*, pages 573–637. Elsevier, 2010. 7

[24] S. Piller, M. Perrin, and A. Jossen. Methods for state-of-charge determination and their applications. *Journal of Power Sources*, 96:113–120, 2001. 53

[25] S. Santhanagopalan and R. E. White. State of charge estimation for electrical vehicle batteries. In *17th IEEE International Conference on Control Applications*, pages 690–695, San Antonio, Texas, USA, September 2008. Part of 2008 IEEE Multi-conference on Systems and Control.

[26] S. Santhanagopalan and R. E. White. State of charge estimation using an unscented filter for high power lithium ion cells. *International Journal of Energy Research*, 34 (2):152–163, February 2010. 22

[27] S. Santhanagopalan, Q. Guo, P. Ramadass, and R. E. White. Review of models for predicting the cycling performance of lithium ion batteries. *Journal of Power Sources*, 156:620–628, 2006. 35

[28] S. Santhanagopalan, Q. Guo, and R. E. White. Parameter estimation and model discrimination for a lithium-ion cell. *Journal of The Electrochemical Society*, 154(3): A198–A206, 2007. 43

[29] D.U. Sauer, G. Bopp, A. Jossen, J. Garche, M. Rothert, and M. Wollny. State-of-charge — what do we really speak about? In *INTELEC '99, Electronic Proceedings of the Conference*, pages 31–32, Copenhagen, 1999. 51

[30] D. Simon, editor. *Optimal State Estimation: Kalman, H-infinity, and Nonlinear Approaches*. John Wiley & Sons, 2006. 56

[31] K. A. Smith. Electrochemical control of lithium-ion batteries. *IEEE Control Systems Magazine*, 30(2), April 2010. 22, 35

[32] K. A. Smith, C. D. Rahn, and C.-Y. Wang. Model-based electrochemical estimation and constraint management for pulse operation of lithium ion batteries. *IEEE Transactions On Control Systems Technology*, 18(3), May 2010. 55

[33] C. Speltino, D. Di Domenico, G. Fiengo, and A. Stefanopoulou. Comparison of reduced order lithium-ion battery models for control applications. In *Joint 48th IEEE Conference on Decision and Control and 28th Chinese Control Conference*, pages 3276–3281, Shangai, P. R. China, December 2009. 36

[34] K. E. Thomas, J. Newman, and R. M. Darling. Mathematical modeling of lithium batteries. In W. A. van Schalkwijk and B. Scrosati, editors, *Advances in Lithium-Ion Batteries*, pages 345–392. Kluwer Academic/Plenum Publishers, New York, 2002. 22, 44

[35] W. A. van Schalkwijk and B. Scrosati. Advances in lithium-ion batteries: Introduction. In W. A. van Schalkwijk and B. Scrosati, editors, *Advances in Lithium-Ion Batteries*, pages 1–5. Kluwer Academic/Plenum Publishers, New York, 2002. 17

[36] E. A. Wan and R. van der Merwe. The Unscented Kalman Filter. In S Haykin, editor, *Kalman Filtering and Neural Networks*, pages 221–280. John Wiley & Sons, 2001. 56, 59, 61, 75

[37] E. A. Wan and R. van der Merwe. The Square-Root Unscented Kalman Filter for state and parameter-estimation. In *Proceedings of IEEE International Conference on Acoustics, Speech, and Signal Processing*, pages 3461–3464, Salt Lake City, Utah, May 2001. 57

[38] K. Xu. Nonaqueous liquid electrolytes for lithium-based rechargeable batteries. *Chemical Reviews*, 104(10):4303–4417, 2004. 12, 18

[39] M. Yoshio and H. Noguchi. A review of positive electrode materials for Lithium-Ion Batteries. In M. Yoshio, R. J. Brodd, and A. Kozawa, editors, *Lithium-Ion batteries: Science and Technologies*. Springer, 2009. 15

[40] M. Yoshio, R. J. Brodd, and A. Kozawa. Introduction: development of Lithium-Ion Batteries. In M. Yoshio, R. J. Brodd, and A. Kozawa, editors, *Lithium-Ion batteries: Science and Technologies*. Springer, 2009. 12